Thermoelastic Analysis of Contacts Defined by Straight or Curved Boundaries under Dry or Elastohydrodynamic Lubrication Conditions

by

Ali YALPANIAN

MANUSCRIPT-BASED THESIS PRESENTED TO ÉCOLE DE TECHNOLOGIE SUPÉRIEURE IN PARTIAL FULFILLEMENT FOR THE DEGREE OF DOCTOR OF PHILOSOPHY
Ph.D.

MONTREAL, SEPTEMBER 27 2021

ÉCOLE DE TECHNOLOGIE SUPÉRIEURE
UNIVERSITÉ DU QUÉBEC

BOARD OF EXAMINERS (THESIS PH.D.)

THIS THESIS HAS BEEN EVALUATED

BY THE FOLLOWING BOARD OF EXAMINERS

Mr. Raynald Guilbault, Thesis Supervisor
Department of Mechanical Engineering, École de technologie supérieure

Mr. Simon Joncas, President of the Board of Examiners
Department of Systems Engineering, École de technologie supérieure

Mr. Hakim Bouzid, Member of the jury
Department of Mechanical Engineering, École de technologie supérieure

Mr. Jorge Seabra, External Evaluator
Department of Mechanical Engineering, University of Porto

THIS THESIS WAS PRENSENTED AND DEFENDED

IN THE PRESENCE OF A BOARD OF EXAMINERS AND PUBLIC

AT ECOLE DE TECHNOLOGIE SUPERIEURE

ACKNOWLEDGMENT

Firstly, I would like to express my sincere gratitude to my thesis supervisors, Prof. Raynald Guilbault, for his invaluable guidance and scholarly inputs that I received throughout this research work. I am grateful for his excellent advice and support which led me toward completion of this doctoral dissertation. I am particularly grateful for his understanding and support at the time that I faced a grave loss in my life.

I would like to thank my committee members: Prof. Hakim Bouzid, and Prof. Simon Joncas for their time, interest, and constructive comments.

I would like to gratefully acknowledge the funding received in form of scholarships and prizes from: Natural Sciences and Engineering Research Council of Canada (NSERC) and École de technologie supérieure (ÉTS).

My special gratitude goes to my family for their encouragement and love which were essential for completion of my PhD program. Despite the geographical distance, you were always nearby. To my father, I cannot thank you enough for being there for me in every step of my life. To my mother, I wish you were still with me for the completion of this PhD. I miss you and I will cherish the memories I have of you for the rest of my life. I thank you from the bottom of my heart.

ANALYSE THERMOELASTIQUE DE CONTACTS DEFINIS PAR DES FRONTIERES DROITES OU COURBES SOUS CONDITIONS SECHES OU DE LUBRIFICATION ELASTOHYDRODYNAMIQUE

Ali YALPANIAN

RÉSUMÉ

L'amélioration des caractéristiques des paliers et des contacts en général est un besoin constant de l'industrie. Cette étude propose une méthode précise, fiable et efficace qui peut traiter des surfaces de contact qui ont différentes géométries d'aspérités négatives ou positives, tout en tenant compte de la thermoélasticité. Cet objectif est atteint en ajoutant la capabilité thermoélastique et la capacité de traitement des bords courbés à la méthode semi-analytique du demi-espace (SAM) développée par Hartnett (Hartnett, 1980).

Pour préparer un modèle de simulation de contact complet, l'étude identifie les faiblesses de la méthode du demi-espace disponible, qui s'est déjà avérée plus efficace et moins longue que les approches FEA, et cible ces faiblesses. L'une des faiblesses des méthodes basées sur le demi-espace est l'incapacité à simuler de manière fiable les bords courbés. Afin de traiter les bords courbés, l'étude définit, d'abord, la position de la pression d'équilibrage pour chaque position à l'intérieur de la zone de contact afin d'éliminer la contrainte cisaillement qui reste à la surface libre courbé. Deuxièmement, il introduit un facteur de correction pour la pression d'équilibrage afin d'éliminer la contrainte normale qui reste sur la surface libre courbé.

Une autre faiblesse importante de SAM est l'incapacité de prise en compte des effets thermoélastiques, en particulier, en présence des bords libres. Pour remédier à cette faiblesse, l'étude introduit des facteurs d'influence thermoélastiques à calculer une seule fois au début du processus de simulation. Semblable aux erreurs élastiques imposées par les bords libres, en raison de l'hypothèse du demi-espace, les bords libres imposent également certaines erreurs lors considération thermoélastique. Ces erreurs proviennent du débit de chaleur et de la contrainte normale thermoélastique généré à la surface libre. Cette étude traite, d'abord, les bords libres plats en tirant parti du débit de chaleur généré à la surface libre afin de définir la frontière thermique correspondante en appliquant des patchs de chaleur d'équilibrage et en introduisant un facteur de modification des frontières thermiques. À la deuxième étape, le processus calcule un facteur de correction pour le patch de chaleur d'équilibrage appliqué pour tenir compte de la contrainte normale thermoélastique générée à la surface libre plat.

A l'étape suivante, l'étude considère les bords libres courbés tout en prenant en compte les effets thermoélastiques. Depuis que les premières étapes de l'étude ont déjà traité les aspects élastiques des bords libres courbés, cette étape se concentre uniquement sur les aspects thermoélastiques. Pour ce faire, l'étude calcule, d'abord, la position des patchs de chaleur d'équilibrage, puis applique le facteur de modification de la frontière thermique introduit dans les étapes précédentes pour définir la frontière thermique au bord libre courbé. Ensuite, l'étude calcule un facteur de correction pour le patch de chaleur d'équilibrage afin d'éliminer la contrainte normale thermoélastique générée à la surface libre courbé pour une frontière thermique spécifique (frontière thermique adiabatique). Dans l'étape finale, l'étude introduit une dernière modification du facteur de correction introduit à l'étape précédente pour tenir compte d'autres frontières thermiques.

Étant donné que le modèle proposé est suffisamment flexible pour gérer tout contact avec un profil de pression arbitraire et variable, l'étude a utilisé le modèle développé pour modéliser un contact de roulement thermoélastique thermique élastohydrodynamique avec des bords libres. Ensuite, l'étude a effectué une analyse factorielle complète sur les effets des trois principales variables de contact (Charge, vitesse moyenne et grade de viscosité du lubrifiant utilisé) sur les paramètres caractéristiques du contact lubrifié (Pression maximale, température maximale et épaisseur minimale du film de lubrifiant).

Mots-clés : mécanique de contact, déplacement thermoélastique, méthode demi-analytique, Lubrification élasthydrodynamique

THERMOELASTIC ANALYSIS OF CONTACTS DEFINED BY STRAIGHT OR CURVED BOUNDARIES UNDER DRY OR ELASTOHYDRODYNAMIC LUBRICATION CONDITIONS

Ali YALPANIAN

ABSTRACT

Improvement of the characteristics of bearings and contacts in general is a constant need of the industry. This study proposes a precise, reliable and time efficient method that, while taking into account thermoelasticity, it can also handle contact surfaces with different negative or positive asperity geometries. This goal is achieved by adding thermoelastic consideration and curved edge treatment capability to the well-known half-space semi-analytical method (SAM) developed by Hartnett (Hartnett, 1980).

To prepare a comprehensive contact simulation model, the study identifies the weaknesses of the available half-space method, which has already been proven more effective and less time consuming than FEA approaches, and targets those weaknesses. One of the weaknesses of the half-space based methods is the inability to reliably simulate the curved edges. In order to handle curved edges, first, the study defines the position of the counterbalance pressure for each position inside the contact area to eliminate the remaining shear stress at the curved free-surface. Second, it introduces a correction factor for the counterbalance pressure to eliminate the remaining normal stress on the curved free-surface.

Another important weakness of SAM is the consideration of thermoelastic effects, specifically in the presence of free-edges. To rectify this weakness, the study introduces thermoelastic influence factors to be calculated only once at the beginning of the simulation process. Similar to elastic errors imposed by free-edges, because of the half-space assumption, free-edges impose some errors for thermoelastic considerations as well. These errors come from the generated heat flux and thermoelastic normal stress at the free-surface. This study first treats straight free-edges by taking advantage of the generated heat flux at the free-surface in order to define the corresponding thermal boundary condition by applying counterbalance heat patches and introducing a thermal boundary modification factor. At the second step, the process calculates a correction factor for the applied counterbalance heat patch to account for the generated thermoelastic normal stress at the straight free-surface.

At the next step, the study considers the curved free-edges while taking into account the thermoelastic effects. Since the initial steps of the study have already treated the elastic aspects of the curved free-edges, this step focuses only on the thermoelastic aspects. To do so, first, the study calculates the position of the counterbalance heat patches and then applies the thermal boundary modification factor introduced in the previous steps to define the thermal boundary condition at the curved free-edge. Then, the study calculates a correction factor for the counterbalance heat patch to eliminate the thermoelastic normal stress generated at the curved free-surface for a specific thermal boundary condition (adiabatic boundary condition). In the final step, the study introduces a final modification for the correction factor introduced in the previous step to account for other thermal boundary conditions.

Since the proposed model is flexible enough to handle any contact with arbitrary and variable pressure profile, the study used the developed model for modeling a thermoelastic thermal elastohydrodynamic rolling contact with free-edges. Then, the study performed a comprehensive factorial analysis on the effects of the three main contact variables (Load, average velocity and viscosity grade of the employed lubricant) on the characteristic parameters of the lubricated contact (Maximum pressure, maximum temperature and minimum film thickness).

Keywords: contact mechanic, thermoelastic deformations, semi-analytical method, elastohydrodynamic lubrication

TABLE OF CONTENTS

Page

LIST OF TABLES

LIST OF FIGURES

LIST OF ABBREVIATIONS AND ACRONYMS

EHL	Elastohydrodynamic lubrication
FEA	Finite element analysis
FSI	Fluid solid interaction
POM	Polyoxymethylene
RFW	Rotational friction welding
RMS	Root mean square
SAM	Semi-analytical method
TEHL	Thermal Elastohydrodynamic lubrication
TTEHL	Thermoelastic Thermal Elastohydrodynamic lubrication

LIST OF SYMBOLES

Variable	**Description**
A	The area under study including the contact area (m^2)
ΔA	The area of a small element over the area A (m^2)
a, b	Hertzian lengths of a contact patch (m)
a *(2nd Article)*	Edge length of the validation model surface (m)
Bi	Biot number
B_z	The equivalent force obtained from accumulation of the shear stresses along z direction in a half-space
c	The distance between the point force and the point where the stress is being calculated (m)
C_{bc}	Thermal boundary modification factor
C_r	The equivalent radial force obtained from accumulation of the normal stresses along z direction in a half-space
C_z	The equivalent axial force obtained from accumulation of the normal stresses along r direction in a cylinder
d	The distance between the point force and the projection of the point where the stress is being calculated on the contact plane (m)
D	Diameter of the thermoelastic mirror zone (m)
E	Modulus of elasticity (Pa)
ES	Entraining speed (m/s)
EHL	Elastohydrodynamic lubrication
f	Influence factor
f_{TE}	Thermoelastic influence factor
F	Force/Load (N)
$\hat{F}$	The distribution of the load force along the ring line (N/m)
FEA	Finite element analysis

FSI	Fluid solid interaction
g	The initial separation of the contact bodies from the contact plane (m)
G	Shear modulus (Pa)
h	Coefficient of heat convection (W/m^2 °K)
H	Physical equivalent of infinity (m)
h_l	Lubricant film thickness (m)
h_0	Minimum lubricant film thickness (m)
I (1st & 3rd Article)	Modified Bessel function of the first kind
I (2nd Article)	Electrical current (Amp)
ISO VG	ISO viscosity grade
J	Bessel function of the first kind
K	Elliptical integral of the first kind
k (1st Article)	General parameter for an ordinary differential equation used in calculation of potential function
k (2nd & 3rd Article)	Thermal conductivity (W/m °K)
l	Distance from edge of the quarter space (m)
L	Length (m)
L_E	Effective length (m)
LH	Left hand side of the equality equation
l_r	Position of the line of action of C_r
m	The corner points of a pressure patch inside the circular boundary
m'	The corner points of the mapped correction patch outside the circular boundary
MF	Dimensionless minimum film thickness
MP	Dimensionless maximum contact pressure
MT	Maximum contact temperature

n	Dimensionless radius ratio
nsf	Normal stress elimination correction factor for $v=0.3$
nsf_v	General normal stress elimination correction factor
nsf_{TE}	Thermoelastic normal stress elimination correction factor
P	Pressure (Pa)
$\bar{P}$	Dimensionless pressure
p	Auxiliary variable
P_H	Maximum Hertzian pressure (Pa)
PM	Proposed method
Q *(1st Article)*	Distributed load (N/m)
q *(1st Article)*	Auxiliary variable
q / Q *(2nd & 3rd Article)*	Heat generation/partition (W)
Q^* *(1st Article)*	Modified distributed load (N/m)
Q^* *(2nd Article)*	Equivalent counterbalance heat (W)
$\hat{Q}$	Distributed heat flux (W/m)
$\hat{Q}^*$	Modified distributed heat load (W/m)
q''	Heat flux (W/m^2)
$\overline{q''}$	Dimensionless heat flux
q'''	Volumetric heat generation (W/m^3)
R *(1st & 3rd Article)*	Radius of the free edge (The circular boundary) (m)
R *(2nd Article)*	Equivalent contact radius in rolling direction (m)
R_c	Electrical contact resistance (ohm)
RFW	Rotational friction welding
RH	Right hand side of the equality equation
RMS	Root mean square

RS	Right hand side of the equality equation
r	Radial position (m)
r'	The distance between the line of action of C_z and the free edge (The circular boundary)
r_z	Radial position of the line of action of C_z
$\bar{r}$	Dimensionless radius (r/R)
s (1st Article)	Auxiliary variable
s (2nd & 3rd Article)	Distance (m)
s_0	Heat-affected zone radius (m)
SAM	Semi-analytical method
SS	Sliding speed (m/s)
t	Auxiliary variable
T	Temperature (˚K)
ΔT	Temperature difference (˚K)
TEHL	Thermal Elastohydrodynamic lubrication
TTEHL	Thermoelastic Thermal Elastohydrodynamic lubrication
TTEHL-TB	Thermoelastic Thermal Elastohydrodynamic lubrication with thermal boundary
$\bar{U}$	Dimensionless velocity
u	General parameter for an ordinary differential equation integration
u_f	Lubricant velocity in rolling direction (m/s)
v_f	Lubricant velocity in lateral direction (m/s)
w	Normal displacement (m)
w_Q *(1st Article)*	The normal displacement at r_i caused by a ring load Q of radius r_o over the half-space
w_Q *(2nd Article)*	The normal displacement at a distance $l_{z_{TE}}$ from the free edge caused by the mirroring heat load (m)

w_{Q^*} *(1st Article)*	The combined normal displacement at r_i caused by a ring load of radius r_o over the half-space and the normal stress elimination process
w_{Q^*} *(2nd Article)*	The normal displacement at a distance $l_{z_{TE}}$ from the free edge caused by the mirroring heat load and the normal stress elimination process (m)
w_E, w_{TE}	The normal displacement at a distance $l_{z_{TE}}$ from the free edge caused by the loads obtained from accumulation of the normal stresses (m)
x, ξ	Cartesian coordinate position (Horizontal) (m)
y, ζ	Cartesian coordinate position (Vertical) (m)
Δx, Δy	Element dimension (m)
z	The position in z direction (m)
$\bar{x}, \bar{y}, \bar{z}$	Dimensionless Cartesian coordinate positions
α	The approach between the two bodies in contact (m)
β *(1st & 3rd Article)*	The angle between $\theta=0$ line and the line between the force point on a ring load and the point at ($\theta=0$, $r=R$)
β *(2nd Article)*	Coefficient of thermal expansion (lubricant) (K^{-1})
γ	Coefficient of thermal expansion (solid) (K^{-1})
η	Dynamic viscosity of the lubricant (Pa.s)
θ	Angular position
κ	Thermal diffusivity (m^2/s)
μ	Friction coefficient
ν	Poisson ratio
ρ	Auxiliary variable
σ, σ_f	Normal stress (Pa)
$\bar{\sigma}$	Dimensionless normal stress
τ	Shear stress (Pa)
$\bar{\tau}$	Dimensionless shear stress

φ	Angular limit
Φ	Heat flux resultant (W/m)
ϕ	Stress potential function in cylindrical coordinate system

Index	**Identifier of the parameters related to**
a	Body number one
b	Body number two
c	Center
cy	Cylinder
E	Elastic (Piezoelastic)
H	Physical equivalent of infinity
ha	Half-space
I	Index of the point that its displacement is being calculated
i	The inner ring load
J	Index of the pressure patch
j	The point where displacement is being calculated
k	The pressure patch
L, U	Four sides of a rectangular element
o	The outer ring load
r	Radial direction
TE	Thermoelastic
u	Sigma parameter
x, y, z	Cartesian coordinate directions

INTRODUCTION

Mechanical contacts are key elements of many power transfer systems used in different equipment, including the power train gearboxes of wind turbines, helicopters and aircrafts (Bhaumik, Sujata, Kumar, Venkataswamy, & Parameswara, 2007 ; Budinski, 2014 ; Siddiqui, Deen, Khan, & Ahmad, 2013 ; Tazi, Châtelet, & Bouzidi, 2017). In many cases, their failure has proven to be catastrophic. For example, one of the main reasons for the crash of Sikorsky S-92A, C-GZCH on March 12, 2009 (St. John's, Newfoundland and Labrador, 35 NM E) was failure of the tail gearbox (A09A0016, 2010). Therefore, the proper design of the power transfer elements is of utmost importance.

The presents study aims to prepare a precise, reliable and time efficient multipurpose contact simulation tool that takes into account the thermoelastic effects. This simulation tool is able to is able to handle the textured surfaces that are recently getting noticed because of the advancements in smart surface engineering (Erdemir, 2005 ; Gropper, Wang, & Harvey, 2016 ; Manser, Belaidi, Hamrani, Khelladi, & Bakir, 2019 ; Ohue & Tanaka, 2013). The contributions of this research are presented in three published (or submitted) articles integrated into an article-based thesis.

This introduction first presents the problematic of the research, the main research objective and its sub-objectives, the corresponding methodologies and finally the document structure.

0.1 Research problem

To control the life span of a set with mechanical contacts, without compromising its characteristics, it is important to know the precise behavior of the contact under real conditions including thermal behavior of the lubricant and thermoelastic response of the solids.

By knowing the affecting factors controlling this behavior, it would be possible to adapt the surface design, treatment and/or operating conditions to the tribological needs and avoid phenomena like early pitting, wear and jamming in bearings and gears. Aside from the thermal aspects of the contact problems, there are some geometrical aspects that also need to be taken into account. Therefore, the general problem of this research is lack of a comprehensive model that, while being time efficient, is also reliable, precise and multipurpose.

Finite element analysis (FEA) and Semi-analytical method (SAM) are two of the most common methods employed for contact analysis. In most cases, FEA gives reasonably acceptable precision for different mechanical problems but sometimes the cost is too high. Typically, a 3D FEA requires a considerable memory size and consumes a lot of time for preparation and analysis (Effertz, Fuchs, & Enzinger, 2017 ; Tian & Bhushan, 1996). Also, for complicated multi-physics problems like, thermal EHL contacts, the complexity of the analysis is rather high, and the results are not necessarily as reliable as they usually are for the simple problems. For such contact problems, semi-analytical methods (SAM) give reliable results with far less costs in comparison with FEA (Hartnett, 1980 ; J. Li & Berger, 2003).

Therefore, this study aims to develop an improved SAM that has the earlier mentioned properties. These half-space base methods have some limitations that confine their applicability. During the past few decades some of these limitations have been overcome by modifications proposed by researchers (Guilbault, 2011 ; Hanson & Keer, 1995 ; Hetényi, 1960, 1970 ; Keer, Lee, & Mura, 1983). Hartnett's SAM (Hartnett, 1980) is a well-known method that has been used in many of these studies.

The main assumption in Hartnett's SAM (Hartnett, 1980) is half-space assumption for contacting bodies. Aside from the main benefit of this assumption, which is simplification of the contact analysis, it also imposes some imprecision. For example, the pressure profile obtained from Hartnett's method for contacts with free-edges is rather erroneous. Since Hartnett's method is a rather fast and practical method, many researchers have tried to overcome these mentioned shortcomings (Guilbault, 2011 ; Hanson & Keer, 1995 ; Keer et al., 1983). Nevertheless, there are some limitations that have not been addressed yet; like thermoelasticity effects or curved free-edges that can be found in surfaces with different asperities and cavities or some textured surfaces (SKF, 2012).

A lot of EHL contact analysis models use the principles of Hartnett's SAM method. Most of these models do not take into account the effect of the heat generated in the lubricant on the contacting solids (Guilbault, 2013 ; Mihailidis, Agouridas, & Panagiotidis, 2013 ; X. Wang, Liu, & Zhu, 2017). Therefore, there are not many studies that consider thermoelasticity effects and the ones that do still need a lot of work (W. Z. Wang, Hu, Wang, & Liu, 2006).

Hence, the main problem that this thesis intends to address is the absence of a comprehensive model that can handle different practical contacts than contain curved and/or straight free-edges.

So, the main objective of this thesis is:

To develop a comprehensive numerical contact method that handles both straight and curved free-edges while taking into account the effects of thermoelasticity.

This main problem can be divided into three separate but related problems and in turn lead to sub-objectives of this thesis. The first problem is current SAMs' inability to handle contacts with curved edges in a fast and reliable manner. The second and third problems are lack of a fast and reliable approach for SAM to take into account thermoelasticity for contacts with straight and/or curved free-edges.

0.2 Objectives

Dividing the main objective results in tangible sub-objectives that can be reached in consecutive steps. This section briefly describes these sub-objectives. The next section will explain the methodologies employed in order to obtain these sub-objectives.

0.2.1 First sub-objective

The first sub-objective is:

To introduce an adjustment to SAM that gives it the capability of handling non-thermoelastic contacts with curved free-edges.

This adjustment should not compromise the precision of the SAM while keeping its main characteristics: time efficiency and reliability.

0.2.2 Second sub-objective

The second sub-objective is:

To infuse the capability to consider thermoelastic effects into SAM in a relatively simple approach and at the same time giving it the capability of handling straight free-edges.

The precision, reliability and rapidity of the resulting SAM is important.

0.2.3 Third sub-objective

The third sub-objective is:

To introduce another adjustment to the developed thermoelastic SAM in order to make it capable of handling curved free-edges as well.

As before, while being precise and reliable, the final model should not be excessively time consuming.

0.3 Methodologies

This section lays down a rough scheme of the methodologies employed for reaching each of the sub-objectives described in the previous section. These methodologies are explained in more detail in the articles presented in the following sections.

0.3.1 Methodology for obtaining the first sub-objective

In order to obtain the first objective, first, the process calculates the shear stress generated on the curved free-surface by applying a load on the contact surface because of the half-space assumption. In the next step, the process finds the position of the corresponding counterbalancing load that creates an accumulated stress of the same magnitude on the curved free-surface to eliminate the generated shear on the curved free-surface. Then, the procedure modifies the magnitude of the counterbalance load in order to eliminate the effects of the remaining normal stress on the curved free-surface. To do so, the procedure calculates the generated normal stress on the curved free-surface by the applied load. Afterwards, a cyclic normal stress elimination process defines overcorrection the overcorrection for the counterbalance load. The first article explains this cyclic procedure in more detail.

In the end, this methodology leads to two simple steps for the treatment of curved free-edges using SAM. The first step gives the position of a counterbalancing load and the second modifies its magnitude.

0.3.2 Methodology for obtaining the second sub-objective

In the first step in pursuit of the second objective, the thermoelastic displacement equation proposed by Barber (Barber, 1971) helps the creation of a thermoelastic influence factor that can easily be integrated into Hartnett's SAM (Hartnett, 1980). Similar to the influence factor introduced by Hartnett, the thermoelastic influence factor introduced here depends only on the grid geometry. Hence, it can be calculated only once at the beginning of the calculation process.

Half-space assumption results in generation of heat flux at the free-surface. An antagonistic heat flux at the free-surface can eliminate this generated heat flux. This antagonistic heat flux can be created by applying a symmetric counterbalance heat load on the surface of the half-space. Nonetheless, instead of the complete elimination of the generated heat flux, the process modifies the counterbalance heat load to define desired thermal boundary conditions at the free-surface by taking advantage of the convection-conduction relation described by Biot number.

The next step for obtaining the second objective is to eliminate the remaining thermoelastic normal stress on the free-surface because of the half-space assumption. To do so, the process calculates the normal stress engendered on the free-surface and replaces it with an equivalent force. Then, it eliminates this equivalent force in a cyclic procedure that is explained in more detail in the second article. This procedure results in an overcorrection factor for the counterbalance heat load.

In the end, following this methodology results in thermoelastic influence factor, a counterbalance load to define the thermal boundary at the free-surface and finally a correction factor for eliminating the remaining thermoelastic stress at the free-surface.

0.3.3 Methodology for obtaining the third sub-objective

To obtain the third objective, first, the procedure calculates the heat flux generated at the curved free-surface because of the half-space assumption. Then, it proposes another position outside the contact zone for applying a counterbalance heat load in order to eliminate the generated heat flux. When the counterbalance position is defined, the procedure applies the earlier described thermal boundary definition factor to account for the thermal boundary condition at the curved free-surface.

To eliminate the thermoelastic normal stresses that are also generated on the curved free-surface because of the half-space assumption, a cyclic approach similar to the one performed for the second objective, but instead for the curved free-surface, gives the modification factor for elimination of the remaining thermoelastic normal stresses assuming adiabatic thermal boundary condition. This factor modifies the counterbalance heat load as well.

Since the thermoelastic normal stress elimination factor is calculated for an adiabatic boundary condition, the next step calculates an extra overcorrection factor to account for the effect of thermal boundary condition on the thermoelastic normal stress elimination factor. The process of calculating the extra overcorrection factor is done analytically.

Ultimately, the explained methodology introduces three factors to be applied into the model that was prepared after accomplishing the second sub-objective. The first factor gives the position of the counterbalance heat load for defining the thermal boundary condition. The second one, adjusts the counterbalance heat load in order to eliminate the thermoelastic normal stress for adiabatic boundary condition. And the third, overcorrects the adjusted counterbalance heat load once more to tune the thermoelastic normal stress elimination factor for different thermal boundary conditions.

0.4 Structure of the thesis

This thesis is comprised of six main chapters excluding the references. The first chapter is the introduction to the main subject of the thesis followed by the problematic of the research, the objectives and a short description of the methodology laid out for reaching those objectives. At the end of chapter one, the general structure of the thesis is presented (This section). The second chapter is a brief literature review of the works done in the main subjects of this thesis. The next three chapters (Articles 1, 2 and 3) are respectively the detailed presentation of each sub-objective presented above, their methodologies and the obtained results. The last chapter of this thesis bring forth the overall conclusion that includes the main achievements of this work, the restraining limitations and finally some recommendations for future research subjects.

CHAPTER 1

LITERATURE REVIEW

This section presents a comprehensive review of the previous studies performed on subjects related to the intended contact analysis of this thesis. The following subsections present the main subjects related to creating a comprehensive contact model that handles lubrication, thermal effects on lubricants, thermoelastic responses of the contacting bodies and various types of free-edges.

Since loading is present in any contact analysis, the first subsection presents the common relation used in different SAMs for calculating the generated load in the contact. The next subsection covers the elastic response of the contacting bodies to the applied pressure. Afterwards, possible types of heat generation in contacts are discussed. The subsection that comes after describes the thermoelastic response of the contacting bodies to the applied heat. The next subsection pronounces the importance of free-edges and the issues raised by them in half-space based simulations. After the main phenomena related to the contacting bodies are discussed, the next subsection describes the lubricant properties and their dependence on pressure and temperature. Following that, the next subsection presents the required hydrodynamic and energy equations for a lubricated contact. Finally, an overview lays out the experimental and numerical approaches employed in different studies for such contact analysis.

1.1 Load

Existence of the load ensures existence of the contact. As many references have explained (Hartnett, 1980 ; Najjari & Guilbault, 2014 ; Yalpanian & Guilbault, 2020), the load balance equation, which ensures the load equilibrium over the solution domain, is simply expressed as:

$$Load = \iint_{\mathrm{A}} P(x, y)\, dxdy \tag{1.1}$$

where *P* is the applied pressure and (*x, y*) are the planar coordinates. Assuming that the contact area is rather small in comparison with the curvature of the contacting bodies, Eq. (1.1) considers a flat projection of the contact area *A* for the integration. This equation is valid for every type of contact that complies with the contact size assumption.

1.2 Piezo-elasticity

Piezoelasticity is the base of dry contact pressure calculation. Hertz theory is the most common basic contact pressure calculation approach (Johnson, 1987). Based on the theory of elasticity, Hertz proposed a reliable but limited contact theory. Since then, many researchers have worked on developing more practical and general methods (Bachtar, Chen, & Hisada, 2006 ; Guilbault, Gosselin, & Cloutier, 2005 ; Hartnett, 1980). One of the pioneering works on this subject is the work performed by Hartnett (Hartnett, 1980). He proposed a numerical method to calculate the pressure distribution of a contact with any physical shape. To do so he used the results of Boussinseq solution for a half-space.

1.2.1 Hertz's Theory

To describe Hertz's theory, we can see the pressure at the contact point as a singular point compared to the whole body. If, about the singular point, we describe a closed surface of small dimensions compared to the whole body, but very large in comparison with the element in which the forces act, the deformations outside and inside this surface may be treated independently of each other. Outside, the deformations depend on the shape of the whole body, the finite integrals of the force-components at the singular point, and the distribution of the remaining forces; inside, they depend only on the distribution of the forces acting inside the element (Hertz, 1896).

Hertz assumed the surfaces in contact are imagined as perfectly smooth and no tangent force exist in the contact. The following assumptions are made by Heinrich Hertz for his theory (Adams & Nosonovsky, 2000 ; Herák, Chotěborský, Sedláček, & Janča, 2018).

- The dimensions of the contact area must be small compared to the dimensions of each body and to the radii of curvature of the surfaces.
- Isotropy and homogeneity of the contact zone.
- The strains are sufficiently small for linear elasticity to be valid.
- The contact is frictionless, so that only the normal stress is transmitted.
- Projected areas for point contacts are elliptical.
- Each body is approximated by an elastic half-space.

Hertz's approach takes the point of first contact as the origin of a Cartesian coordinate system with the *x–y* plane as the common tangent plane while the *z*–axis is directed inwards. During the compression by the normal load *P*, distant points T_1 and T_2 displace distances δ_1 and δ_2 respectively parallel to the *z*–axis towards the coordinate's origin *O*. The quantity $\delta = \delta_1 + \delta_2$ is called the normal approach or the interference (Adams & Nosonovsky, 2000). In addition to deformation, the contact pressure also causes internal or subsurface stresses (Johnson, 1987).

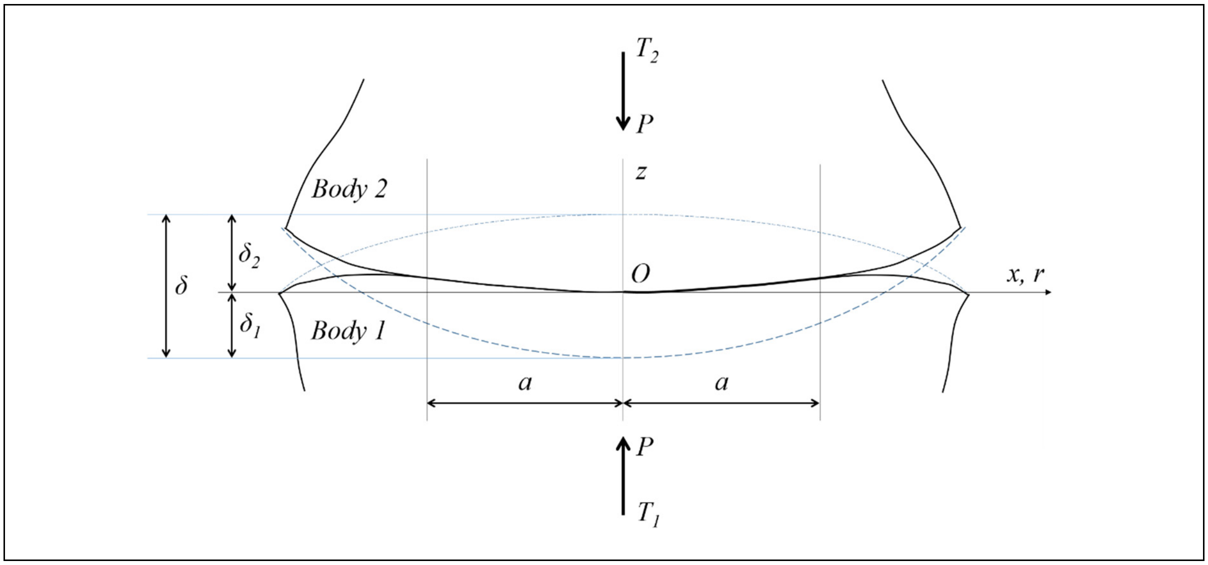

Figure 1.1 Hertz contact of two nonconforming elastic bodies
Reproduced from Adams & Nosonovsky (2000, p. 432)

Calculation of Hertzian parameters including the maximum pressure and the contact area is available in many references and can be used as a tool for verifying the numerical results.

Although, the Hertz calculations might not be accurate for some practical problems, but its results are very close to reality.

1.2.2 Boussinesq's results for a Half-space

Boussinesq and Cerruti solved the problem of point loading on a half-space using potential functions (Johnson, 1987). Using Boussinesq's results for a half-space, it is possible to calculate the normal deformation at any point in a half-space including its surface. Eq. (1.2) shows the formula for calculating the normal displacement at any point in a half-space caused by applying pressure on an area *A* of the half-space surface (de Mul, Kalker, & Fredriksson, 1986).

$$\begin{aligned} w_E(x,y,z) = \frac{(1+v)}{2\pi E} \iint_A \ P(\xi,\zeta)\Bigg(& \frac{z^2}{\left((x-\xi)^2+(y-\zeta)^2+z^2\right)^{3/2}} \\ & + \frac{2(1-v)}{\sqrt{(x-\xi)^2+(y-\zeta)^2+z^2}}\Bigg) d\xi d\zeta \end{aligned} \tag{1.2}$$

In this formula, w_E is the normal displacement at the surface, *z* is the depth from the surface, $P(\xi,\zeta)$ is the distributed pressure applied on the area *A* of the half-space surface, (ξ,ζ) are local coordinates, v is the Poisson ratio and *E* is Young's modulus. This formula only considers the pressure. Shear forces and thermoelastic effects are not included.

1.2.3 Compatibility Equation

Eq. (1.3) defines the relation between the initial separation *g* of bodies *a* and *b* from the contact plane and the linear elastic deformation of the solids (w_{E_a}, w_{E_b}). In a dry contact this equation gives the contact pressure. In this equation, α represents the mutual approach of the bodies (de Mul et al., 1986 ; Hartnett, 1980).

$$\begin{cases} w_{E_a} + w_{E_b} + g_a + g_b = \alpha & ,P > 0 \\ w_{E_a} + w_{E_b} + g_a + g_b > \alpha & ,P = 0 \end{cases} \tag{1.3}$$

In hydrodynamic contacts like EHL, usually the Reynolds equation gives the pressure while a modified complimentary equation gives the lubricant film thickness of the lubricated contacts (Greenwood & Kauzlarich, 1973 ; Najjari & Guilbault, 2014).

1.2.4 Stress Field

One of the most important issues in any moving contact is the failure, which is mostly referring to wear, scuffing and similar problems like pitting. The start of most of these failures is due to passing some stress threshold; therefore, in most studies one of the goals is to identify the stress field. This is not bound to a specific type of contact. Theory of elasticity helps in finding internal stresses based on the applied surface stresses (Stachowiak & Batchelor, 2014).

A map of the stress field can be used for predicting the point of crack growth or the point where plasticity happens first (Adams & Nosonovsky, 2000). It can also be used for other purposes like defining the depth for a contact that is being simulated by the half-space assumption (de Mul et al., 1986) or defining quarter space correction factor for the half-space based methods (Guilbault, 2011).

1.3 Heat

Generation of heat in mechanical contacts happens for different reasons. Four of the most common types of contact heat generation are frictional and electrical heating for dry contacts as well as shear and compression heating for lubricated contacts. Some of these types might happen simultaneously (Bansal, 2009 ; Mihailidis et al., 2013 ; Sukumaran, Baets, & Fauconnier, 2018 ; W. Z. Wang et al., 2006). Heat generation has diverse effects on the behavior of the contact in general and more specifically in physical properties of the lubricant (Greenwood & Kauzlarich, 1973 ; Najjari & Guilbault, 2014) or the thermal response of the contacting bodies (Barber, 1971 ; J. R., Barber, 1982).

1.3.1 Frictional heat generation in dry contacts

Frictional heating is the conversion of kinematic energy to thermal energy during a friction process. The produced energy depends on intrinsic parameters like material properties of the contacting bodies and the external condition parameters applied to the contact like load and sliding speed. Although these parameters vary for each specific contact, their heat generation (q) is generally calculated by the same formula (Eq. (1.4)) (Sukumaran et al., 2018).

$$q = \mu PU \tag{1.4}$$

In Eq. (1.4), μ is the coefficient of friction, U is the sliding velocity, and P is the contact pressure.

1.3.2 Electrical heat generation in dry contacts

The electrical heat generation happens due to a phenomenon called Joule or Ohmic heating. When electrical current passes through a conductive material or the contact between to conductors, by overcoming the electrical resistance it produces thermal energy (Bansal, 2009). In the case of electrical contact, this heat generation is reversely related to the contact pressure (M. G. Cooper, B. B. Mikic, 1969). Eq. (1.5) gives the general formula for the electrical heat generation (q).

$$q = \frac{R_c I^2}{A} \tag{1.5}$$

In this equation, R_c is the electrical contact resistance, I is the electrical current and A is the contact area.

1.3.3 Shear heating in lubricated contacts

In TEHL contacts, the heat generation is usually dominated by viscous shear heating. Overcoming the shear stress in lubricant layers produces heat. Eq. (1.6) gives the shear heating term solved in TEHL energy equation (Greenwood & Kauzlarich, 1973 ; W. Habchi & Vergne, 2015).

$$q_{shear} = \eta \left[\left(\frac{\partial u_f}{\partial z} \right)^2 + \left(\frac{\partial v_f}{\partial z} \right)^2 \right] \tag{1.6}$$

where η is the dynamic viscosity of the lubricant, u_f is the lubricant's velocity in rolling direction and v_f is the lubricant's velocity in lateral direction.

1.3.4 Compressive heating in lubricated contacts

In TEHL contacts, where the purely rolling condition applies, the compressive heating of the lubricant can become at least equally as important as shear heating. The compressive heating is a consequence of a pressure build-up at the inlet of TEHL contacts that leads to a lubricant compression accompanied by a generation of heat. At the exit, the pressure drop causes lubricant decompression acting like a heat sink. This combined heating/cooling mechanism which is caused by lubricant compression/decompression is referred to as "compressive heating". Eq. (1.7) gives the compressive heating term solved in TEHL energy equation (W. Habchi & Vergne, 2015).

$$q_{Comp} = \beta T \left(u_f \frac{\partial P}{\partial x} + v_f \frac{\partial P}{\partial y} \right) \tag{1.7}$$

where β is the coefficient of thermal expansion.

1.4 Thermo-elasticity

The thermoelastic deformations on a half-space have already been studied for a while. In 1979, Burton produced a thermoelastic numerical model for a frictionally heated contact. He conducted experiments to compare the results with his model (Burton, 1980). Around the same time, Barber proposed transient analytical model for a thermoelastic contact to predict the beginning of the thermoelastic instability (Barber, 1980). In 2000, Liu and Wang suggested a model for simulating a 2D thermoelastic frictional contact and proposed some analytical formulas (G. Liu & Wang, 2000). Recently, Barber et al. also studied thermoelasticity of a stagnated Hertzian contact in 2009 (Jang, Cho, & Barber, 2009), where the friction was not considered. Barber (Barber, 1971) also studied the thermoelastic effects of a heat source over a half space. Bryant (Bryant, 1988) performed a similar study for a moving heat patch.

As the name entails, a half-space is a semi-infinite matter. Therefore, no matter how long a heat source is applied on that, it will continue absorbing the heat and, as a result, achieving a steady state is intrinsically impossible. Therefore, if a steady state heat source is applied on the surface of a half-space, the thermoelastic deformation is in fact time dependent and converges to infinity (Figure 1.2-a). Therefore, Barber (Barber, 1971) proposed the definition of a heat affected zone radius (s_0) so that the thermoelastic displacement can be practically defined in steady state problems (Figure 1.2-b).

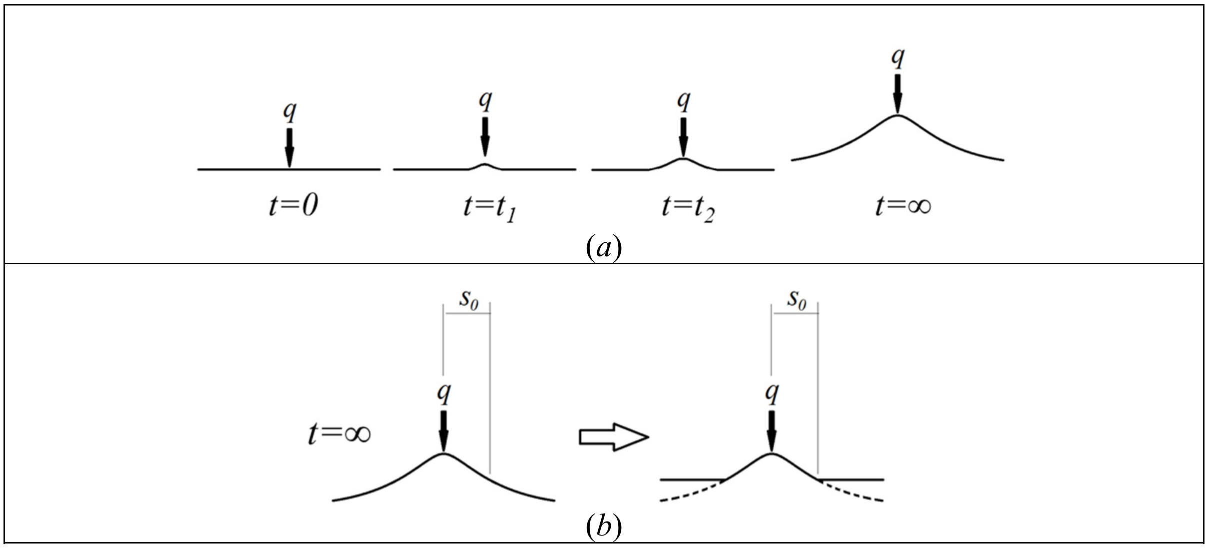

Figure 1.2 a) Time convergence of thermoelastic displacement, b) Steady state thermoelastic displacement

Barber’s displacement equation for a half-space is:

$$w = \frac{q\alpha(1+\nu)}{2\pi k}\log(s_0/s) \tag{1.8}$$

where α, k, ν are respectively the coefficient of thermal expansion, thermal conductivity, Poisson’s ratio of the material and s is the distance from the applied heat source.

1.5 Free-edge

In many contacts like textured surfaces (Manser et al., 2019 ; Siripuram & Stephens, 2004 ; Wakuda, Yamauchi, Kanzaki, & Yasuda, 2003) or rollers (Z. Liu et al., 2019 ; Najjari & Guilbault, 2014), the contact gap changes abruptly. When half-space based simulation methods like SAM are employed, free-edges cause considerable deviation in the contact results (Guilbault, 2011 ; Keer et al., 1983 ; Yalpanian & Guilbault, 2020). These deviations are introduced to the results by the half-space assumption for the normal displacement calculations. Half-space assumption leaves unreal shear and normal stresses on the free-surfaces because of the superfluous constraints. Researchers have proposed different methods to relieve the constraints applied to the free-surface by half-space assumption. Hetényi (Hetényi, 1960, 1970) and Keer et al. (Hanson & Keer, 1995 ; Keer et al., 1983) developed different methods to treat the aforementioned problem. They introduced a complicated, time consuming and considerably precise method for capturing the effects of the free-surface. Mul and Fredrikson (de Mul et al., 1986) proposed a simple mirroring technique, which was used later by other researchers (Figure 1.3). Their method relieves the shear stress on the free-surface but leaves the normal stress.

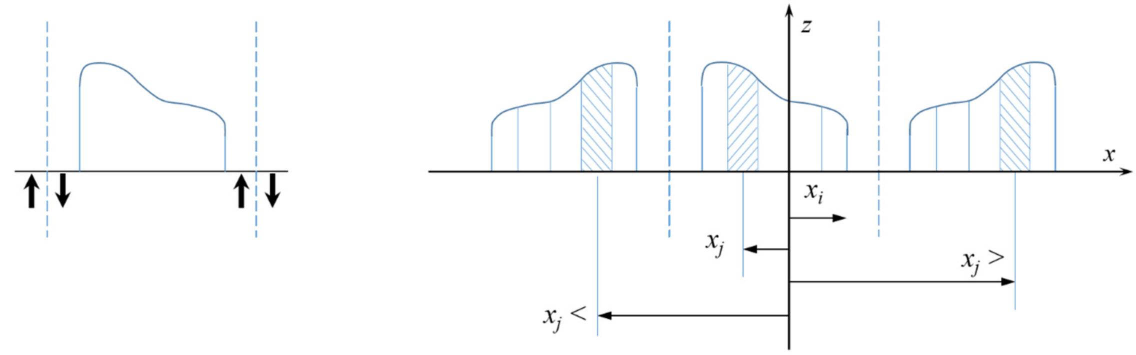

a) Original half-space situation *b) Finite length adjustment by mirroring*

Figure 1.3 Schematics of the method proposed by Mul and Fredrikson for removing the shear stress from the free-surface
Reproduced from de Mul et al. (1986, p. 146)

Guilbault suggested an overcorrection factor (Eq. (1.9)) for their mirroring technique in order to account for the normal stress as well (Guilbault, 2011). His method is almost as precise as the methods proposed by Hetényi (Hetényi, 1960, 1970) and Keer et al. (Hanson & Keer, 1995 ; Keer et al., 1983) while being simpler and far less time consuming. To eliminate the remaining normal stress, he balanced out the normal stress in a cyclic process until the remaining stress was negligible (Figure 1.4).

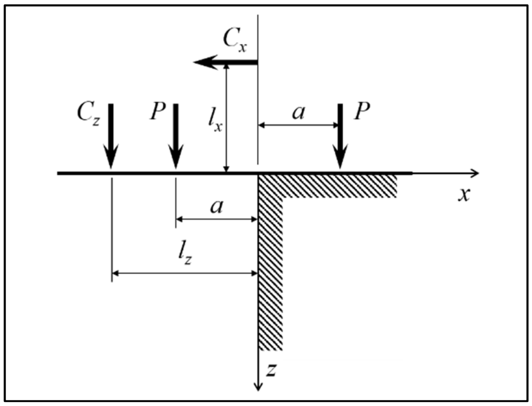

Figure 1.4 Free edge correction process proposed by Guilbault
Reproduced from Guilbault (2011, p. 4)

$$\psi = 1.29 - \frac{1}{(1-v)}[0.08 - 0.5v] \tag{1.9}$$

Since only the free-edge treatments for non-thermoelastic straight edges existed, the half-space based works that studied the asperities usually consider only continuous profiles with no free-edges that could cause deviation in the results (W. Z. Wang et al., 2006 ; X. Wang et al., 2017).

1.6 Lubricant Properties

In normal circumstances, most of the lubricant properties can be considered as constants but, when there are considerable changes in conditions like pressure and temperature, their dependencies cannot be ignored. Two of the most important physical properties of a lubricant that strongly depend on pressure and temperature are viscosity and density. The following paragraphs briefly explain the dependency of these lubricant properties.

Two of the most commonly used viscosity relations for EHL calculations are Barus' and Roeland's Viscosity-Pressure-Temperature relations. Houpert mentioned (Houpert, 1985) that Barus' viscosity relation has been experimentally confirmed to be valid at low pressures, yet for high pressures, Roeland's relation is recommended. Therefore, Roelands' relation is widely used for EHL simulations (Houpert, 1985). Eq. (1.10) shows Roeland's viscosity equation (Najjari & Guilbault, 2014).

$$\eta_{Roeland} = \eta_0\, exp\left\{[\ln(\eta_0) + 9.67]\left[-1 + (1 + 5.1 \times 10^{-9} P)^{z_1}\left(\frac{T - 138}{T_0 - 138}\right)^{-s_1}\right]\right\} \tag{1.10}$$

where, z_1 and s_1 are Roelands' parameters defined for each lubricant and are considered constant at any pressure and temperature. η_0 is the initial viscosity, T_0 is the initial temperature, T is the contact temperature and P is the contact pressure.

The influence of severe shear conditions leading to a shear-thinning response of the lubricant is important. It is often described by the Carreau's expression (Eq. (1.11)) (Marx, Fernández, Barceló, & Spikes, 2018 ; Yasuda, Armstrong, & Cohen, 1981). Under low shear rates ($\dot{\gamma}$), Newtonian lubricants present a shear independent viscosity (η), while at high shear rates, the viscosity is a function of the shear rate itself and, occasionally, a second Newtonian constant viscosity (η_∞). Bair and Khonsari (Bair & Khonsari, 2006), based on their observation of the difference between film thickness of different lubricants, described the lubricant's behavior by Carreau's expression as follows.

$$\mu = \eta_\infty + (\eta - \eta_\infty)\left[1 + \left(\frac{\eta\dot{\gamma}}{G}\right)^2\right]^{(n-1)/2} \tag{1.11}$$

Since generally the power-law region does not fully develop, Guilbault (Guilbault, 2013) considered the same assumption and used the following equation instead.

$$\mu = \eta\left[1 + \left(\frac{\eta\dot{\gamma}}{G}\right)^2\right]^{(n-1)/2} \tag{1.12}$$

Many researchers used modified versions of Carreau's expression as well; Habachi et al. used Carreau–Yasuda equation (W. Habchi et al., 2010).

The limiting shear stress is another important concept that is used widely in EHL analysis (Wan & Wong, 2009 ; Y. Zhang & Wen, 2002). It is recognized that τ_L is nearly proportional to the pressure (*P*), and influenced by the temperature (Guilbault, 2013). Equations similar to Eq. (1.13) are often used for τ_L modeling, where the ratio Λ has a value around 0.04–0.08.

$$\tau_L = \Lambda P \tag{1.13}$$

Taking into account the limiting shear stress effect, Eq. (1.14) offers a good rheological model for viscosity:

$$\mu = min\left[\eta\left[1 + \left(\frac{\eta\dot{\gamma}}{G}\right)^2\right]^{(n-1)/2}, \frac{\Lambda P}{\dot{\gamma}}\right]. \tag{1.14}$$

As for the density–pressure–temperature relationship, Dowson's formula is commonly used in many simulations (Ghosh & Hamrock, 1983 ; Khan, Sinha, & Saxena, 2009 ; Najjari & Guilbault, 2014). Eq. (1.15) shows Dowson's density relation (Dowson, 1997).

$$\rho_{Dowson} = \rho_0\left[1 + \frac{0.6\times10^{-9}P}{1+1.7\times10^{-9}P}\right]\left(1 - b_d(T - T_0)\right). \tag{1.15}$$

In Eq. (1.15), ρ_0 is the initial density and b_d is Dowson's thermal constant.

1.7 Hydrodynamics (Reynolds Equation)

For the first time, Osborne Reynolds analyzed the lubrication of bearings, and described the connection between bearing geometry, load and motion with the viscosity of the lubricant and initiated the subject of lubrication hydrodynamics (Guilbault, 2013). Reynolds equation describes behavior of the thin layer of lubricant in a lubricated contact. As mentioned earlier, in a lubricated contact, instead of the complimentary equation, Reynolds equation calculates the pressure and the complimentary equation gives the lubricant film thickness (Dowson, 1997 ; Najjari & Guilbault, 2014). Reynolds equation simplifies the general Navier-Stokes equation for fluid dynamics by ignoring the lubricant velocity and pressure variation across the film (Peiran & Shizhu, 1990). Eq. (1.16) shows the generalized Reynolds equation for the steady state problems (Najjari & Guilbault, 2014 ; Peiran & Shizhu, 1990).

$$\frac{\partial}{\partial x}\left(\frac{\rho h^3}{\eta}\frac{\partial p}{\partial x}\right)+\frac{\partial}{\partial y}\left(\frac{\rho h^3}{\eta}\frac{\partial p}{\partial y}\right)=12\bar{U}\frac{\partial}{\partial x}(\rho h)+12\bar{V}\frac{\partial}{\partial y}(\rho h) \qquad (1.16)$$

where h is the film thickness, $\bar{U}$ is the average lubricant velocity in rolling direction and $\bar{V}$ is the average lubricant velocity in axial direction. The two terms in the left side of the equation refer to Poiseuille flow and the two terms at the right side refer to Couette flow. Najjari and Guilbault used a variation of the Reynolds equation (Eq. (1.17)) to solve the 3D EHL problem of a finite line contact considering different crown shapes for a roller bearing (Najjari & Guilbault, 2014).

$$\frac{\partial}{\partial x}\left(\frac{\rho h^3}{\eta}\frac{\partial p}{\partial x}\right)+\frac{\partial}{\partial y}\left(\frac{\rho h^3}{\eta}\frac{\partial p}{\partial y}\right)=12\bar{U}\frac{\partial}{\partial x}(\rho h) \qquad (1.17)$$

Khan et al. (Khan et al., 2009), Ghosh and Hamrock (Ghosh & Hamrock, 1983) and many other researchers have also used other variations of Reynolds equation.

1.8 Energy Equations

Energy equations are derived from a general form based on the conditions and the assumptions. Energy equation can be derived for both solids and lubricants. Energy equation for solids can simply be written as (Incropera & De Witt, 1981):

$$k\frac{\partial^2 T}{\partial z^2} = \rho C_p u \frac{\partial T}{\partial x} \tag{1.18}$$

In comparison with solids, for lubricants, energy equation is usually more complicated. The same as Reynolds equation, energy equation for lubricants is derived from a more general form based on the conditions and the assumptions. Eq. (1.19) presents the general form of energy equation (W. Habchi & Vergne, 2015).

$$\begin{aligned} -\frac{\partial}{\partial z}\left(k\frac{\partial T}{\partial z}\right) + \rho c\left(u_f\frac{\partial T}{\partial x} + v_f\frac{\partial T}{\partial y}\right) \\ = \beta T\left(u_f\frac{\partial P}{\partial x} + v_f\frac{\partial P}{\partial y}\right) + \eta\left[\left(\frac{\partial u_f}{\partial z}\right)^2 + \left(\frac{\partial v_f}{\partial z}\right)^2\right] \end{aligned} \tag{1.19}$$

where ρ is the lubricant density and c is the lubricant's thermal capacity.

The common heat transfer assumption in thermal EHL is neglecting the heat convection across the lubricant film and the heat conduction along the film. By assuming that the heat transfer coefficient is constant, Najjari and Guilbault simplified the energy equation (Eq. (1.20)) to study the free-edge effect and the effect of different crowns on thermal EHL of a line contact (Najjari & Guilbault, 2014).

$$k\frac{\partial^2 T}{\partial z^2} = \rho C_p u \frac{\partial T}{\partial x} - \beta T u \frac{\partial P}{\partial x} - \eta\left(\frac{\partial u}{\partial z}\right)^2 \tag{1.20}$$

Greenwood concluded (Greenwood & Kauzlarich, 1973) from Crook's work (Crook, 1962) that the principal mechanism of heat loss is conduction across the inlet to the roller surfaces, while convection along the oil film is only important where the oil film temperatures are very low. Crook (Crook, 1962) concluded that, in pure rolling, the temperatures arising from the friction are confined to the entry side, ahead of the high pressure region.

Guilbault (Guilbault, 2013) mentioned that the combination of high pressure and shear stress could result in a layered lubricant film. The lubricant being layered means that some regions exhibit a solid-like behavior and some others accommodate the shear strain. The shear layer of the lubricant presents a liquid like behavior. He assumed that the heat generation only happens in the shearing layer.

1.8.1 Boundary Conditions

Each researcher applies proper boundary conditions according to the state of the problem they have prepared for their work. For most cases, the boundary condition assumptions are as follows (Najjari & Guilbault, 2014):

$$T_a|_{z_a=-3w_h} = T_0 \tag{1.21}$$

$$T_b|_{z_b=-3w_h} = T_0 \tag{1.22}$$

$$k_a \frac{\partial T}{\partial z_a}\bigg|_{z_a=0} = k_a \frac{\partial T}{\partial z}\bigg|_{z=0} \tag{1.23}$$

$$k_b \frac{\partial T}{\partial z_b}\bigg|_{z_b=0} = k_a \frac{\partial T}{\partial z}\bigg|_{z=0} \tag{1.24}$$

in which the constant w_h is the Hertzian width and indexes *a* and *b* represent each body.

1.9 Elastohydrodynamic Lubrication (EHL)

As Stribeck's graph shows (Figure 1.5), there are three main categories in lubricated contacts: Hydrodynamic, Mixed and Boundary lubrications (Zulkifli, Kalam, Masjuki, Shahabuddin, & Yunus, 2013). In hydrodynamic lubrication regime, there is no direct solid contact, while the mixed lubrication regime is partly hydrodynamic and partly direct solid contact. In boundary lubrication, direct solid contact happens all over the contact area.

The normal EHL is classified under hydrodynamic contact category, while the starved EHL is classified under mixed contact category. High pressure, in comparison with the elasticity modulus of contact bodies, results in change from normal hydrodynamic lubrication to EHL. The concept of EHL has been studied for more than fifty years.

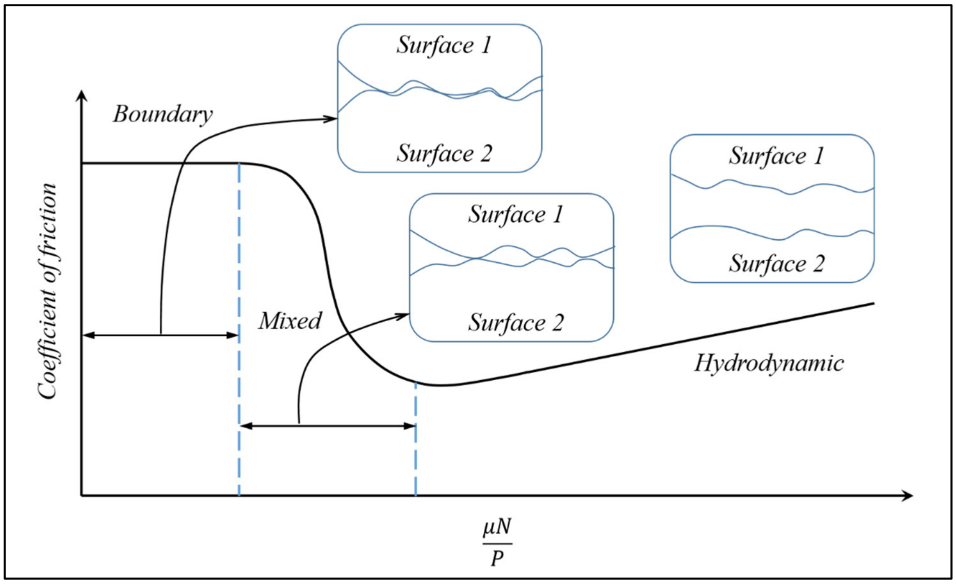

Figure 1.5 Stribeck's curve diagram
Reproduced from Zulkifli et al. (2013, p. 168)

EHL combines hydrodynamic lubrication (hydrodynamics) and elastic deformation (piezoelasticity) of the contacting bodies under high pressures (load). In EHL, the lubricating films are very thin, in the range of 0.1 to 1 µm, but they separate the interacting surfaces, resulting in a significant reduction of wear and friction (Stachowiak & Batchelor, 2014). Dowson (Dowson & Higginson, 1959) indicated that when the loading is high, the film thickness is small compared to the local elastic displacements, as a result, except near the edges of the thin film zone, the pressure must be close to the Hertzian pressure of the dry contact (Figure 1.6).

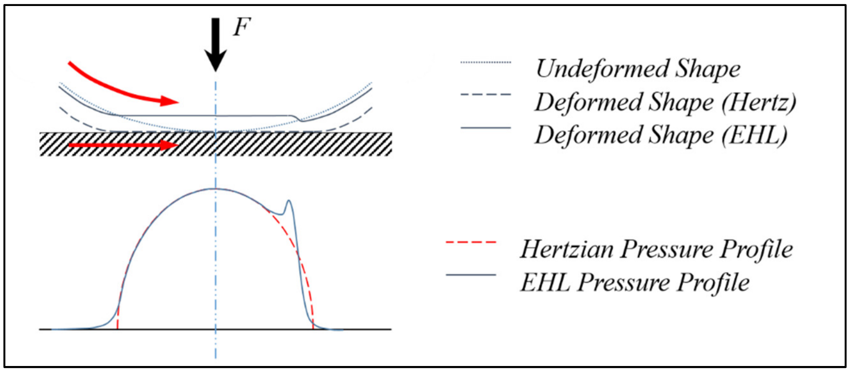

Figure 1.6 Schematic view of EHL and Hertzian Contacts

Grubin (GRUBIN, VINOGRADOVA, & KETOVA, 1949), in his pioneering work, introduced the elastic deformation of the solids and the piezoviscosity of the lubricant in the hydrodynamic calculations. By numerically solving a simplified problem, he was able to derive the first EHL regression formula for central film thickness calculations. He also speculated about the existence of the pressure spike at the outlet of the contact. Blok and Cameron argued that Ertel is the true originator of the work; therefore, the work is referred as Ertel–Grubin (Morales-Espejel & Wemekamp, 2008).

In 1972, Greenwood improved Grubin's work by starting from the elastic pressure distribution for an off-center flat instead of Hertzian pressures (Greenwood, 1972). In 1975, Hamrock and Dowson did a numerical analysis on isothermal elastohydrodynamic lubrication of a point contact (Hamrock & Dowson, 1976). In 1985, Haupert proposed new calculations for traction force in EHL contacts (Houpert, 1985). Hamrock and Ghosh studied thermal aspects of an elastohydrodynamic lubrication for a line contact in 1983 (Ghosh & Hamrock, 1983). Recently, Guilbault developed a thermal EHL model for a 2D infinite line contact using layered lubrication film assumption in which he considered heat generation and heat transfer in different layers (2013) (Guilbault, 2013). Mihailidis et al. proposed a 3D model for a starved thermal EHL for a line contact (Mihailidis et al., 2013). They introduced a fraction factor to consider the limit of starvation in EHL contact. Most of these studies considered only the effect of thermal considerations on the lubricant. Only a few studies considered the effect of thermoelasticity in thermal EHL (W. Z. Wang et al., 2006 ; Xu & F. Sadeghi, 1998).

In 1998, Xu and Sadeghi studied thermal EHL of a thrust bearing considering thermal distortion due to temperature rise using finite element method (Xu & F. Sadeghi, 1998). Wang et al. also considered thermoelasticity for a mixed lubricated point contact ignoring the viscosity and density variations across the film (W. Z. Wang et al., 2006). The attention to thermoelasticity in thermal EHL is relatively new and still there are works to be done in this field.

Finite element analysis (FEA) is also an accepted simulation approach for contact simulation (Bachtar et al., 2006 ; Chatterjee & Sahoo, 2014 ; Sahoo & Ghosh, 2007 ; Yang & Komvopoulos, 2005). Employing FEA commercial software is not that simple, especially when it comes to the contribution of factors like thermoelasticity and/or FSI (Fluid Solid Interaction) (Gropper et al., 2016 ; Lindemann, Skalski, Wlosinski, & Zimmerman, 2006 ; Reddy, 2015). It also leads to prohibitive mesh preparation times and computational costs. Because of these FEA limitations, SAM is more sought out in contact problems (Hanson & Keer, 1995 ; Hartnett, 1980 ; Hetényi, 1960, 1970 ; Keer et al., 1983 ; J. Li & Berger, 2003 ; Junshan Li & Berger, 2001). Nonetheless, FEA is a rather helpful and widely accepted tool for validation of other methods (Guilbault, 2011). Experimental investigation of contact problems is usually entwined with considerable difficulties (Gohar & A. Cameron, 1963 ; Wymer & Cameron, 1974).

1.10 Experimental Measurements

Experimental studies performed on contacts can be divided into two specific categories, Dry contacts and lubricated contacts, specifically EHL contacts. The following sections present some of the works that has been done in each of these categories.

1.10.1 Dry Contact

Many researchers performed experimental measurement of the contact pressure using pressure sensitive films; like the work of Belforte et al. (Belforte, Conte, Bertetto, Mazza, & Visconte, 2009) who measured contact pressure for seal connection. Zhang et al. (M. Zhang, Suo, Jiang, & Meng, 2018) also performed an experimental contact pressure measurement of seals using sensitive films. Conte et al. (CONTE, MANUELLO, L.MAZZA, & C.VISCONTE, 2006) used a similar approach for a pneumatic seal contact pressure measurement. As Figure 1.7 shows, these pressure sensitive films that are made by PRESCALE Company are mostly useful for detecting the irregularities in a contact surface rather than giving a precise pressure profile. The precision of these kinds of films is not so high and, especially, its precision is rather inadequate for small contacts. Another short coming of these films for study purposes is that the pressure range that each pressure sensitive film covers is limited; for example, if a pressure profile contains 20 and 100 PSI in a single profile, the sensor film is not capable of capturing it. It can merely point out that a high pressure range exists. Figure 1.7 illustrates some sample results obtained from an “ultra low pressure” sensitive film (28-85 PSI) for the contacts between a cylindrical part with the external diameter of 15 mm and the internal hole diameter of 4 mm with; a flat surface (Figure 1.7-a) and another cylindrical part with the same outer diameter but without the internal hole (Figure 1.7-b). Both contacts are under an 8 Kg load. As Figure 1.7-b illustrates, an irregularity on the surface of one of the cylindrical parts is detected by the pressure sensitive film but the results are not conclusive enough to create a concrete pressure profile.

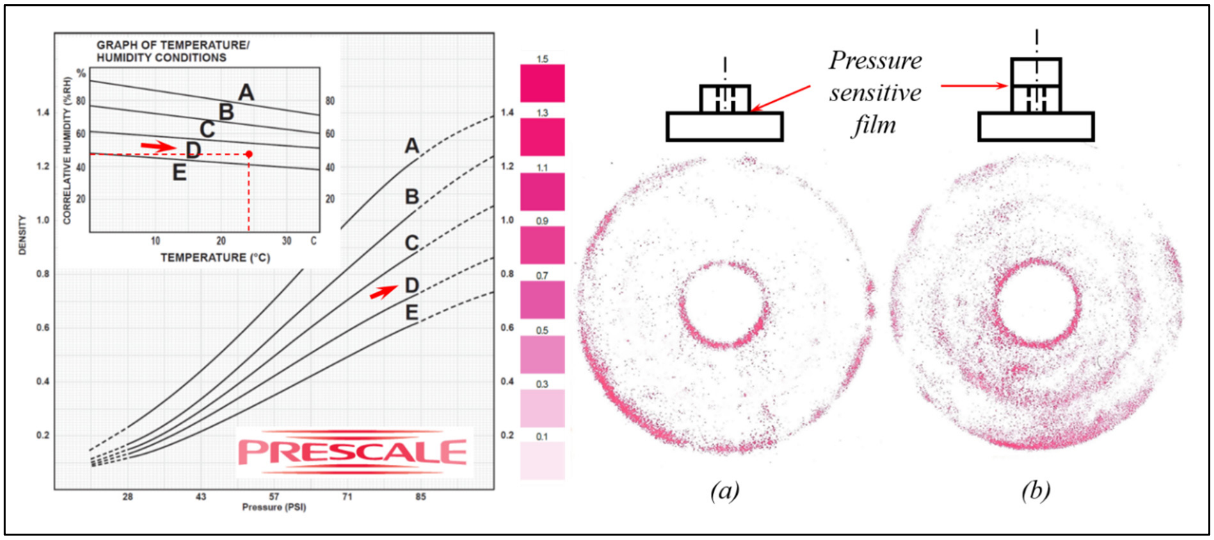

Figure 1.7 The results of the sensitive film obtained from a simple experiment

There are other experimental studies as well like the study performed by Guilbault (Guilbault, 2011). He used a rubber sheet and an aluminum cylinder to study the effect of free-edge on the contact area in a finite line contact.

1.10.2 Lubricated Contact (EHL)

Various elastohydrodynamic measurement techniques have been developed over the years. These techniques can be generally classified as electrical resistance, capacitance, X-ray, mechanical and optical interferometry methods (Stachowiak & Batchelor, 2014).

Gohar and Carmen (Gohar & A. Cameron, 1963) were the first ones to experiment on EHL by interferometry using a high reflective index glass and a steel ball. Otero et al. used an MPR tribological equipment developed by PCS-Instruments to validate their numerical results (Otero, Ochoa, Tanarro, Lantada, & Munoz-Guijosa, 2012). In their experiment, they measured the traction coefficient in thermal EHL while controlling the heat by an electric cartridge heater and fixing the load on the upper ring. Chu et al. (Chu, Hsu, Lin, & Chang, 2009) concluded that optical interferometry has been found to be the most widely used and successful method in measuring oil film. Hence, they used an inverse approach to improve the extracted data from optical interferometry.

Leeuwen et al. (van Leeuwen, Meijer, & Schouten, 1987) performed the local film thickness and temperature measurements in an eccentric cam-flat follower contact by means of miniature vapor deposited thin layer transducers. They measured film thickness by calculating the ohmic resistance or the capacitance of the film using a transducer on the follower, which was constantly being pushed over the cam by a spiral spring.

Necas et al. (Necas, Sperka, Vrbka, Krupka, & Hartl, 2015) used an experimental setup (Figure 1.8) for a ceramic ball and a glass disk under pure rolling based on Gohar's experiment in 1963 (Gohar & A. Cameron, 1963). The ball and disk could rotate independently so that different ratios of slide/rolling was possible. They developed and applied mercury lamp induced fluorescence. Their measured data did not exactly match the theoretical results, indicating that other parameters like thermal effects could influence the lubricant film.

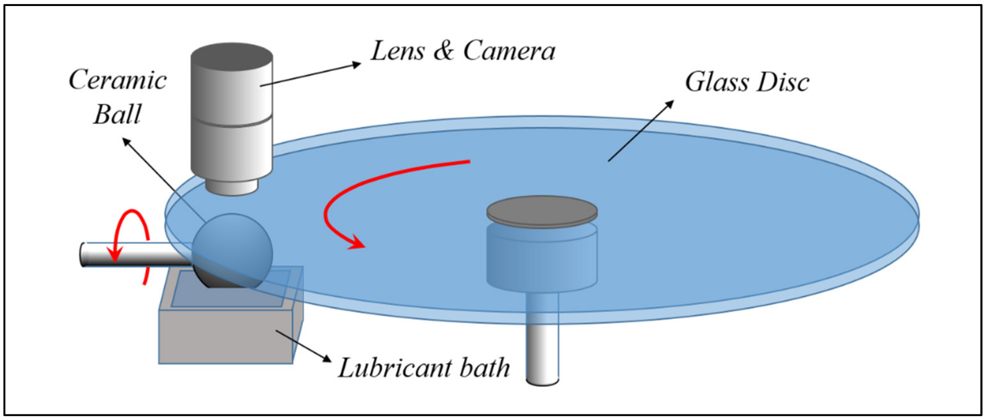

Figure 1.8 Necas' experimental setup for EHL film measurement
Reproduced from Necas et al.(2015, p. 822)

Svoboda et al. (Svoboda, Kostal, Kunak, & Krupka, 2014) also performed a similar experimental study of grease lubrication in a starved elastohydrodynamic lubricated (EHL) contact using optical interferometry. Their experimental setup was also based on a glass disk and a sphere or a barrel like roller.

As can be seen, in all these measurement techniques, the thermal effects or specifically the thermoelastic effects are not exactly distinguishable in the measurement. That will cause the experimental results to differ from the results obtained from numerical simulations, especially with the ones that ignore the thermal aspects or specifically thermoelasticity.

1.11 Numerical solution approaches

To determine the pressure distribution within the lubricant film, the process should solve Reynolds equation, the complimentary equation for film thickness, the equations for lubricant properties (viscosity, density …) and the load balance equation. The solution of energy equations give the temperature within the lubricant and the solid bodies. The viscosity, density, pressure and temperature are nonlinearly interconnected, so it is too complicated to be solved analytically.

Hamrock and Dowson (Hamrock & Dowson, 1976) were of the first researchers who used the aforementioned process for a 2D isothermal study using a simple Gauss-Seidel iteration scheme for pressure calculation. Others have further improved this numerical approach and extended the range of operating conditions and were able to surpass the limitations of Hamrock and Dowson's numerical model.

In general, the numerical simulation approaches employed for contact problems can be divided into two categories; the methods based on finite element analysis (FEA) and the half-space based semi-analytical methods (SAM). Figure 1.9 shows a general comparison of the SAM and FEA based methods. Some of the examples of the studies performed in both approaches are as follow.

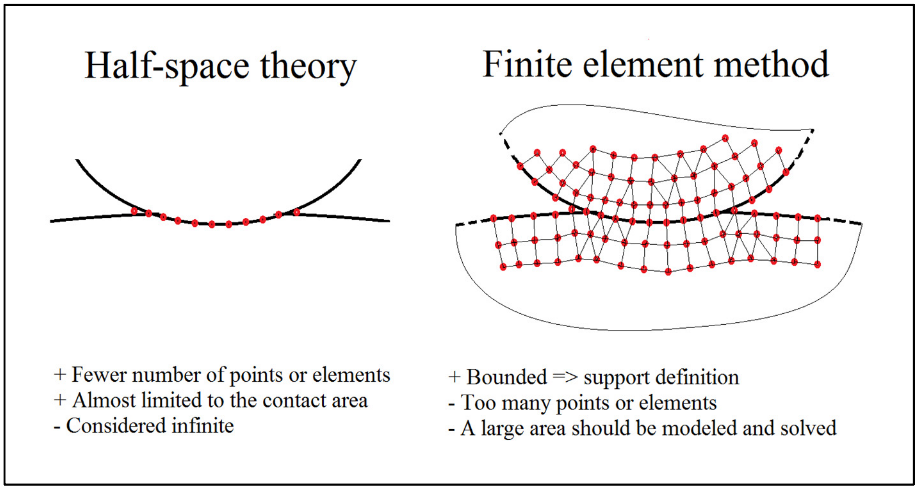

Figure 1.9 A general comparison between SAM and FEA based Methods

1.11.1 Researches that have employed SAM

Ghosh and Hamrock (Ghosh & Hamrock, 1983) used an isothermal approach similar to Hamrock's Method in order to find the pressure distribution as the initial guess for thermal cases. They used a standard central finite deference method. The system of simultaneous equations was solved by the standard Gauss-Seidel iterative method, yet they had difficulties evaluating the surface temperature near the pressure spike.

Venner and Napel (Venner & Napel, 1992a, 1992b) proposed a multilevel multigrid model called multilevel multi-integration technique for EHL of point contact. Later, Venner (Venner & Bos, 1994) adapted relaxation models to the multigrid model. Wang et al. (X. Wang et al., 2017) used a finite difference method while employing influence coefficient algorithms to calculate both the surface deformation and the temperature rise. The approach they used is called a semi-systemic approach. The basic idea of the semi-system approach is to consider the entraining flow term as a function of unknown nodal pressures. Thus, the construction of the coefficient matrix will utilize not only the pressure flow terms but the entraining flow term as well. Therefore, the diagonal dominance of the coefficient matrix is guaranteed even when the pressure flow becomes extremely weak or even zero. Moes (Moes, 1992) employed a similarity method for solving an EHL problem.

In the work of Wang et al. (W. Z. Wang et al., 2006) who considered thermoelasticity, after discretization of the computational domain, influence coefficients (ICs) were obtained for elastic deformation and temperature rise. Then, the discrete convolution and FFT (DC-FFT) method were used to speed up the calculations of elastic deformation and temperature rise. For thermoelastic deformations, since their equation was in frequency response function (FRF) mode, they needed to first convert the FRF to ICs, and then apply the DC-FFT method to obtain the normal thermoelastic deformation.

1.11.2 Researches that have employed FEA

Xu and Sadeghi (Xu & F. Sadeghi, 1998) applied FEA for solid parts and the same Gauss-Seidel finite difference method for the lubricant. In 2008, Habchi (Wassim Habchi, 2008) wrote his PhD thesis on application of finite element approach for solving EHL with Ultra-Low-Viscosity fluids. He studied thermal and Non-Newtonian effects. Habchi et al. (W. Habchi et al., 2010) used a model based on a finite element fully coupled resolution of the elastohydrodynamic equations and introduced special formulations in order to stabilize the solution of Reynolds equation at high loads. Hsiao et al. (Hsiao, Hamrock, & Tripp, 1999) also used FEA for modeling elliptical EHL contacts by an isothermal assumption employing Galerkin's weight function. Stupkiewicz (Stupkiewicz, 2009) employed FEA for soft EHL problem of a rod seal.

1.12 Common practical application

Some practical applications of a comprehensive contact analysis are in simulation of gears, textured bearings and lubricated bearings with feeding or pressure amplifying grooves. One example is Polyoxymethylene (POM) composite bearings that are suitable for high loads and low speeds. These kinds of bearings are in different forms like cylindrical bushes, flanged bushes, thrust washers or sliding plates (Figure 1.10). As Figure 1.10 demonstrates, the distinctive feature of such bearings is a pattern of cavities in the contact surface.

These cavity patterns help improve bearing characteristics, including and not limited to less heat generation. Therefore, there have been many studies focused on such textured contact surfaces. Morris et al. (Morris, Shahmohamadi, Rahmani, Rahnejat, & Garner, 2018) have done a comprehensive study on textured journal bearings. Manser et al. (Manser et al., 2019) have also worked on the influence of textured surface on journal bearings. They have studied different texture shapes and sizes. Tala-Ighil et al. (Tala-Ighil, Maspeyrot, Fillon, & Bounif, 2007) have studied the positioning and patterns of texture cavities in journal bearings. Siripuram and Stephens (Siripuram & Stephens, 2004) have done a similar study on textures of asperities for hydrodynamic lubrication. The studies that are being done on textured surfaces require a contact analysis method that is fast and reliable. The study presented in this thesis aims to provide a comprehensive contact analysis method that can be used for analysis of such textured contact surfaces.

As Figure 1.10 shows, the main feature of a textured contact surface is the pattern of cavities (or asperities (Siripuram & Stephens, 2004)) implemented on the surface. Some common surface projections of these cavities are circular and square. Due to presence of curved and straight free-edges in these cavities, common SAM is not capable of fully analyzing such contacts, especially while considering thermoelastic behavior of the surface material. By obtaining all the intended sub-objectives of this thesis, the proposed contact analysis method has the ability of handling thermal thermoelastic analysis of contacts, which are textured and have cavities with curved or straight free-edges.

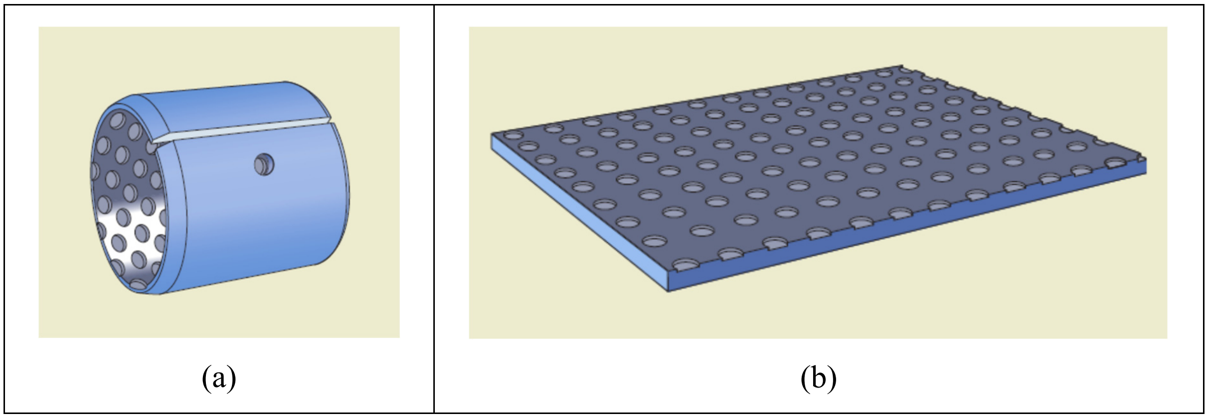

(a) (b)

Figure 1.10 POM Composite bearings; a) Straight cylindrical bushing with a lubrication hole, b) sliding plates
Taken from SKF Catalogue (2012, p. 4, 6)

Another example is the grooved shoe bearings that are usually designed for heavy duty operations with a relatively fast rotation speed (Figure 1.11). These kinds of bearings are used in a variety of industrial equipment like; tilting shoe journal bearings used in heavy duty ball mills that are being used in mining industry (SKF, s.d.) or the tilting pad thrust bearings used in ship industry to allow for more powerful engines and propellers (Stachowiak & Batchelor, 2014). They can also be found in other heavy duty rotating equipment like supports for turbines and generators that weigh over a hundred tons (Kingsbury Inc., 2019).

There have been many studies on the effect of implementing such grooves and their geometries on tilting pad bearings. Mikula (Mikula, 1985, 1988) studied different versions of grooved tilting pads and their pressure losses and temperature variations. Instead of performing a sole experimental study, in 2017, Varela et al. (Varela, García, & Santos, 2017) studied leading groove tilting pads using a numerical approach. Another application of the comprehensive contact analysis method that the study of this thesis intends to deliver is analysis of such grooved contacts. This method can expedite and facilitate studies on such grooved bearings.

As Figure 1.11 demonstrates, one of the important features of these bearings is the presence of different types of grooves. These grooves may have straight and/or curved free edges. Similar to the cases with textured surfaces, common SAM does not possess the capability of handling free-edges of the grooves, particularly while taking thermoelastic behavior of the surface material in consideration. The ability of handling thermal thermoelastic contacts with curved and/or straight free-edges renders the comprehensive contact analysis method proposed in this thesis very useful for fast analysis of such grooved contacts.

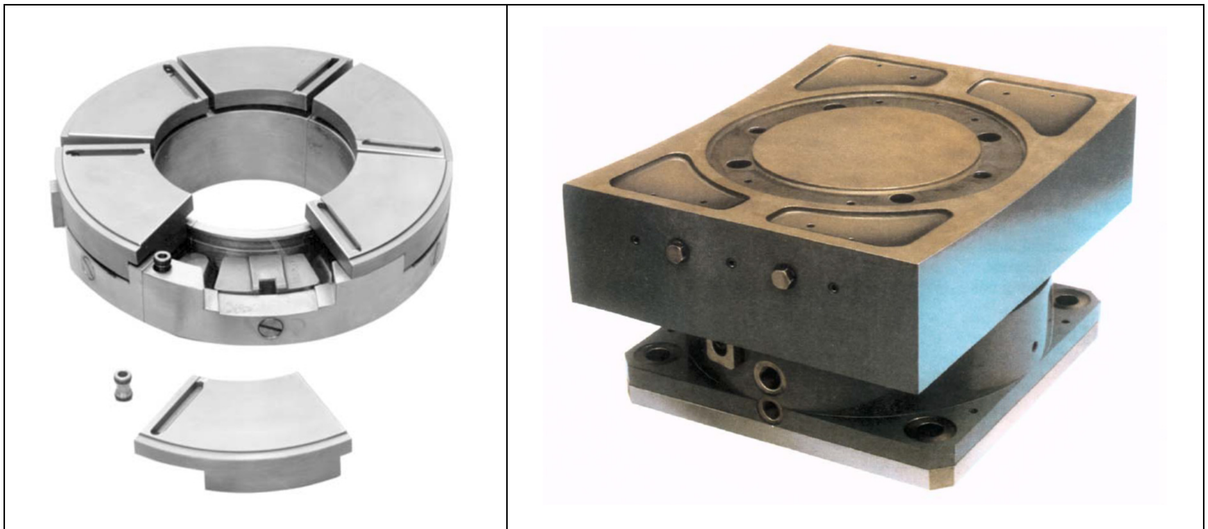

(a) (b)

Figure 1.11 Tilting shoe bearings; a) Leading edge groove thrust bearing (Taken from Kingsbury guide (2019, p. 12), b) Tilting pad journal bearing (Taken from SKF Catalogue (Hydrostatic shoe bearing arrangement)

Overall, literature review establishes the need for a comprehensive, fast, and reliable contact analysis method that can handle different non-plain contacts (Textured or grooved).

1.13 Summary

This review showed that there are some studies performed on steady state thermoelastic contacts, but they are not complete yet. In addition, the works performed on free-edges have only considered straight free-edges like the two ends of a finite cylinder while other types of free-edges like inside a circular hole or pit and around a circular asperity are ignored. To our knowledge, at the time of preparing this thesis, no study was reported on the consideration of free-edges in a half-space based method that considers thermoelasticity. Some of the works and results mentioned in this literature review help in filling the gaps mentioned for free-edge studies. The work of Mul et al. (Veress, Molnár, & Rohács, 2009) on basic mirroring technique and depth consideration is one of them. Another one is the result of Guilbault's work on free-edge to eliminate the normal stresses at the free-surface (Guilbault, 2011). Barber's work

(Barber, 1971) is specifically useful in integrating thermoelasticity to the basic half-space based SAM.

It can also be deduced from the literature review that there are only a few studies performed on thermal EHL, which considered thermoelasticity and they are limited and not suitable for contacts like finite roller contacts. Najjari's work on thermal EHL (Najjari & Guilbault, 2014) and Guilbault's work (Guilbault, 2013) on layered heat generation inside the lubricant give insight to the thermal EHL aspects including lubricant properties and shear heating relations.

CHAPTER 2

A FAST CORRECTION OF THE FREE SURFACE FOR CONTACT PRESSURE CALCULATION OF PROTRUSIONS WITH CURVED EDGES

Ali Yalpanian[a], Raynald Guilbault[b],

[a,b] Department of Mechanical Engineering, École de technologie supérieure, Université du Québec, 1100 Notre-Dame West, Montreal, Quebec, Canada H3C 1K3

Paper published in *Tribology International*, January 2020

2.1 Abstract

This study proposes a simple method for simulating contacts with curved edges. It develops a fast correction approach to eliminate the errors introduced on curved free surfaces by the half-space assumption in semi-analytical methods. The complete procedure first defines a counterbalance radius to eliminate the shear stress generated on free surfaces, and then introduces a correction factor for the counterbalance load to account for the normal stresses generated on free surfaces. A comparison with FEA results shows a 92% improvement after applying the shear correction and a greater-than-96% improvement after applying the complete correction (shear and normal stresses). Computational costs are also significantly lower than those required by FEA, and are at least 9 times so for the studied cases.

Keywords: Contact mechanics, Numerical analysis, Simulation

2.2 Introduction and literature survey

This study presents a simple method for including the effects of curved free edges in contact models based on half-space theory. The proposed method addresses a problem which is common in various contact problems, such as rotational friction welding (RFW) (RFW) (Jl, Renee, & Jacoby, 1991 ; W. Li, Vairis, Preuss, & Ma, 2016 ; Lindemann et al., 2006 ; Reddy,

2015) or patterned and textured contacts (D.B. Hamilton, 1966 ; Etsion, Kligerman, & Halperin, 1999 ; Gropper et al., 2016 ; Wakuda et al., 2003). Contact problems that involve simple geometries may be solved using Hertz theory (Hertz, 1896), which for its part, involves three basic assumptions:

1) The contact is frictionless;
2) The contact area is small as compared to the size of bodies;
3) The contact area is small as compared to the curvature radii of surfaces.

While the first assumption has the obvious consequence of restricting the load to a pressure, the two others involve less transparent simplifications: the second eliminates any possible influence by nearby boundaries, whereas the third assumes that the bodies may be viewed as half-spaces submitted to linear elastic strains only. Over the years, numerous approaches have also been developed for contact problems, and impose similar simplifications, while breaching the simplicity of the contact geometries (de Mul et al., 1986 ; Hartnett, 1980 ; S. Liu & Hua, 2009). Among these approaches, the Semi-analytical method (SAM) proposed by Hartnett (Hartnett, 1980) is very effective. This method takes advantage of Boussinesq’s half-space solution (Johnson K.L., 1985). Similar SAM methods have also been used for rough surfaces (Chen & Wang, 2009 ; Poon & Sayles, 1994 ; Tian & Bhushan, 1996 ; Willner, 2008). Although these methods may be applicable to almost any contact problem, they still present some limitations that must be addressed. For example, Hetényi (Hetényi, 1960, 1970) and Keer (Hanson & Keer, 1995 ; Keer et al., 1983) proposed different solutions to eliminate the effect of the shear and normal stress distributions generated on the free boundaries by the half-space assumption. de Mul et al. (de Mul et al., 1986) observed that the shear stress distribution greatly influences the loaded surface displacement, while the normal stress demonstrates fewer controlling effects. Therefore, a partial elimination which neglects the normal stress distribution influences should offer sufficient precision in most situations, while resulting in a significant reduction of calculation times. However, in sensitive applications, the effect of normal stresses may culminate in unacceptable displacement evaluation, especially close to the free boundaries. In such conditions, both shear and normal stress distributions should be eliminated. The solutions proposed in Refs. (Hanson & Keer, 1995 ; Hetényi, 1960, 1970 ;

Keer et al., 1983) for normal stress elimination, although very precise, are rather unsuitably time-consuming. Guilbault (Guilbault, 2011) proposed a simpler solution for normal stress elimination on straight free surfaces using a simple correction factor. This approach provides high precision levels without increasing calculation times, as compared to partial correction.

Finite element analysis (FEA) may also enable valuable simulations (Bachtar et al., 2006 ; Chatterjee & Sahoo, 2014 ; Sahoo & Ghosh, 2007 ; Yang & Komvopoulos, 2005). However, while employing FEA commercial software, could, on the one hand, be rather simple, on the other hand, FEA often leads to prohibitive mesh preparation times and computational costs. Moreover, additional drawbacks of FEA in contact problems arise with the analysis of phenomena such as thermoelasticity and conditions such as elastohydrodynamics (Gropper et al., 2016 ; Lindemann et al., 2006 ; Reddy, 2015) , where contributing thermal factors and FSI (Fluid Solid Interaction) should be considered. Due to these limitations, SAM is more commonly sought to deal with contact problems (Hanson & Keer, 1995 ; Hartnett, 1980 ; Hetényi, 1960, 1970 ; Keer et al., 1983 ; J. Li & Berger, 2003 ; Junshan Li & Berger, 2001). Nevertheless, FEA could be a considerably helpful tool for validating other methods. Actually, the difficulty encountered with experimental investigations of contact problems makes FEA a valuable and widely accepted validation aid.

The solutions available in the literature for releasing free surfaces in half-space-based methods are mostly targeted at planar free surfaces (Guilbault, 2011 ; Hetényi, 1970). However, there are also some practical contacts bordered by curved edges and curved free surfaces. Rotational friction welding (Jl et al., 1991 ; W. Li et al., 2016 ; Lindemann et al., 2006 ; Reddy, 2015) and textured contacts with cylindrical holes or protrusions (D.B. Hamilton, 1966 ; Etsion et al., 1999 ; Gropper et al., 2016 ; Wakuda et al., 2003) are good examples that still need to be addressed.

This paper develops a half-space-based method that accounts for curved free edges. This method involves two simple steps targeting the elimination of shear and normal stresses. The first step relates each radial contact position to a corresponding position outside the boundary in order to eliminate the half-space intrinsic shear stress present on the free surface; an external pressure applied at this position counterbalances the shear stress distribution. For straight boundaries, this external pressure would be known as a mirror pressure. This method gives a relation applicable to both cylindrical protrusions and cavities. Second, based on the procedure put forward in Ref. (Guilbault, 2011), the present study formulates a correction factor to be applied on the external pressure exerted in the first step to correct the shear stress. This correction factor aims at compensating for the influence of the normal stress distribution on the displacement.

The following section describes the basis of the SAM approach, while the next sections develop the shear and normal stress elimination processes. Finally, the last section validates the solution developed by comparing the predictions obtained for different contact problems with FEA results.

2.3 Half-space method basis

The Hartnett numerical method (Hartnett, 1980) applies the results of the Boussinesq half-space solution. This method assumes that the contact is part of a half-space, and is limited to linear deformation. Eq. (2.1) gives the normal displacement at point (x, y) due to a distributed pressure $P(\xi, \zeta)$ acting on the area A.

$$w(x,y) = \frac{1-v^2}{\pi E} \iint_{\mathrm{A}} \frac{P(\xi,\zeta)}{\sqrt{(x-\xi)^2+(y-\zeta)^2}} d\xi d\zeta \tag{2.1}$$

where w is the normal displacement, v is the Poisson ratio and E is the modulus of elasticity.

The Hartnett procedure includes a complimentary equation defining the relation between the existing initial separation g of bodies a and b from the contact plane as well as the linear deformation of the solids (w_a, w_b) (Eq. (2.2)). In this equation, α is the approach of the bodies. Figure 2.1 illustrates the variables.

$$\begin{cases} w_a + w_b + g_a + g_b = \alpha & ,P > 0 \\ w_a + w_b + g_a + g_b > \alpha & ,P = 0 \end{cases} \tag{2.2}$$

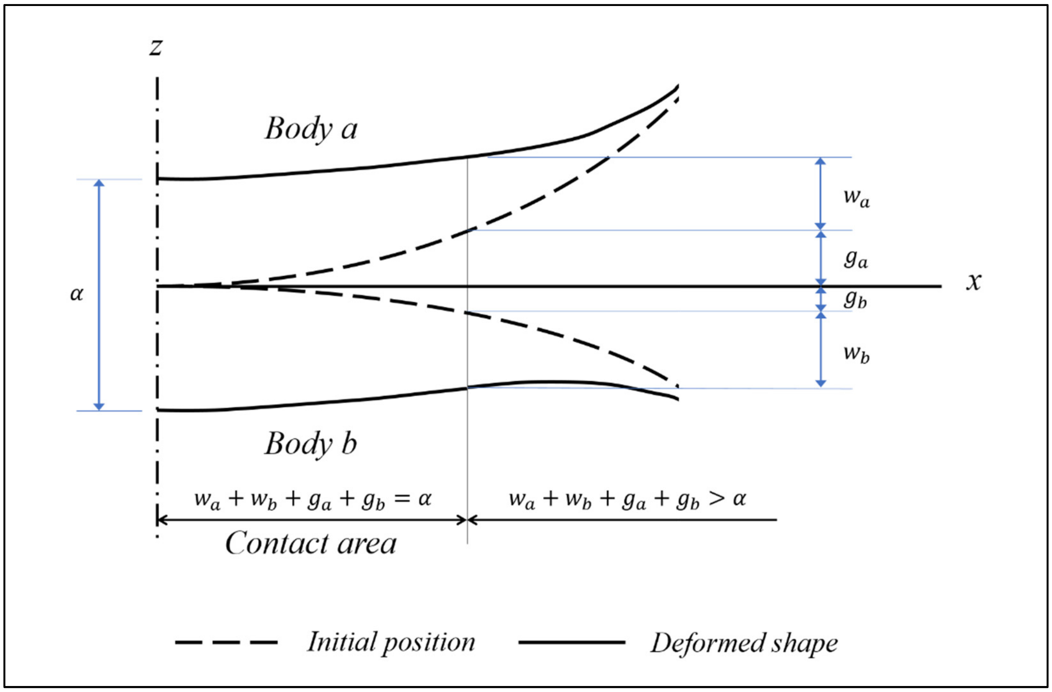

Figure 2.1 Physical representation of complimentary equation

2.3.1 Half-space numerical approach (Influence Factor)

In SAM, a blanket is divided into rectangular contact patches bearing uniform pressures. Hence, Eq. (2.2) transforms to:

$$\sum_{A} P_k \times f_{jk} = \alpha - g_{a\,j} - g_{b\,j}$$

where f_{jk} is a set of influence factors resulting from Eq. (2.1) and formulated by Eq. (2.3).

$$f_{jk}(x,y) = \left(\frac{1-{v_a}^2}{\pi E_a} + \frac{1-{v_b}^2}{\pi E_b}\right) \iint_A \frac{1}{\sqrt{(x-\xi)^2 + (y-\zeta)^2}} d\xi d\zeta \qquad (2.3)$$

where (*x, y*) are the coordinate locations of the center of the displaced patch *k* with respect to the center of the loaded patch *j* in a local frame.

2.3.2 Half-space stresses

The Boussinesq formula also provides the shear and normal stresses at a position (x, y, z) of a half-space where the point load F on the surface is located at the origin, while the z axis is inward and aligned with the surface normal. Eqs. (2.4) and (2.5) formulate these stresses, respectively:

$$\sigma_x = \frac{F}{2\pi}\left[\frac{(1-2v)}{d^2}\left\{\left(1-\frac{z}{c}\right)\frac{x^2-y^2}{d^2}+\frac{zy^2}{c^3}\right\}-\frac{3zx^2}{c^5}\right] \qquad (2.4)$$

$$\tau_{xz} = -\frac{3F}{2\pi}\frac{xz^2}{c^5} \qquad (2.5)$$

In these equations $d = (x^2 + y^2)^{\frac{1}{2}}$ and $c = (d^2 + z^2)^{\frac{1}{2}}$.

2.4 Free edge

An edge causes abrupt changes in the contact condition. Because of the half-space assumption, free surfaces lead to extreme pressure peaks in the Hartnett's SAM. These pressure rises originate from an artificial over-constraint of the free surface caused by the half-space internal shear and normal stress distributions generated onto them (Figure 2.2). As mentioned earlier, de Mul et al. (de Mul et al., 1986) indicated that the effect of shear stresses on the half-space surface displacement, and thus on the contact pressure profile, is considerably greater than the normal stress influence. Therefore, a partial elimination of the boundary stress could be adequate for most practical cases. More importantly, while the shear stress elimination with the mirroring process has a low incidence on the solution times, the normal stress cancelation leads to prohibitive calculations.

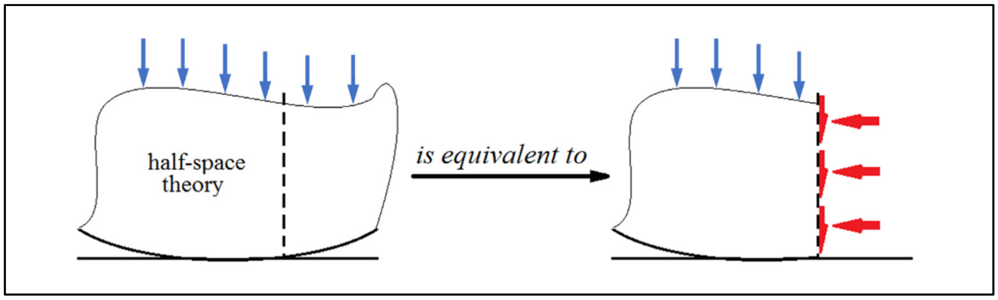

Figure 2.2 Effects of half-space assumption on free edges

The main idea underlying the procedure developed in Ref. (Guilbault, 2011) involves the use of a sequential calculation of normal stresses and their mirror corrections to establish the resulting displacements. The normal stress distributions are replaced by their equivalent forces. The final displacement assessed for the normal stress is introduced via a simple correction factor applied as a multiplier of the external pressure exerted to correct the shear stress effects; the resulting shear stress overcorrection compensates for the normal stress distribution influences. This study employs a similar approach.

2.5 Shear stress elimination on cylindrical free surface

Unlike the planar free surface case, the shear stress present on curved free surfaces cannot be eliminated by mirroring each point with a corresponding point situated at the same distance from the free edge. Thus, the accumulated shear stress at the free surface caused by a circular arc load has to be associated with a corrective radial position that generates the same accumulated shear stress at the free surface, but in the opposite direction.

2.5.1 Shear stress generated at the free surface

In order to define the correction radius, the stresses caused inside and outside a ring load are calculated. The integration along the normal direction (z direction) is done analytically. On the other hand, the integration over the load arc (tangential direction θ) is done numerically. More details are provided later. Figure 2.3 shows the important parameters used in the stress calculation, where R is the radius at the free edge, r_i is the radius of the arc load, and r_o is the radius of the correction arc load required to eliminate the shear stress generated on the free surface of the protrusion.

Actually, while this description considers a cylindrical protrusion of radius *R,* the same procedure could also describe a cylindrical cavity of radius *R*. Therefore, the two next subsections look specifically at the internal load on a radius r_i and the external load on a radius r_o. The main coordinate system considered here is the cylindrical coordinate system (r, θ, z) illustrated in Figure 2.3.

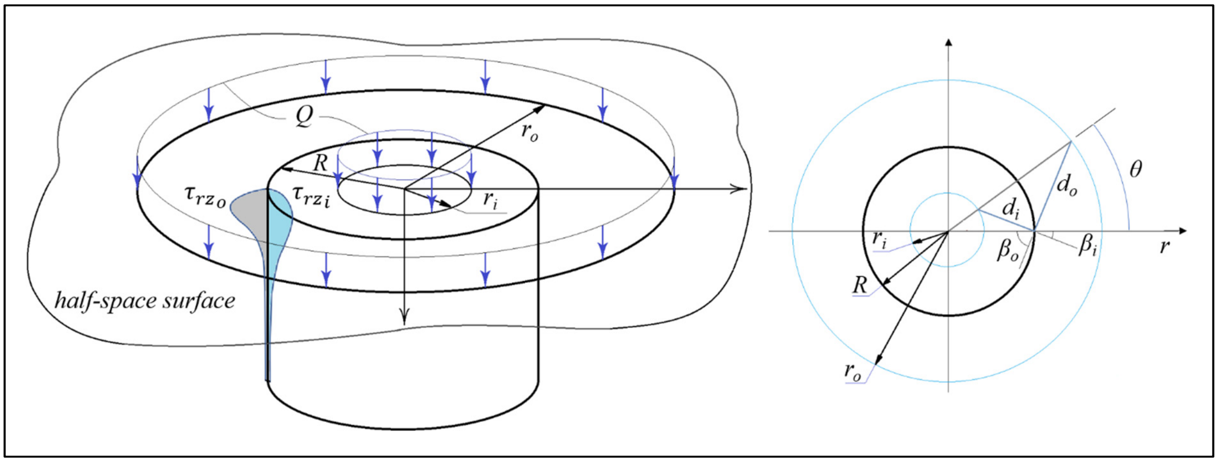

Figure 2.3 Parameters for a circular protrusion

The following variable definitions are introduced in the stress formulas,

$$c_{i,o}{}^2 = d_{i,o}{}^2 + z^2$$

while the next parameters are dimensionless:

$$n_i = \frac{r_i}{R}, n_o = \frac{R}{r_o}, \bar{z} = \frac{z}{R}, \bar{\tau}_{rz} = \frac{\pi R \tau_{rz}}{Q}$$

where τ_{rz} is the shear stress at $\theta = 0$ and Q is the constant force distributed over the arc. $d_{i,o}$, $\beta_{i,o}$, z are the variables defining the relative position of each infinitesimal load ($F = Q r_{i,o} d\theta$) on the inner (subscription i) or outer (subscription o) ring loads and the point (R, 0, z) where the stress is calculated. Eq. (2.6) gives the shear stress at the point (R, 0, z) generated by a point force F:

$$\tau_{rz}|_{\theta=0} = -\frac{3F}{2\pi}\frac{d_{i,o}\cos(\beta_{i,o})\, z^2}{{c_{i,o}}^5} \tag{2.6}$$

2.5.1.1 Shear stress distribution generated at a radius R by an arc load r_i

The dimensionless shear stress distribution generated on a cylindrical surface of radius *R* at $\theta = 0$ by an arc load of radius r_i situated on the top of a half-space (see Figure 2.3) is given by Eq. (2.7), where the φ is the limit angle of the load arc, which will be explained later, and $\bar{z}$ is the dimensionless *z/R* ratio. Figure 2.3 illustrates these conditions and the shear stress distribution.

$$\bar{\tau}_{rz_i} = -3\bar{z}^2 n_i \int_0^{\varphi} \frac{(1 - n_i\cos(\theta))}{(1 + {n_i}^2 - 2n_i\cos(\theta) + \bar{z}^2)^{2.5}}\, d\theta \tag{2.7}$$

Figure 2.4-a presents the shear stress distribution along *z* at *r* = *R* for five n_i ratios.

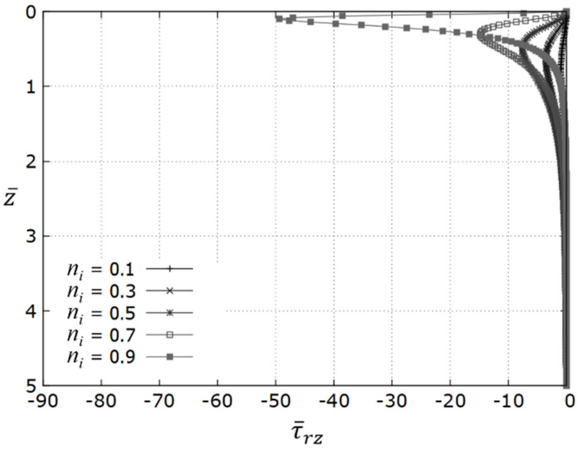

(a)

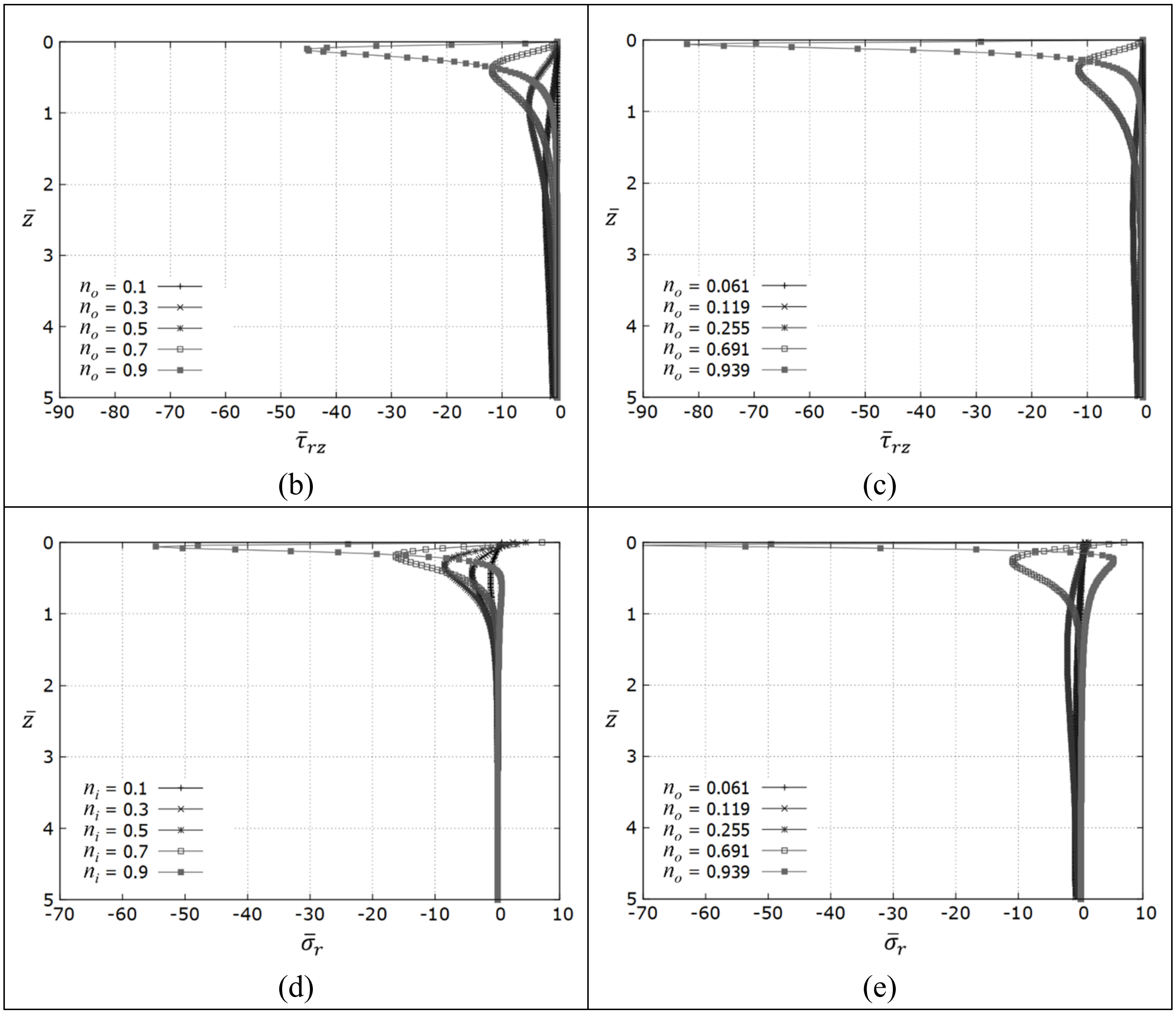

(b)

(c)

(d)

(e)

Figure 2.4 Dimensionless shear stress distribution at a radius R; caused by an arc load (a) over the ring of radius r_i (b) over the ring of radius r_o (c) over the ring of radius r_o positioned to generate a shear force equivalent to the stress accumulated along the z direction and dimensionless normal stress distribution at a radius R; caused by a ring load (d) over the ring of radius r_i (e) over the corresponding ring of radius r_o defined by Eq. (2.12)

The shear stress elimination procedure works with the force (B_z) equivalent to the accumulation of the shear stress along the z direction at radius R. Eq. (2.8) gives the equivalent force B_{z_i} generated by an arc load of radius r_i when $\theta = [-\varphi, \varphi]$. The angular integration in Eq. (2.8) over the arc load sums up the shear stress at the depth z caused by infinitesimal loads ($F = Qr_i d\theta$), while the linear integration along z gives the force equivalent to the accumulation of the shear stress.

$$
\begin{aligned}
B_{z_i} &= \int_{-\varphi}^{\varphi}\int_{0}^{\infty} \tau_{rz}\, dz\, d\theta \bigg|_{r_i} \\
&= -\frac{3n_iQ}{\pi R}\int_{0}^{\pi}\int_{0}^{\infty} \frac{(1-n_i\cos(\theta))\bar{z}^2}{\left((1+{n_i}^2-2n_i\cos(\theta))+(\bar{z})^2\right)^{\frac{5}{2}}}\, dz\, d\theta
\end{aligned}
\tag{2.8}
$$

2.5.1.2 Shear stress distribution generated at a radius R by an arc load r

The shear stress distribution generated on a cylindrical surface of radius *R* at $\theta = 0$ by an arc load of radius r_o situated on the top of a half-space is formulated by Eq. (2.9). Figure 2.3 illustrates these conditions as well as the shear stress distribution.

$$
\bar{\tau}_{rz_o} = -3\bar{z}^2{n_o}^3\int_{0}^{\varphi} \frac{(n_o-\cos(\theta))d\theta}{(1+{n_o}^2-2n_o\cos(\theta)+{n_o}^2\bar{z}^2)^{2.5}}
\tag{2.9}
$$

Figure 2.4-b,c illustrate the shear stress distribution generated at the position *r* = *R* for five n_o ratios. The n_o ratios considered in Figure 2.4-b correspond to n_i values of Figure 2.4-a, while those in Figure 2.4-c produce shear stress force equivalent to those generated by the n_i values in Figure 2.4-a, as will be explained later in Section 2.5.2 . Eq. (2.10) gives the equivalent force B_{z_o} generated by an arc load of radius r_o where $\theta = [-\varphi, \varphi]$.

$$
\begin{aligned}
B_{z_o} &= \int_{-\varphi}^{\varphi}\int_{0}^{\infty} \tau_{rz}\, dz\, d\theta \bigg|_{r_o} \\
&= \frac{3Q{n_o}^3}{\pi R}\int_{0}^{\pi}\int_{0}^{\infty} \frac{(n_o-\cos(\theta))\bar{z}^2}{\left((1+{n_o}^2-2n_o\cos(\theta))+(n_o\bar{z})^2\right)^{\frac{5}{2}}}\, dz\, d\theta
\end{aligned}
\tag{2.10}
$$

2.5.2 Shear stress elimination process

In order to eliminate the shear stress generated at *r=R* by an arc load of radius r_i, a neutralizing external load applied on an arc of radius r_o with the same angular limit ($\pm\varphi$) should produce an equivalent shear force ($B_{z_i} = B_{z_o}$). This neutralizing distributed load would play the same role as a mirror pressure for a straight boundary.

Displacing a point force over a circle of radius *r_o* generates shear stresses at the position (*R,0, z*), which alternate from negative to positive distributions. On the other hand, all the positions over a circle of radius r_i generate negative shear stress distributions. Therefore, the angular limit of the correction arc has to be established considering only the fraction of the circle of radius r_o that generates shear stresses of the same sign as the one generated by a point force situated on the circle of radius r_i. This condition determines the required φ. Figure 2.5 illustrates the considered region for a radius r_i and its corresponding radius r_o.

A rapid comparison of the curves displayed in Figure 2.4 indicates that while producing an equal shear force might be simple, generating a commensurate shear stress distribution should be difficult. Therefore, the procedure only assures a force equilibrium, equating Eqs. (2.8) and (2.10) as indicated by Eq. (2.11). After some manipulations, Eq. (2.11) proves to have no closed form solution. An approximate solution is thus obtained for $B_{z_i} = B_{z_o}$ using a numerical approach. The procedure considers the depth *z=10R* as infinity.

$$-\frac{n_i Q}{\pi R}\int_0^{\varphi}\left[\frac{(1-n_i\cos(\theta))}{(1+{n_i}^2-2n_i\cos(\theta))}\right]d\theta = \frac{Q}{\pi R}\int_0^{\varphi}\left[\frac{(n_o-\cos(\theta))}{(1+{n_o}^2-2n_o\cos(\theta))}\right]d\theta \qquad (2.11)$$

For a given ring load of radius r_i, Eq. (2.11) shows that the computation of the neutralizing load arc of radius r_o requires the definition of both r_i and φ. The arc limit φ also depends on r_o, which is not known at the beginning of the process. The arc limit for both inner and outer arc loads is considered the same. The calculation process is iterative; it results in calculation of both r_o and φ.

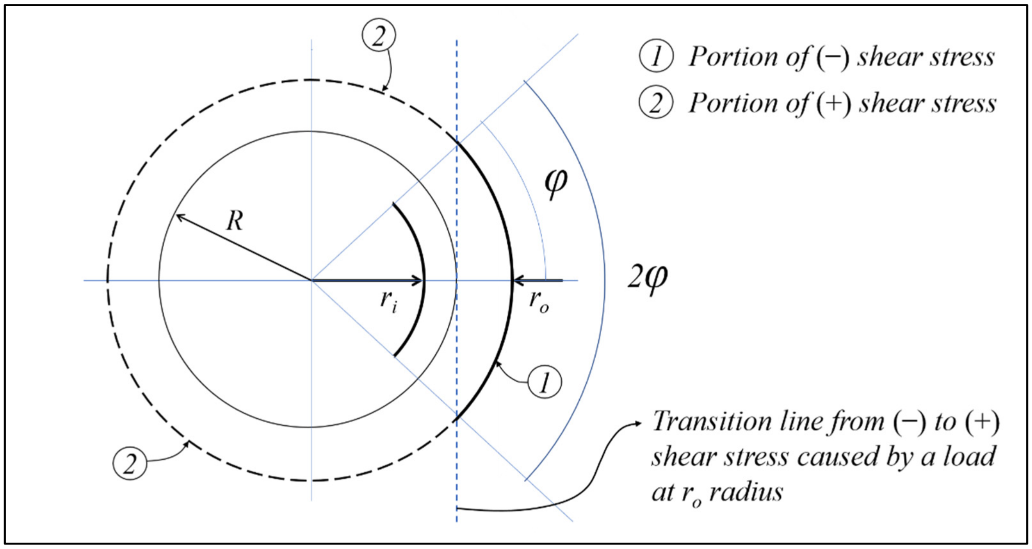

Figure 2.5 Arc limit for stress calculation

2.5.3 Numerical process and the results

Both n_i and n_o are by nature limited between *0* and *1*. As a result, both sides of the equality in Eq. (2.11) may be drawn in the same graph range. Figure 2.6 draws the left-hand side (*LH*) and the right-hand side (*RH*) of Eq. (2.11). Therefore, a very simple numerical solution for n_o may be obtained from a graphical approach, also illustrated in Figure 2.6. For a selected n_i position, the left-hand side (*LH*) of Eq. (2.11) is evaluated numerically, and then the *RH* is set to *LH*, and the solution process establishes the corresponding ratio of n_o. Eq. (2.12) provides a curve-fitting expression of this solution, and thus gives r_o as a fraction of r_i.

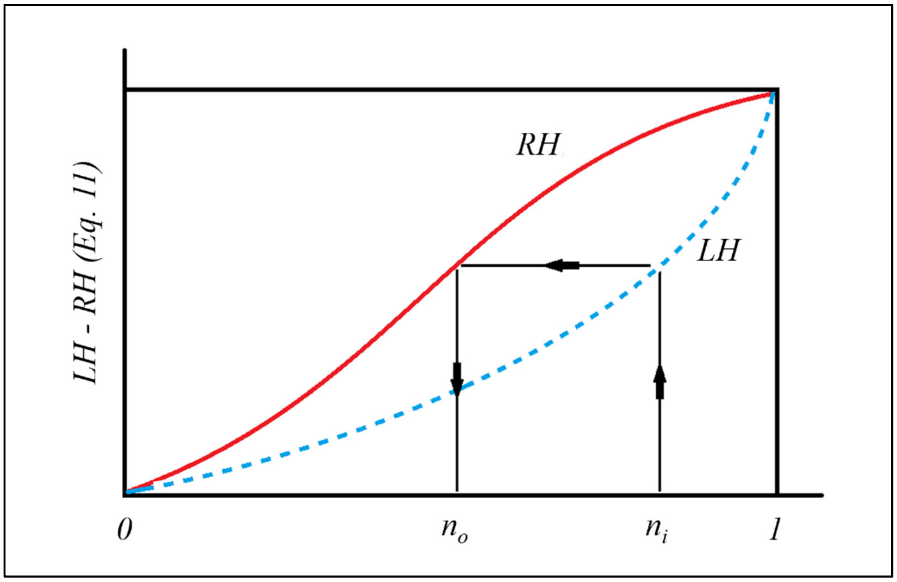

Figure 2.6 n1-n2 relation graph

$$n_o(n_i) = \frac{p_1 n_i^{\,4} + p_2 n_i^{\,3} + p_3 n_i^{\,2} + p_4 n_i + p_5}{n_o^{\,5} + q_1 n_o^{\,4} + q_2 n_o^{\,3} + q_3 n_o^{\,2} + q_4 n_o + q_5} \tag{2.12}$$

where

$p_1 = 0.2381$ $p_2 = -0.1652$ $p_3 = -0.00943$ $p_4 = 0.02335$ $p_5 = 9.47e-5$

$q_1 = -3.1$ $q_2 = 3.935$ $q_3 = -2.214$ $q_4 = 0.4578$ $q_5 = 0.008826$

Eq. (2.12) allows mapping any internal area onto its external correction area. Thus, Figure 2.7 illustrates the correction area obtained outside the contact region for a rectangular contact patch using Eq. (2.12). Eq. (2.12) gives a specific corresponding radius for any point inside the original patch. Transferring the perimeter of the original contact patch (m_1, m_2, m_3, m_4) results in a curvilinear quadrangle (curved edges). On the other hand, assuming that these edges are straight simplifies the calculation of the correction patch area. Hartnett's influence factor calculation formula assumes rectangular contact patches (Hartnett, 1980). Therefore, instead of the curvilinear quadrangle, the proposed calculation approach simplifies the correction patch to a rectangle with the same area as the mapped curvilinear quadrangle (Figure 2.7). The aspect ratio of the considered rectangle is the same as the original patch.

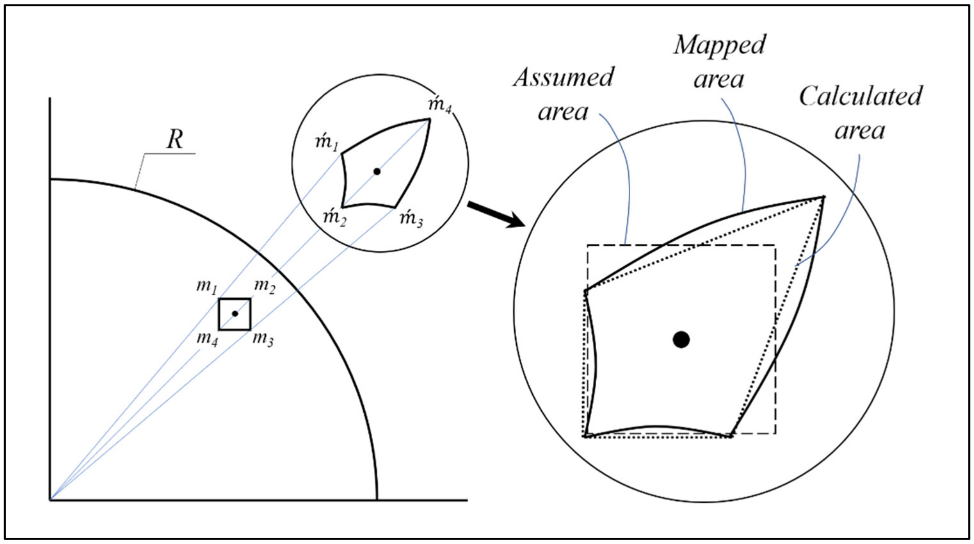

Figure 2.7 A schematic of the correction patch

In order to simplify the calculation, it is also possible to consider the correction patch area equal to the original patch area. However, while simplifying the process, it introduces some imprecision into the calculations. Therefore, the calculation approach for the correction patch area may be selected based on the needed precision. The results obtained from both approaches are compared later.

2.6 Normal stress elimination on a cylindrical free surface

To eliminate the normal stress distribution effect on the displacement of the contact surface, the present study develops an approach similar to the procedure put foreward by Guilbault in Ref. (Guilbault, 2011). This procedure overcorrects the effects of the shear stress distribution on the contact surfaces to compensate for the normal stress distribution consequences on the displacement. This strategy avoids increasing the computational cost and time. The process groundwork requires the description of the influence of the normal stress distributions engendered over a cylindrical surface of radius R by ring loads situated on the top of a half-space. Moreover, since a normal load applied over a cylindrical surface will in turn generate new shear and normal stress distributions onto the half-space surface, the definition of the influences of those stresses must also be established.

The forces equivalent to the accumulations of normal stresses presented in the following sections are also dependent on Poisson ratio, while the positions (l_r, r_z) of the lines of action of these forces remain almost independent of v. To simplify the calculations, the Poisson ratio is initially fixed at a constant value of 0.3, which represents an average evaluation compatible with most of the engineering materials. This simplification will be later compensated by a correction factor.

2.6.1 Normal stress generated inside a half-space at a radius *R* caused by a normal ring load

The normal stress distribution generated at a cylindrical surface of radius R by a ring load applied on an elastic half-space is calculated by integrating the Boussinesq formula over a complete ring. While an analytical integration along the z direction is relatively simple, the circular direction shows a singularity, which significantly complicates the integration process. Therefore, the solution combines the analytical integration along the z direction with a numerical integration along the cylindrical direction. Eq. (2.13) gives the normal stress at the position (R, 0, z) generated in a half-space by applying a point force $F = Qr_{i,o}d\theta$ on an inner (r_i) or an outer (r_o) rings over a half-space.

$$\begin{aligned}\sigma_r|_{(R,0,z)} = \frac{F}{2\pi}\Bigg[\frac{(1-2v)}{{d_{i,o}}^2}\Bigg\{\left(1-\frac{z}{c_{i,o}}\right)\left[\left(\cos(\beta_{i,o})\right)^2-\left(\sin(\beta_{i,o})\right)^2\right] \\ +\frac{z\left(d_{i,o}\sin(\beta_{i,o})\right)^2}{{c_{i,o}}^3}\Bigg\}-\frac{3z\left(d_{i,o}\cos(\beta_{i,o})\right)^2}{{c_{i,o}}^5}\Bigg]\end{aligned} \qquad (\ 2.13\ )$$

$$\bar{\sigma}_r = \frac{\pi R\sigma_r}{Q}$$

where σ_r is the normal stress in radial direction.

2.6.1.1 Normal stress distribution generated at a radius R by a ring load of radius r$_i$

The dimensionless normal stress distribution generated at a cylindrical surface of radius *R* by a ring load (radius *r$_i$*) situated on top of an elastic half-space (see Figure 2.3) is given by Eq. (2.14):

$$\bar{\sigma}_{r_i} = n_i \int_0^{\pi} \left[\frac{(1-2v)}{(t_i)} \left\{ \left(1 - \frac{\bar{z}}{(t_i + \bar{z}^2)^{\frac{1}{2}}} \right) \frac{(s_i + {n_i}^2 \cos(2\theta))}{(t_i)} + \frac{\bar{z}{n_i}^2 \sin(\theta)^2}{\left((t_i + \bar{z}^2)\right)^{\frac{3}{2}}} \right\} - \frac{3\bar{z}(s_i + {n_i}^2 \cos(\theta)^2)}{\left((t_i + \bar{z}^2)\right)^{\frac{5}{2}}} \right] d\theta \qquad (2.14)$$

where the parameters *s$_i$* and *t$_i$* are defined as follows:

$$s_i = 1 - 2n_i \cos(\theta)$$

$$t_i = a_i + {n_i}^2$$

Figure 2.4 also presents the dimensionless normal stress distributions along $\bar{z}$ at *r* = *R*. Figure 2.4-d illustrates the dimensionless normal stress distribution for the ring loads applied on five *n$_i$* ratios, while Figure 2.4-e illustrates the dimensionless normal stress distribution for the ring loads applied on five *n$_o$* ratios calculated with Eq. (2.12) for the *r$_i$* radiuses used in Figure 2.4-e (Eq. (2.12)).

The normal stress elimination procedure also works with the force equivalent to the accumulation of the normal stress generated along *z* direction. Eq. (2.15) gives the equivalent force (C_{r_i}) acting at $\theta = 0$ and radius *R* for a ring load of radius *r$_i$*. As before, the angular integration is done over the ring load to sum up the normal stresses at (*R, 0, z*), while the linear integration along *z* finally produces the force equivalent to the normal stresses.

$$C_{r_i} = \int_{-\pi}^{\pi} \int_{0}^{\infty} \sigma_r \, dz \, d\theta \bigg|_{r_i} = -\frac{2Qvn_i}{\pi} \int_0^{\pi} \frac{(1 + {n_i}^2 \cos(\theta)^2 - 2n_i \cos(\theta))}{(1 + {n_i}^2 - 2n_i \cos(\theta))^{\frac{3}{2}}} d\theta \qquad (2.15)$$

2.6.1.2 Normal stress distribution generated at a radius R by a ring load of radius r$_o$

Eq. (2.16) formulates the normal stress distribution at the position (*R, 0*) generated by a ring load of radius r_o situated on top of an elastic half-space, where the parameters s_o and t_o are defined as follows.

$$s_o = {n_o}^2 - 2n_o \cos(\theta)$$

$$t_o = a_o + 1$$

$$\begin{aligned} \bar{\sigma}_{r_o} = n_o \int_0^{\pi} \Bigg[& \frac{(1-2v)}{(t_o)} \Bigg\{ \Bigg(1 - \frac{n_o \bar{z}}{(t_o + {n_o}^2 \bar{z}^2)^{\frac{1}{2}}} \Bigg) \frac{(s_o + \cos(2\theta))}{(t_o)} \\ & + \frac{n_o \bar{z} \sin(\theta)^2}{(t_o + {n_o}^2 \bar{z}^2)^{\frac{3}{2}}} \Bigg\} - \frac{3 n_o \bar{z} (s_o + \cos(\theta)^2)}{(t_o + {n_o}^2 \bar{z}^2)^{\frac{5}{2}}} \Bigg] d\theta \end{aligned} \qquad (2.16)$$

As mentioned before, Figure 2.4-e illustrates the normal stress distribution along the $\bar{z}$ direction and at *r* = *R* for five n_o ratios. Eq. (2.17) gives the normal force (C_{r_o}) at $\theta = 0$ and radius *R* equivalent to the normal stresses distributed along the *z* direction for an applied ring load of radius r_o.

$$C_{r_o} = \int_{-\pi}^{\pi} \int_{0}^{\infty} \sigma_r \, dz \, d\theta \bigg|_{r_o} = -\frac{2Qv}{\pi} \int_0^{\pi} \frac{({n_o}^2 + \cos(\theta)^2 - 2n_o \cos(\theta))}{(1 + {n_o}^2 - 2n_o \cos(\theta))^{\frac{3}{2}}} d\theta \qquad (2.17)$$

Eq. (2.18) provides the position of the line of action (l_r) for the equivalent forces given by Eqs. (2.15) and (2.17). Figure 2.10 demonstrates how these positions are perceived.

$$l_r = \frac{\int_0^\infty z\,\sigma_r\,dz}{\int_0^\infty \sigma_r\,dz} \tag{2.18}$$

2.6.2 Normal displacement over a half-space caused by a normal ring load

Eq. (2.19) shows the formula proposed by Lubarda (Lubarda, 2013) for calculating the surface displacement (w_{ha}) at a radius r caused by a ring load of radius r_o over a half-space, where $r<r_o$.

$$w_{ha} = \frac{2Q(1-v)}{\pi G} K\left(\frac{r}{r_o}\right) \tag{2.19}$$

with G is the shear modulus and K is the elliptical integral of the first kind.

2.6.3 Normal stress generated inside a cylinder caused by a radial ring load

In the proposed strategy, the stress distributions are replaced by the equivalent forces (C_{r_i}, C_{r_o}) established above. These resultants are actually not concentrated forces, but rather, are distributed around the cylindrical surface of radius R at a l_r position along z. The elimination process of the calculated normal force requires the addition of an antagonistic distributed force at the same axial position.

Any force distribution applied around the cylindrical surface will in turn generate normal stresses and displacements in the z direction. The equations establishing the response of the solid to this load are thus also required. The process uses the stress distribution derived from the potential function (Eq. (2.20)) given by Timoshenko (Timoshenko S. P., s.d.) for the conditions illustrated in Figure 2.8-a. Developing the normal stress distribution for the conditions brought in Figure 2.8-a, it is possible to superpose two slightly shifted distributions (Figure 2.8-b) to produce a pressure band acting around a cylinder (Figure 2.8-c and d).

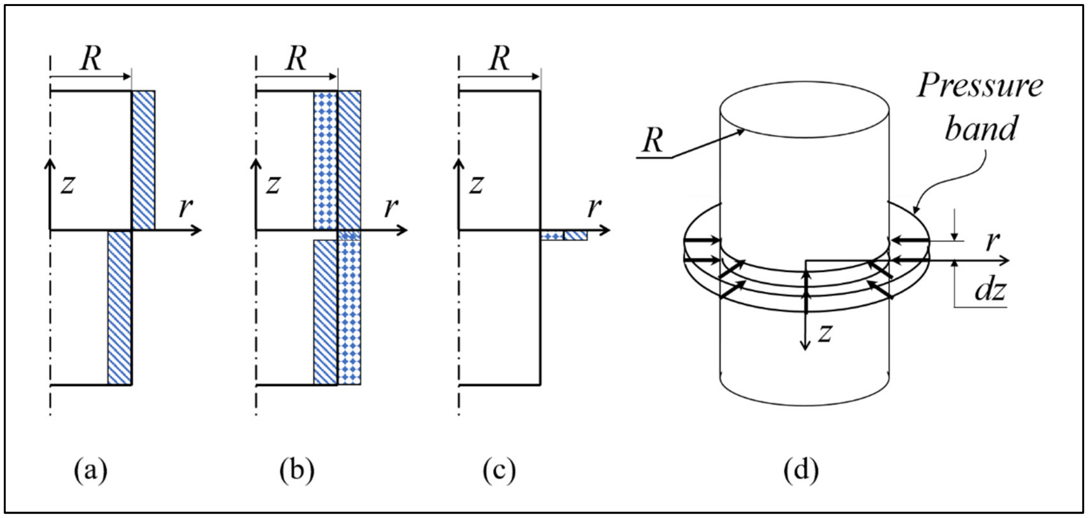

Figure 2.8 (a) Pressure distribution for the initial potential function, (b) Superposition model, (c, d) Pressure band

Eq. (2.21) expresses the normal stress along the *z* direction, where ϕ is the potential function given by Eq. (2.20) for the condition illustrated in Figure 2.8-a. Eq. (2.22) gives the resulting normal stress (σ_{z_f}) generated at the depth *z* for this load condition. Introducing Eq. (2.22) into Eq. (2.23) gives the axial normal stress (σ_z) generated at the depth *z* by a pressure band around a cylinder (Figure 2.8-c,d). The procedure considers the width of the pressure band small enough to simulate a line load. To evaluate the width of the band required to reproduce a line load, a comparison was made with the results obtained from FEA. This comparison showed that *dz=0.001R* gives acceptable results (Figure 2.9). Figure 2.9 shows, for two dimensionless radial positions (*r/R= 0.25*, *0.75)*, that the stress distribution obtained from the potential function with *Q=P dz* are in perfect agreement with the results obtained from FEA along *z* direction for a distributed force *Q* around a cylinder of radius *R*. The force *Q* acts at *z=0*.

$$\phi = -\frac{Q}{\pi\, dz}\int_0^\infty \frac{[\rho\, I_0(kr) - kr\, I_1(kr)]\cos(kz)}{k^4\left[(1-2\upsilon-\rho)I_0(kR) + \left(kR + \frac{\rho}{kR}\right)I_1(kR)\right]}dk \tag{2.20}$$

$$\sigma_{z_f} = \frac{\partial}{\partial z}\left[(2-\upsilon)\left[\frac{\partial^2\phi}{\partial r^2} + \frac{1}{r}\frac{\partial\phi}{\partial r}\right] + (1-\upsilon)\frac{\partial^2\phi}{\partial z^2}\right] \tag{2.21}$$

$$\sigma_{z_f} = -\frac{Q}{\pi\, dz}\times$$

$$\int_0^\infty \frac{sin(kz)\big(2Rk^3I_1(kR)I_0(kr) - R^2k^4I_0(kR)I_0(kr) + Rk^4rI_1(kR)I_1(kr)\big)}{k^3\left[\big(I_1(kR)\big)^2(R^2k^2-2v+2) - R^2k^2\big(I_0(kR)\big)^2\right]}dk \tag{2.22}$$

$$\sigma_z = \left(\sigma_{z_f} - \sigma_{z+dz_f}\right) \tag{2.23}$$

while I_0 and I_1 are modified Bessel functions of the first kind and the parameter ρ is defined as follows:

$$\rho = 2(1-\nu) + kR\frac{I_0(kR)}{I_1(kR)}$$

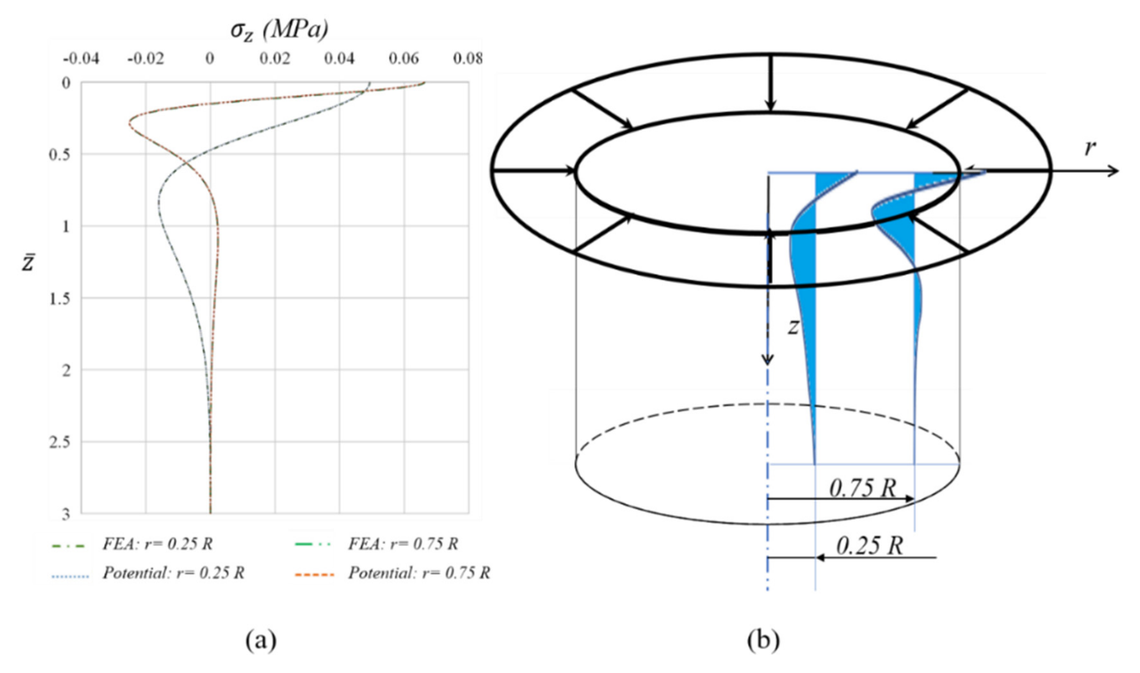

(a) (b)

Figure 2.9 Potential function validation.

Eq. (2.24) gives the normal force (C_z) equivalent to normal stresses σ_z generated at both z and $-z$ positions over the range 0 to R by an applied radial ring load around a cylinder of radius R (shown in Figure 2.9).

$$C_z = \int_0^R \sigma_z dr \bigg|_z = \int_0^R \sigma_z dr \bigg|_{-z} \tag{2.24}$$

Eqs. (2.25) and (2.26) respectively give the position of the line of action of the equivalent axial force (C_z) in relation to the edge (r'_z) and its radial position r_z (see Figure 2.10).

$$r'_z = \frac{\int_0^R (R-r)\,\sigma_z\,dr}{\int_0^R \sigma_z\,dr} \tag{2.25}$$

$$r_z = R - r'_z = \frac{\int_0^R r\,\sigma_z\,dr}{\int_0^R \sigma_z\,dr} \tag{2.26}$$

2.6.4 Axial displacement caused by a radial ring load around a cylinder

Eq. (2.27) gives the axial displacement in the *z* direction caused by the conditions illustrated in Figure 2.8-a. Introducing the potential function (Eq. (2.20)) into Eq.(2.27) results in Eq. (2.28), which gives the axial displacement w_z at a position (*r, z*). Introducing the displacement obtained from Eq. (2.28) for the conditions of Figure 2.8-a into Eq. (2.29) gives the axial displacement w_{cy} caused by a pressure band acting around a cylinder (Figure 2.8-c,d). The width of the pressure band is *dz=0.001R* as before.

$$w_z = \frac{1}{2G}\left[2(1-v)\nabla^2\phi - \frac{\partial^2\phi}{\partial z^2}\right] \tag{2.27}$$

$$w_z = \frac{Q}{2\pi G\,dz} \int_0^\infty \frac{cos(kz)R\big(RkI_0(kR)I_0(kr) - krI_1(kR)I_1(kr) + 2I_1(kR)I_0(kr)(v-1)\big)}{k\left[\big(I_1(kR)\big)^2(R^2k^2-2v+2) - R^2k^2\big(I_0(kR)\big)^2\right]}\,dk \tag{2.28}$$

$$w_{cy} = (w_z - w_{z+dz}) \tag{2.29}$$

2.6.5 Normal stress elimination process

The following description is illustrated in Figure 2.10. The elimination of the normal stress generated by a ring load acting over a half-space at a radius r_i and its corresponding shear correction ring load acting at the radius r_o requires a counterbalancing equivalent normal stress.

The proposed procedure replaces the generated normal stresses (σ_r) by their equivalent forces $C_{r_{i,o}}$ (Eqs. (2.15) and (2.17)), which are actually radial loads occurring around a cylinder at the axial position given by their line of action l_r (Eq. (2.18)). Eliminating these radial forces requires an equivalent antagonistic load (C_r) at the same position. This correction force in turn causes shear and normal stresses on the half-space surface of radius *R*. To eliminate this new shear stress, the process applies the same load at a symmetrical position. These two correction forces cause new normal stresses (σ_z) on the half-space surface. The next step of the procedure replaces these σ_z normal stresses by the equivalent force C_z (Eq. (2.24)), which is actually a ring load acting over the half-space at a radius r_{z_i} (Eq. (2.26)). As before, eliminating this equivalent force requires an equivalent antagonistic load (C_z) at the same position, which again requires a counterbalance load at a corresponding radius r_{z_o} for eliminating the new shear stresses on the cylindrical free surface caused by C_z. Again, the loads at r_{z_i} and r_{z_o} generate new normal stresses on the free surface of the body. As before, the procedure replaces these normal stresses by their equivalent forces at the positions of their lines of action. Theoretically, this cyclic procedure is infinite. However, the effects of the equivalent forces are reduced after some cycles.

Ultimately, the displacement of the half-space at r_i caused by the initial shear eliminating load at r_o (w_Q) and the correction forces C_r (w_{cy}) and C_z (w_{ha}) (Figure 2.10) accumulate and produce a total displacement w_{Q^*} (Eq. (2.30)). Since the correction forces fade as the process evolves, w_{Q^*} converges to a fixed value for each initial r_i radius.

$$w_{Q^*} = w_Q + \sum \left(w_{ha} + w_{cy}\right) \tag{2.30}$$

Similar to the approach of Ref. (Guilbault, 2011), this study assumes a Q^* distributed load at r_o that causes a surface displacement w_{Q^*}. Therefore, Q^* becomes equal to $Q(w_{Q^*}/w_Q)$. This Q* eliminates the influence of both shear and normal stress distributions produced by a ring load *Q* of radius r_i. If Q^* is written as $Q^*=nsf\,Q$, Eq. (2.31) gives *nsf*, while Eqs. (2.32) and (2.33) give the *nsf* factor final formulation established from the combination of the previous equations. The obtained *nsf* is valid for any dimensionless radius between *0* and *1*.

$$nsf = \frac{Q^*}{Q} = \frac{w_{Q^*}}{w_Q} \tag{2.31}$$

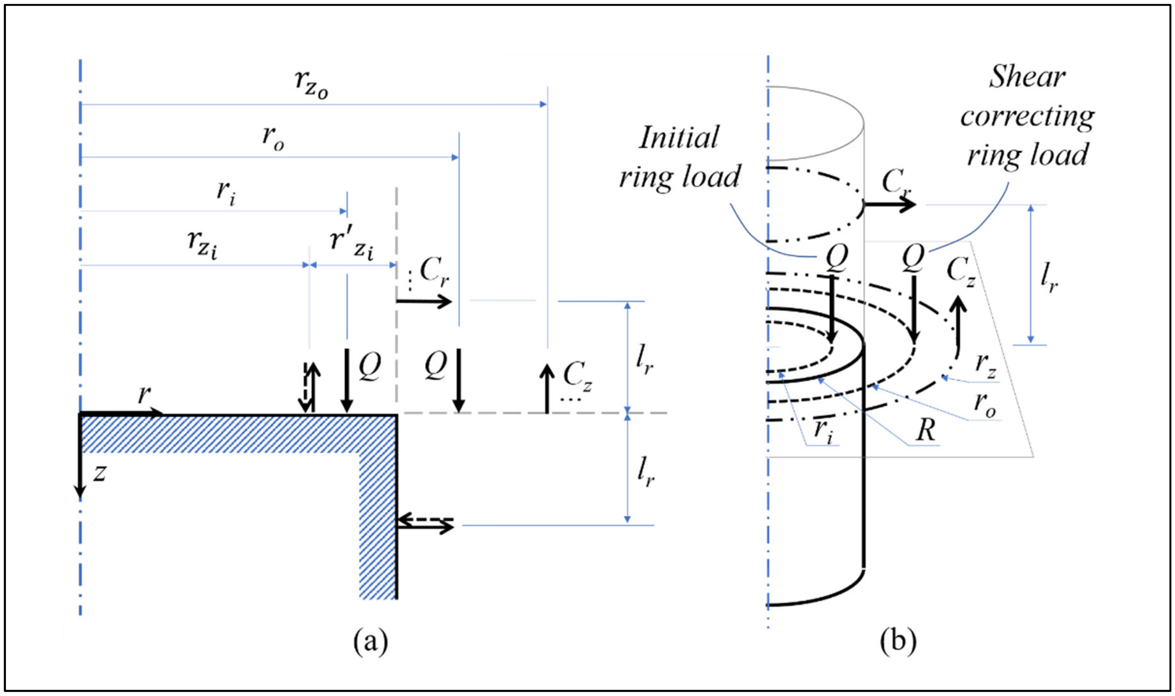

Figure 2.10 Initial steps of residual normal stress elimination process

$$nsf = \frac{p_1 {n_i}^4 + p_2 {n_i}^3 + p_3 {n_i}^2 + p_4 n_i + p_5}{{n_i}^3 + q_1 {n_i}^2 + q_2 n_i + q_3} \qquad (0 < n_i \leq 0.67) \tag{2.32}$$

$p_1 = -0.03995$ $p_2 = 1.227$ $p_3 = 1.252$ $p_4 = 0.05578$ $p_5 = 7.16e-5$

$q_1 = 1.284$ $q_2 = 0.0615$ $q_3 = 0.000111$

$$nsf = \frac{p_1 n_i^5 + p_2 n_i^4 + p_3 n_i^3 + p_4 n_i^2 + p_5 n_i + p_6}{n_i^5 + q_1 n_i^4 + q_2 n_i^3 + q_3 n_i^2 + q_4 n_i + q_5} \qquad (0.67 < n_i < 1) \qquad (2.33)$$

$p_1 = -1.797$ $p_2 = 0.7247$ $p_3 = 0.7923$ $p_4 = 0.2787$ $p_5 = 0.1678$

$p_6 = 2.717$ $q_1 = -1.628$ $q_2 = -0.7441$ $q_3 = 0.06873$ $q_4 = l2.203$

$q_5 = 1.871$

As mentioned earlier, the actual results obtained in the previous section depend on Poisson ratio. Therefore, since previous developments assumed a constant value, Eqs. (2.32) and (2.33) are expressions valid for *v=0.3*. Nevertheless, *nsf* may be corrected to account for any *v* value. Figure 2.11 shows the nsf_v factor for various Poisson ratios. These curves may be amalgamated to form an nsf_v evaluation valid for any *v*. Eq. (2.34) gives nsf_v as a function of *nsf* given by Eqs. (2.32) and (2.33).

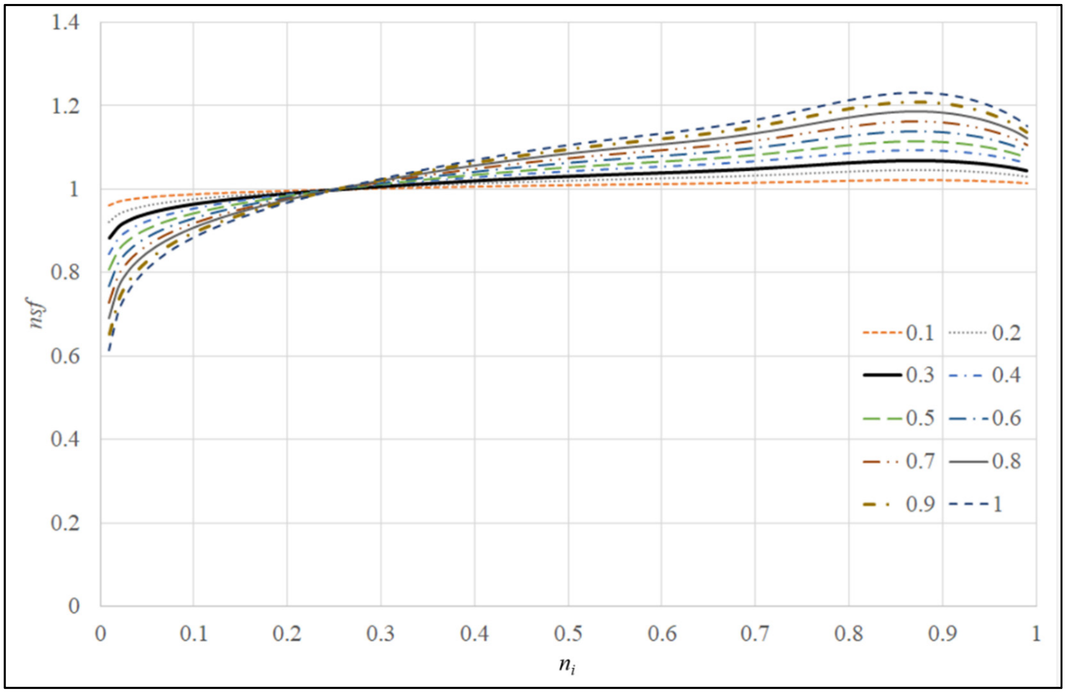

Figure 2.11 Normal stress correction factor for different Poisson ratios

The results obtained from Eq. (2.34) are less precise for the last 30% of the dimensionless radius (*r/R*), specially for Poisson ratios that are not close to 0.3. In cases requiring higher precision, the graphs in Figure 2.11 provide more precise *nsf* values.

$$nsf_v = 1 + \frac{10v}{3}(nsf - 1) \qquad (2.34)$$

2.7 Summarized implementation process

The elimination process of the free boundary stress follows the following steps:

1) Eq. (2.12) maps the contact patch onto a correction patch and gives the position of the counterbalance pressure;

2) Calculate the area of the correction patch and replace it with a square patch of the same area (see Figure 2.7);

3) Apply the pressure (same as the contact patch) onto the correction patch and calculate the correction force *Q* required to eliminate the shear stress distribution (partial correction);

4) Calculate *nfs* the correction factor with Eqs. (2.32) and (2.33), and multiply *Q* by *nfs* to obtain Q^*. Q^* eliminates both the shear stress and the normal stress distributions (complete correction).

2.8 Model validation

The simple problem illustrated in Figure 2.12 serves as a validation arrangement for the developed model. This sample problem assumes two long coaxial cylinders with the same radius *R* pressed against each other. The considered Poisson ratio is 0.3. The contact pressure distribution obtained from the proposed model is compared with the results obtained from FEA.

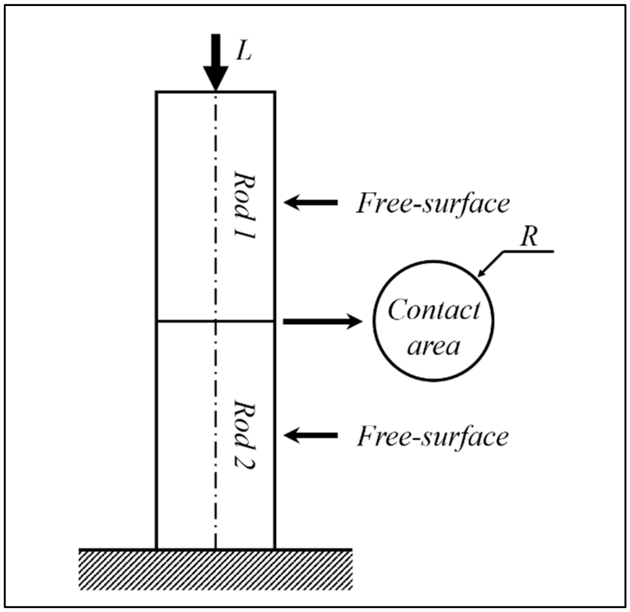

Figure 2.12 Rod problem

For a complete illustration of the *nsf* role, Figure 2.13-a compares the contact pressure evaluated over the contact area by Hartnett's procedure without any correction, with partial correction (shear) and with a complete stress correction (shear and normal) produced by *nsf* with the FEA results obtained for the Figure 2.12 conditions. Those results are presented on a dimensionless graph; the horizontal axis is $\bar{r} = r/R$, while the vertical axis is $\bar{P} = P/P_{ave}$. The graph also includes the results obtained with a partial correction when the correction patches have the same size as the contact patch.

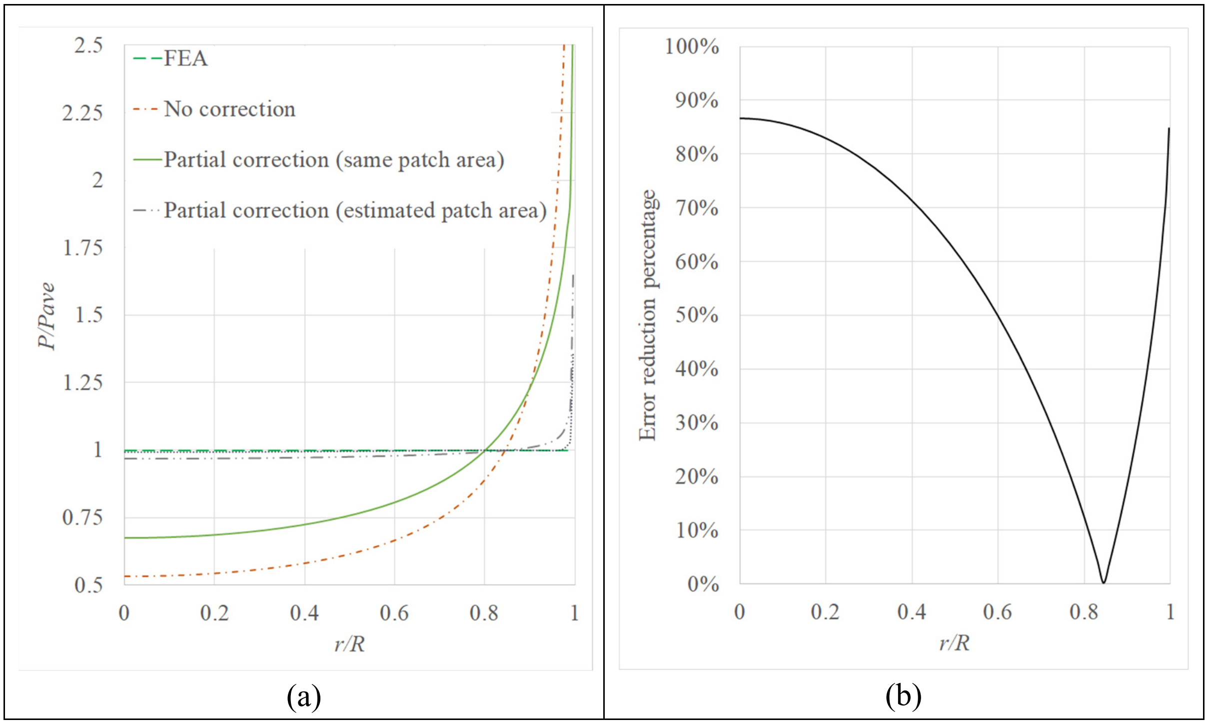

(a) (b)

Figure 2.13 (a) Dimensionless contact pressures obtained for R=10 mm, L=50N; (b) Contact pressure correction percentage compared to no-correction

Figure 2.13-a shows that when maintaining the correction patch size equal to the size of the contact patches, the partial correction does not really improve the results. On the other hand, by adapting the correction patch size, the sole shear stress correction significantly improves the results as compared to the no-correction condition and brings the results close to the reference FEA evaluations. Nevertheless, the precision decreases in the immediate vicinity of the free edge, where $\bar{r}$ approaches *1*; the remaining effects of the normal stress (after a shear correction) mainly affects the predictions close to the free boundary. Adding the normal stress correction with *nsf* further enhances the precision of the results close to the boundary, but has no practical effect at positions where $\bar{r} < 0.9$. However, it is also worth mentioning that the inclusion of *nsf* into the calculation procedure does not change the computation times compared to the sole shear correction. Moreover, these computation times remain small in comparison to those required for FEA. For example, for the precision shown in Figure 2.13-a, the calculation times were respectively 15 s, 25 s, 27 s and 464 s for the no-correction, sole shear correction (estimated patch area), complete correction and FEA. These calculations were

made on a computer with a Quad core 3.4GHz CPU. Finally, Figure 2.13-b shows the correction percentage of the complete correction in comparison with the no-correction results; despite the pressure peak at the edge, the correction percentage remains about 85%. The small remaining difference in comparison with FEA results may be attributed to the Hartnett procedure being based on rectangular pressure patches, which actually only approximate the real curved shape of the boundary.

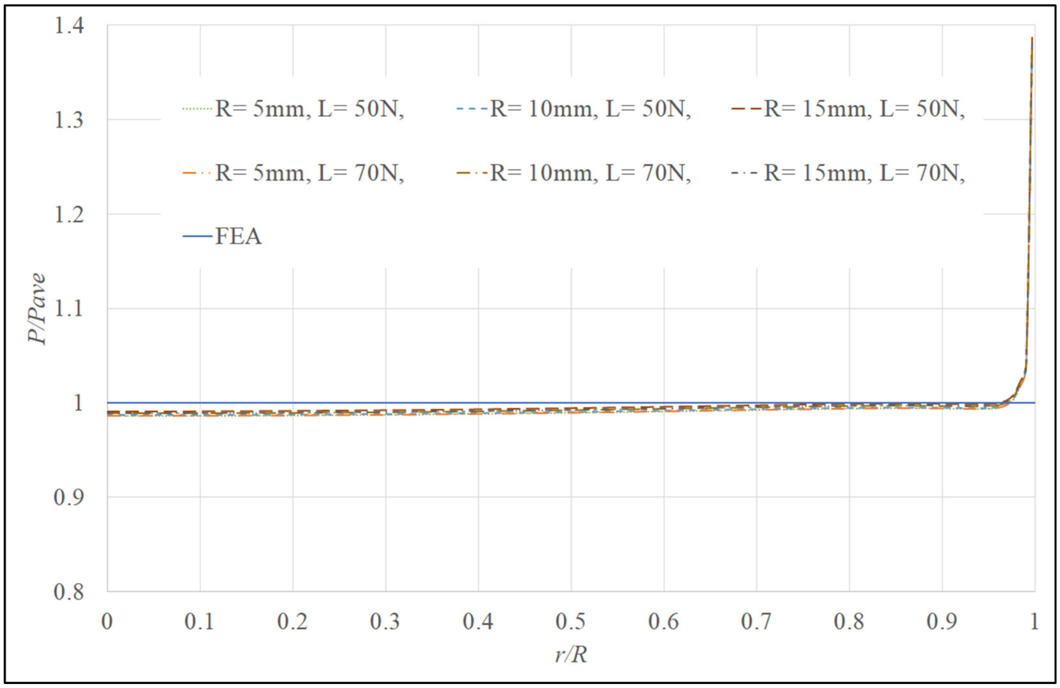

Figure 2.14 Dimensionless contact pressures obtained for obtained for different R and L values

To complete the validation, the prediction of the proposed method are compared to the FEA evaluation for three values of *R* (5 mm, 10 mm and 15 mm) and two force amplitudes *L* (50 N, 70 N). Figure 2.14 presents the pressure graph using the dimensionless variables (pressure and radius) defined above. The calculations were made with constant numbers of elements, which is equivalent to constant dimensionless mesh sizes. The results were established using the complete correction. The graph shows that the proposed approach provides a constant precision for a given dimensionless mesh size.

The global precision also depends on the dimensionless size of the contact patches. Therefore, in order to clarify the effects of the patch size, the following analysis compares three different contact mesh refinements for a fixed condition (*L= 50 N, R= 10 mm*). The contact meshes are made of rectangular patches with smaller sizes close to the free boundary. Figure 2.15 shows the shape of a typical contact mesh. As indicated earlier, Eq. (2.12) maps each rectangular patch from inside the boundary to a nonrectangular correction patch outside the boundary (Figure 2.7).

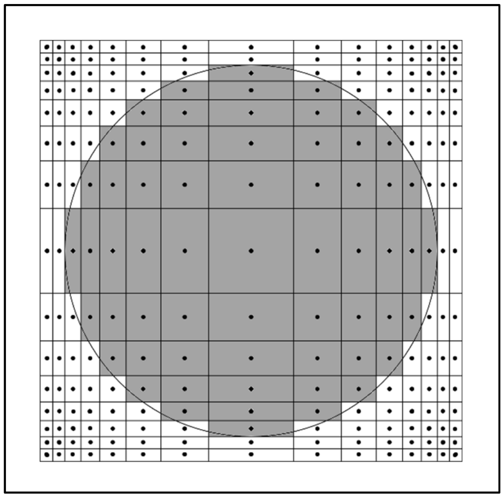

Figure 2.15 Typical contact mesh with rectangular patches

Table 2.1 juxtaposes the calculated differences between the model predictions and the FEA for three mesh sizes. The calculations are made at four dimensionless radial positions. These results demonstrate the precision of the proposed method and indicate that the remaining differences are attributable to the decrease of the rectangular contact patches with a reduction of the patch size. Finally, while being as precise as FEA, as already mentioned, the proposed modeling procedure is less time-demanding. For example, the calculation times for the evaluations of Table 2.1 were 14 s, 200 sec, 135 s and 2885 s for the 51 patch model, 151 patch model, the 51 nodes FEA and the 151 FEA respectively; the model is more than 9 times faster than the FEA with the 51 patch mesh and more than 14 times with the 151 patch one.

Table 2.1 The percentage of pressure difference in comparison with FEA results for various mesh refinement

Position (*r/R*)	Number of patches along *R*		
	51	151	451
0.00	*1.80%*	*0.66%*	*0.63%*
0.33	*1.59%*	*0.58%*	*0.55%*
0.66	*1.00%*	*0.41%*	*0.38%*
0.99	*-12.34%*	*-0.92%*	*0.05%*

2.9 Conclusion

The first part of this paper develops a simple approach for the elimination of the shear stresses generated on curved free surfaces caused by the half-space assumption present in semi-analytical methods applied to contact simulation. A common simple approach for the elimination of the shear stresses generated on a planar free surface should consider a counterbalance pressure patch located at the same distance from the free edge, but on the mirror side. Since this approach is not optimal for curved edges, this study introduces a counterbalance radius based on the free edge radius to map the shear correction patch. A graph showed the relation between each dimensionless radius inside the free edge and its corresponding dimensionless radius outside the boundary. This relationship between inside radii and their corresponding parts is also formulated in an equation that allows a complete mapping of a rectangular pressure patch. A comparison with FEA results shows that applying the proposed shear correction approach reduces the errors intrinsic to the half-space assumption by up to 92%. The evaluations show that the effectiveness of the proposed approach is not a function of the free edge radius or the applied load.

The second part of this paper proposes a correction factor to eliminate the influence of the intrinsic normal stress generated by the halfspace assumption on the surface displacement. This correction factor modifies the amplitude of the pressure applied on the shear correction patch defined in the first part. The complete calculation procedure thus reduces to two simple equations: the first one establishes the correction patch size and position required to eliminate the shear stress on the free edge, while the second one defines the correction adjustment required to compensate for the normal stress influences. A final comparison with FEA results shows that applying the complete correction (shear and normal stresses) further reduces the errors by up to 96%. As before, the effectiveness of the presented factor is independent of the dimensions and the load.

Finally, in addition to its simplicity and effectiveness compared to FEA, the proposed approach is less time-consuming, ignoring the preparation time required by FEA. The proposed approach shows, for the studied cases and equivalent precision, calculation times at least 9 times lower than those of the FEA.

CHAPTER 3

A FAST THERMOELASTIC MODEL BASED ON THE HALF-SPACE THEORY APPLIED TO ELASTOHYDRODYNAMIC LUBRICATION OF LINE CONTACTS INVOLVING FREE BOUNDARIES

Ali Yalpanian[a], Raynald Guilbault[b],

[a,b] Department of Mechanical Engineering, École de technologie supérieure, Université du Québec, 1100 Notre-Dame West, Montreal, Quebec, Canada H3C 1K3

Paper submitted for publication, May 2021

3.1 Abstract

This study allows contact models based on semi-analytical methods including the impacts of thermoelastic deformations in contacts of finite dimension bodies. The proposed method controls heat flows crossing free boundaries. A comparison with FEA reveals that the proposed method can reduce the calculation times by more than 98%. The paper introduces the thermoelasticity effects into thermal-elastohydrodynamic lubrication (TEHL) modeling of line contact problems. The analysis reveals that including thermoelastic deformations changes the pressure profile, and tends to localize the pressure close to the distribution center. Compared to TEHL simulations, the examined configurations caused an overall increase in the maximum pressure by about 9%, an overall film thickness reduction of about 7%, and an overall temperature increase of about 2 K.

Keywords: Contact Mechanic, Thermoelastic Deformations, Semi-Analytical Method, Elastohydrodynamic Lubrication

3.2 Introduction and literature survey

This study presents a simple method for incorporating the effects of thermoelasticity in the modeling of contacts with free edges based on steady-state half-space theory. This class of problem includes contact conditions ranging from dry to Thermal Elastohydrodynamic Lubrication (TEHL) contacts. The proposed method addresses problems commonly encountered in different industrial applications, such as line contacts in roller bearings and gears (M. Liu et al., 2019 ; Z. Liu et al., 2019 ; Meng, Yu, Xie, & Mei, 2018 ; K. L. Wang & Cheng, 1980) or in static electrical contacts in power transfer equipment (Albers, Martin, & Lorentz, 2011 ; Chin-Tu & Bryant, 1994 ; Williamson & Majumdar, 1992). In many of these devices, the real loads and pressure distributions may potentially be affected by thermoelastic displacements. Actually, the true level of influence of thermoelasticity is not really known, since precise experimental measurements are virtually impossible, while the great majority of the available modeling strategies simply neglect it.

In reality, when considering simple contact configurations and ignoring thermal considerations, Hertz theory (Hertz, 1896) provides precise evaluations of contact areas and pressure distributions. In essence, this theory imposes the following restrictions: a) The combined surfaces induce no friction; b) The contact zone covers a limited portion of the surfaces; and c) The width of the contact zone is small in proportion to the surface radii. While the essence of restriction a) is clear, b) and c) enforce less obvious limitations, with b) eliminating the consequential effect of surrounding borders, and c) leading to the solids being considered as half-spaces solely accepting elastic displacements.

Researchers have also proposed methods close to the Hertz theory, but better adapted to irregular surfaces (de Mul et al., 1986 ; Hartnett, 1980 ; S. Liu & Hua, 2009). For instance Ref. (Hartnett, 1980) by Hartnett introduces a Semi-Analytical Method (SAM) based on the half-space theory (Johnson K.L., 1985), which is a very effective one of them. Rough surfaces have also been solved using similar semi-analytical methods (Chen & Wang, 2009 ; Poon & Sayles, 1994 ; Tian & Bhushan, 1996 ; Willner, 2008). The presence of free surfaces for cases such as roller bearings introduces some errors to such methods due to the stresses (normal and shear) forced on those surfaces by the half-space concept. Few authors ((Hanson & Keer, 1995 ; Hetényi, 1960, 1970 ; Keer et al., 1983)) implemented effective tactics for eliminating these stresses, and while the solutions were precise, they were nonetheless rather tedious. To the same end, Guilbault and Yalpanian (Guilbault, 2011 ; Yalpanian & Guilbault, 2020) proposed simpler solutions based on correction factors. This correction factor approach provides high precision levels for contacts involving free surfaces without imposing additional calculation times, and is efficient for a large range of body shapes. However, despite the powerful modeling methods offered by this approach, free surfaces still engender additional errors when the thermoelasticity aspect of the problem is considered.

Finite element analysis (FEA) is another valuable simulation approach (Bachtar et al., 2006 ; Chatterjee & Sahoo, 2014 ; Sahoo & Ghosh, 2007 ; Yang & Komvopoulos, 2005). The FEA commercial software option can be quite easy to use, but quickly becomes complicated when the contribution of thermal factors such as thermoelasticity and/or FSI (Fluid Solid Interaction) need to be taken into account (Gropper et al., 2016 ; Lindemann et al., 2006 ; Reddy, 2015). Actually, even if a commercial software application is able to guarantee simple implementation, FEA still involves prohibitive mesh preparation times and computational costs. Given these FEA limitations, the SAM option is more common in contact problems (Hanson & Keer, 1995 ; Hartnett, 1980 ; Hetényi, 1960, 1970 ; Keer et al., 1983 ; J. Li & Berger, 2003 ; Junshan Li & Berger, 2001). Nevertheless, FEA is still quite helpful as a tool for validating other methods. In fact, as a validation approach, FEA is a widely accepted replacement for experimental investigations, especially for contact problems, which are entangled with considerable difficulties.

To the authors' knowledge, there are currently no SAM that can properly handle thermoelastic contacts with free edges. However, there are practical cases of thermal contacts partially or fully surrounded by free surfaces. In addition to the industrial applications mentioned earlier, contacts with textured surfaces (D.B. Hamilton, 1966 ; Etsion et al., 1999 ; Gropper et al., 2016 ; Wakuda et al., 2003) and some contacts in friction welding (Effertz et al., 2017 ; Jedrasiak, Shercliff, McAndrew, & Colegrove, 2018 ; Jl et al., 1991 ; Kuroki, Hiroshi; Nezaki, Koji; Wakabayashi, Tsukasa; Nakamura, 2014) are also relevant cases of configurations combining thermoelastic deformations and free edges .

The present work introduces an improved SAM handling about any thermoelastic contact definition, whether or not it involves free surfaces. The procedure comprises two parts. The first part introduces thermoelastic influence factors into the half-space-based SAM to account for thermoelastic displacements over the contact area. The second adjusts these thermoelastic influence factors to incorporate the influence of the thermal boundaries, namely to eliminate the normal component of the artificial thermoelastic stresses activated on the free surfaces by the half-space hypothesis.

The next section describes the rationale of the proposed SAM, and the sections that follow establish the thermal boundary condition treatment and thermoelastic normal stress elimination processes. The model development is followed by a validation comparing the model predictions with the FEA results obtained for a simple problem. Finally, the proposed method is used to describe the effect of thermoelasticity on the TEHL of line contact problems.

3.3 Method based on the half-space hypothesis

The Hartnett representation (Hartnett, 1980) puts into action the Boussinesq half-space formulation. Hence, the model presumes linear deformations. Eq. (3.1) gives the normal displacement at any point (x, y) of the half-space surface when a pressure $P(\xi, \zeta)$ is distributed over an area A of this surface:

$$w(x,y) = \frac{1-\nu^2}{\pi E} \iint_{\mathrm{A}} \frac{P(\xi,\zeta)}{\sqrt{(x-\xi)^2+(y-\zeta)^2}} d\xi d\zeta \tag{3.1}$$

where w is the displacement normal to the surface, ν the Poisson ratio, and E the Young modulus.

To define the contact conditions between two bodies, the Hartnett procedure also requires Eq. (3.2). This expression combines the initial separation (g) of body a and body b from the contact plane with their linear normal deformations (w_a, w_b). In Eq. (3.2), α is the normal approach of the bodies. This representation facilitates the inclusion of thermoelastic displacements (w_{TE}) of the half-space surface. Eq. (3.3) presents a modified formulation including the thermoelasticity contribution. Figure 3.1 illustrates the variables for both equations:

$$\begin{cases} w_a + w_b + g_a + g_b = \alpha & ,P > 0 \\ w_a + w_b + g_a + g_b > \alpha & ,P = 0 \end{cases} \tag{3.2}$$

$$\begin{cases} w_a + w_b - w_{TE_a} - w_{TE_b} + g_a + g_b = \alpha & ,P > 0 \\ w_a + w_b - w_{TE_a} - w_{TE_b} + g_a + g_b > \alpha & ,P = 0 \end{cases} \tag{3.3}$$

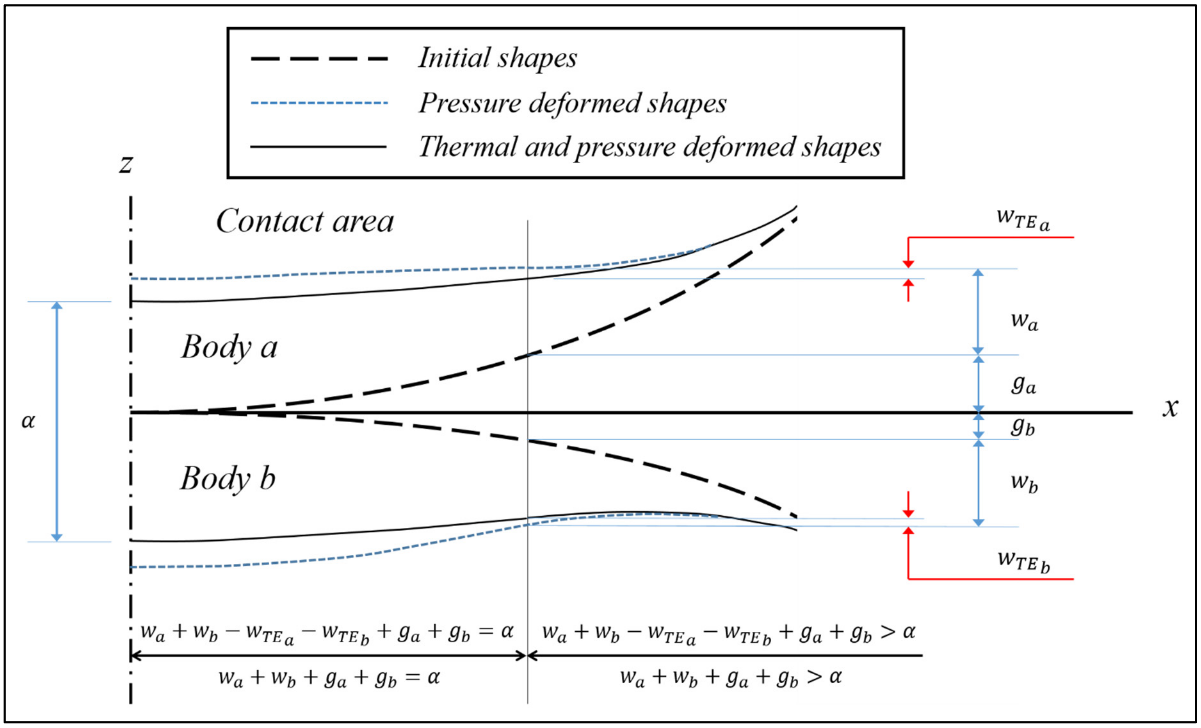

Figure 3.1 Contact definition

3.3.1 Half-space numerical approach for elastic deformation

The Hartnett SAM divides the contact plane, referred to as a blanket, into rectangular contact patches, each bearing a uniform pressure. Hence, for the contact patches belonging to the contact area, Eq. (3.2) may be rewritten as:

$$\sum_{A} P_i \times f_{ij} = \alpha - g_{a\,j} - g_{b\,j} \tag{3.4}$$

where f_{ij} are influence factors formulated by Eq. (3.5).

$$f_{ij}(x,y) = \left(\frac{1-{\nu_a}^2}{\pi E_a} + \frac{1-{\nu_b}^2}{\pi E_b}\right) \iint_A \frac{1}{\sqrt{(x-\xi)^2 + (y-\zeta)^2}} d\xi d\zeta \tag{3.5}$$

In Eq. (3.5), (*x, y*) are the Cartesian coordinates in a local coordinate system of the central point of the affected patch *j* with respect to the central point of patch *i* that supports the load.

3.3.2 Half-space stress formulation

The half-space theory formulates the elastic stresses (shear τ_{xz} and normal σ_x) caused at any position (x, y, z) by a concentrated force *F* active at $(0{,}0{,}0)$ the origin on the surface (the inward *z* axis is normal to the surface). Therefore, assuming that *F* and the normal to the examined free boundary are in the *z* direction and the *x* direction, respectively, while the space dimension along the *y* axis remains large, the dominant stresses active on the free surface may be reduced to the shear stress τ_{xz} and the normal stress σ_x. Eqs. (3.6) and (3.7) formulate these stresses:

$$\sigma_x = \frac{F}{2\pi}\left[\frac{(1-2v)}{d^2}\left\{\left(1-\frac{z}{c}\right)\frac{x^2-y^2}{d^2}+\frac{zy^2}{c^3}\right\}-\frac{3zx^2}{c^5}\right] \tag{3.6}$$

$$\tau_{xz} = -\frac{3F}{2\pi}\frac{xz^2}{c^5} \tag{3.7}$$

where $d = (x^2+y^2)^{\frac{1}{2}}$ and $c = (d^2+z^2)^{\frac{1}{2}}$.

3.4 Thermal aspects

The heat generated at different contact positions engenders thermal displacements which modify the contact conditions (Eq. (3.3). For dynamic contacts, heat generation usually results from dry friction, from lubricant shearing (Eq. (3.8), and compression (Eq. (3.9), or under a partial lubrication regime, from a combination of both conditions (Balci, Yildirim, & Dag, 2015 ; Sukumaran et al., 2018). In static contacts, it is often an electrical resistance at the surface junction between two bodies that causes a heat dissipation (Eq. (1.7)) (Bahrami, Yovanovich, & Culham, 2005 ; M. G. Cooper, B. B. Mikic, 1969 ; Mikic, 1974). As suggested in Eq. (3.3, the resulting thermoelastic displacements may be regarded as unidirectional and normal to the contact surface. $q''_{dry} = \mu PSS$, where q''_{dry} is the heat flux (W/m^2), μ is the coefficient of friction, *SS* is the sliding velocity (m/s), and *P* is the contact pressure (N/m^2).

$$q'''_{shear} = \eta\left[\left(\frac{\partial u_f}{\partial z}\right)^2+\left(\frac{\partial v_f}{\partial z}\right)^2\right] \tag{3.8}$$

where q'''_{shear} is the shear heat flux per length ((W/m^2)/m) or volumetric shear heat generation (W/m^3), η is the dynamic viscosity of the lubricant (Pas), u_f is the lubricant velocity in the flow direction (m/s), and v_f is the lubricant velocity in the lateral direction (m/s).

In TEHL contacts, compressive heating results from a pressure build-up at the inlet. It is also worth indicating that at the outlet, the pressure drop causes a lubricant decompression acting as a heat sink. This combined heating/cooling mechanism is designated as compressive heating.

$$q'''_{comp} = \beta T \left(u_f \frac{\partial P}{\partial x} + v_f \frac{\partial P}{\partial y} \right) \tag{3.9}$$

where q'''_{comp} is the compressive heat flux per length ((W/m^2)/m) or volumetric compressive heat generation (W/m^3), T is the lubricant temperature (°K), and β is the coefficient of thermal expansion of the lubricant (K^{-1}).

$$q''_{elec} = \frac{R_c I^2}{A} \tag{3.10}$$

where q''_{elec} is the electrical heat flux (W/m^2), R_c is the electrical contact resistance, I is the electrical current, and A is the contact area.

3.4.1 Thermoelastic displacement

Several studies have proposed analytical models to establish the thermoelastic displacements generated by a heat source acting on the surface of a half-space (Akbari, Sinton, & Bahrami, 2009 ; Barber, 1971 ; J. R., Barber, 1982 ; Sternberg & Mcdowell, 1957). These models show that a steady heat source applied on the surface of a half-space leads to infinite thermoelastic displacements of that surface. In order to provide better representations of real body conditions, in Ref. (Barber, 1971), Barber defined a heat-affected zone radius (s_0), allowing the thermoelastic displacements to be evaluated under steady-state conditions. Figure 3.2 illustrates the concept, while Eq. (3.11) gives the normal displacement w at a distance s smaller than s_0 from the heat source q.

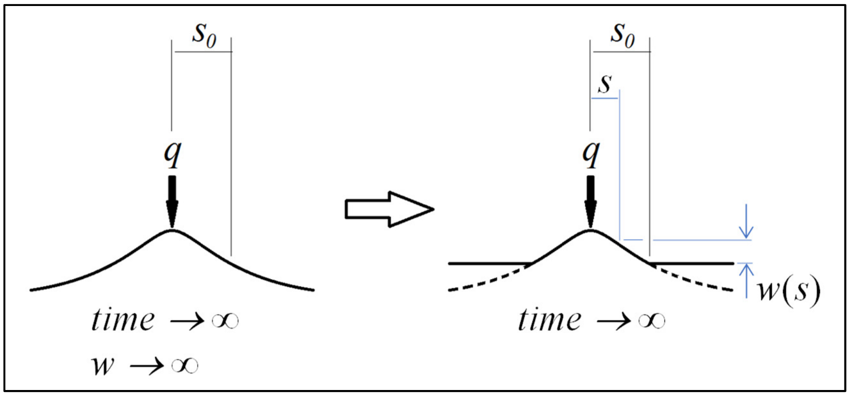

Figure 3.2 Steady-state thermoelastic displacement

$$w = \frac{q\gamma(1+\nu)}{2\pi k}\log\left(\frac{s_0}{s}\right) \tag{3.11}$$

where γ, k and ν are the coefficient of thermal expansion (°K^{-1}), the thermal conductivity (W/m °K) and the Poisson ratio of the half-space material, respectively.

Assuming there is a uniform heat flux (q'') over a rectangular patch of area *A*, and that s_0 is considerably larger than the dimensions of this patch, integrating Eq. (3.11) into *A* gives the overall thermoelastic displacement expressed by Eq. (3.12):

$$w = \frac{\gamma(1+\nu)}{2\pi k}\left\{q"\left(\log(s_0)\iint_A dA - \iint_A \log(s)\ dA\right)\right\} = \sum q"_i \times f_{TE} \tag{3.12}$$

where q'' is the heat flux (W/m^2). Eq. (3.12) indicates that the thermoelastic displacement at a position *s* of the surface caused by a given heat flux essentially depends on material properties and geometric parameters. Therefore, thermoelastic displacements may be predefined and integrated into a numerical process via a thermoelastic influence factor (f_{TE}). A multiplication of the heat generated over a given rectangular patch i by this influence factor gives the displacement at a position *s*. Thus, Eq. (3.13) integrates the thermoelastic displacements into Eq. (3.4) as follows:

$$\sum_A P_i \times f_{ij} - \sum_A q_i'' \times f_{TE_{ij}} = \alpha - g_{a_j} - g_{b_j} \tag{3.13}$$

Reference (Hartnett, 1980) offers a complete description of the implementation of Eq. (3.13) and of the associated solution algorithm. Eq. (3.14) formulates the thermoelastic influence factor defined for a displaced rectangular patch *j*, which has its center located at (*x, y*) with respect to the center of the loaded patch *i*. The lengths of patch *i* are 2a and 2b along the *x* and *y* axes, respectively. The patch size and position respect the mesh definition prepared for the elastic displacement calculations.

$$\begin{aligned} f_{TE,ij} = \frac{\alpha(1+\upsilon)}{2\pi k}\Bigg[&4\log(s_0)\, ab \\ &-\Bigg\{\Bigg[x_U y_U(\log(x_U{}^2 + y_U{}^2) - 3) + x_U{}^2 tan^{-1}\left(\frac{x_U}{y_U}\right) + y_U{}^2 tan^{-1}\left(\frac{y_U}{x_U}\right)\Bigg] \\ &-\Bigg[x_L y_U(\log(x_L{}^2 + y_U{}^2) - 3) + x_L{}^2 tan^{-1}\left(\frac{x_L}{y_U}\right) + y_U{}^2 tan^{-1}\left(\frac{y_U}{x_L}\right)\Bigg] \\ &-\Bigg[x_U y_L(\log(x_U{}^2 + y_L{}^2) - 3) + x_U{}^2 tan^{-1}\left(\frac{x_U}{y_L}\right) + y_L{}^2 tan^{-1}\left(\frac{y_L}{x_U}\right)\Bigg] \\ &+\Bigg[x_L y_L(\log(x_L{}^2 + y_L{}^2) - 3) + x_L{}^2 tan^{-1}\left(\frac{x_L}{y_L}\right) + y_L{}^2 tan^{-1}\left(\frac{y_L}{x_L}\right)\Bigg]\Bigg\}\Bigg] \end{aligned} \tag{3.14}$$

In Eq. (3.14), L and U indices refer to the lower and upper positions, respectively. Hence, $x_L = x - a$, $x_U = x + a$, $y_L = y - b$ and $y_U = y + b$.

The thermoelastic influence factor approach allows a straightforward integration of the thermoelastic displacements into the simple elastic process introduced by Hartnett (Hartnett, 1980). However, unlike the elastic displacements, which are inward when the surface sustains a pressure load, the thermoelastic displacements generated by a surface heat source are outward. Moreover, generally, the generated heat is a function of the contact pressure, while the contact pressure depends on both the elastic and thermoelastic displacements. As a result, the solution process of a thermoelastic model might be slightly less stable than that of a purely elastic model.

3.5 Free edge

SAM based on the half-space assumption, such as the Hartnett model, result in incorrect pressure increases in the vicinity of free surfaces of real bodies. These pressure rises result from artificial constraints of the free surfaces engendered by the internal shear and normal stress distributions that are inherent to the half-space assumption (Figure 3.3-a).

It has long been demonstrated that applying a counterbalance pressure eliminates the artificial shear stress from the free surface. The counterbalance pressures mirror the pressure distribution with respect to the free surface. Moreover, the additional operation introduced into the representation does not significantly affect the computation burden. The literature also offers exact correction methods to completely release the traction-free surfaces from the artificial normal stress (Hanson & Keer, 1995 ; Hetényi, 1970). However, these procedures require significant computation efforts. On the other hand, the approach put forward by Guilbault in (Guilbault, 2011) is simpler, while offering a comparable precision. The process removes the normal internal stress influence on the surface displacements without engendering any increase in calculation times; the mirrored pressures correcting the shear stress are multiplied by an overcorrection factor, which compensates for the normal stress influence on the surface displacements.

In reality, both elastic and thermoelastic displacement calculations can engender pressure increases close to the free surfaces. Here, *elastic* refers to the elastic response of the solids to a pressure, while *thermoelastic* refers to the thermoelastic response of the solids to a heat source.

The stress generated inside a half-space by a surface heat load is planar (Sternberg & Mcdowell, 1957); a surface heat load causes internal normal stress distributions, but no shear stress. Therefore, a thermoelastic modeling approach based on the half-space assumption results in inherent normal stress distributions (Figure 3.3-b) on any free surface. In reality, eliminating this undesired effect is not a real problem, since any of the strategies developed for the elastic problem may be adapted to this thermoelastic consideration. However, in addition the stress-strain aspect, the pattern of the inborn heat flux must also be adapted to the free boundary presence.

The next section introduces the procedure put forward to reproduce adiabatic or convective conditions over an internal surface of a half-space in order to simulate a free boundary, while Section 3.7 presents the normal stress elimination strategy adapted to the thermoelastic problem.

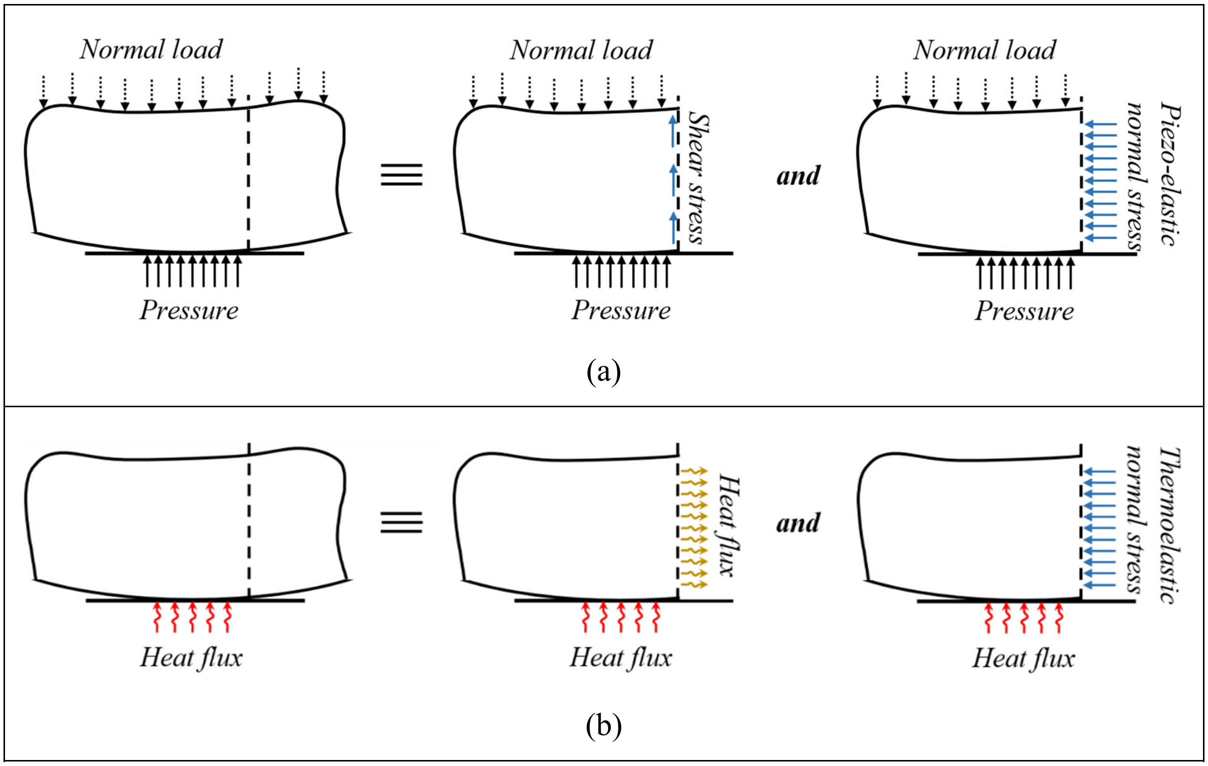

(a)

(b)

Figure 3.3 Repercussions of the half-space hypothesis on a boundary

3.6 Thermal correction for free boundaries

The definition of an adiabatic condition coincides with numerous practical situations. This state probably also corresponds to the easiest boundary condition to simulate for a free surface. Nevertheless, it cannot represent all physical situations. For many free surfaces where a convective heat transfer is dominant, the adiabatic assumption is not valid. Therefore, after an analysis of the adiabatic condition, Section 3.6.2 develops a general model suitable for any convective thermal boundary. Before that, however, Section 3.6.1 introduces the basic equations.

3.6.1 Heat flux generated by a heat load acting on the surface of a half-space

The internal heat flux generated by a steady-state heat load q (W) acting over a surface element (ΔA) of a half-space may be deduced in any direction from the associated temperature distribution. Eq. (3.15) formulates the half-space temperature distribution resulting from a steady-state heat load q (Mark Kachanov, Boris Shafiro, 2003):

$$\Delta T = \frac{q}{4\pi k} \frac{1}{\sqrt{x^2 + y^2 + z^2}} \tag{3.15}$$

where ΔT is the temperature variation, k is the thermal conductivity (W/m °K), and the *(x,y,z)* position indicates the temperature evaluation point in a local coordinate system located at the heat load position with axis *z* oriented inward.

Considering the Fourier's law ($q''_x = -k\,\partial(\Delta T)/\partial x$) and the temperature distribution given by Eq. (3.15), Eq. (3.16) establishes the heat flux along the *x* axis (q''_x in (W/m^2)). Eq. (3.17) describes a dimensionless version ($\overline{q''_x}$) of Eq. (3.16):

$$q''_x = -\frac{q}{4\pi}\left(\frac{x}{(x^2 + y^2 + z^2)^{3/2}}\right) \tag{3.16}$$

$$\overline{q''_x} = -\frac{4\pi q''_x}{q''} = \frac{\bar{x}}{(\bar{x}^2 + \bar{y}^2 + \bar{z}^2)^{3/2}} \tag{3.17}$$

where $q'' = \frac{q}{\Delta A}$ (W/m^2) is the heat flux acting on the surface of the half-space and $\bar{x}, \bar{y}, \bar{z}$ are dimensionless coordinates defined as $\bar{x} = \frac{x}{\sqrt{\Delta A}}, \bar{y} = \frac{y}{\sqrt{\Delta A}}, \bar{z} = \frac{y}{\sqrt{\Delta A}}$. Figure 3.4 shows $\overline{q''_x}$ distributions calculated along $\bar{z}$ for different $\bar{x}$ positions when $\bar{y} = 0$:

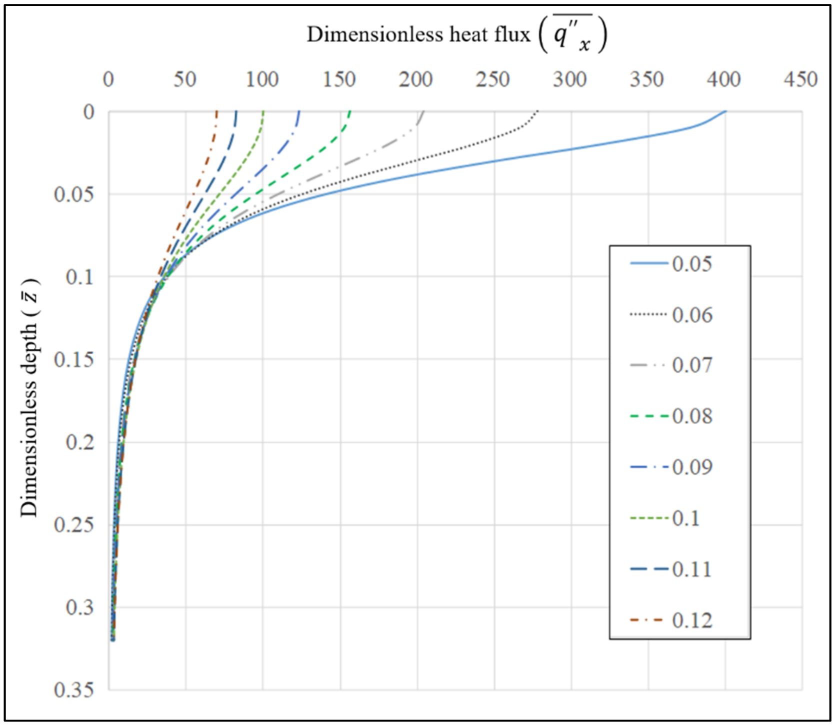

Figure 3.4 Dimensionless heat flux distribution at different $\bar{x}$ positions

3.6.2 Definition of the thermal boundary

An adiabatic boundary condition signifies the absence of a crossing heat flux. On the other hand, the half-space formulation supposes that the heat flux can propagate freely across an infinite domain. Thus, the simulation of a free surface under an adiabatic condition requires the elimination of the heat flux crossing this surface. The elimination process is quite simple: an opposite heat flux with an amplitude equivalent to that of the present flux should be generated on the free surface. A heat load mirroring the active heat load with respect to the free surface, or positioned on the opposite side at the same distance from the free surface, generates the desired heat flux. This thermal corrective strategy is designed to work with the Hartnett SAM. Thus, the original contact algorithm defined in (Hartnett, 1980) remains unchanged. The thermal part only integrates the heat flux effect over each original contact patch and corresponding mirror correction. Figure 3.5 illustrates the heat load mirroring operation. The figure also introduces the multiplier C_{bc}. This factor will allow generating conditions of convective heat transfer. Hence, the thermal boundary presented in Figure 3.5 is adiabatic when C_{bc} is set to 1.0.

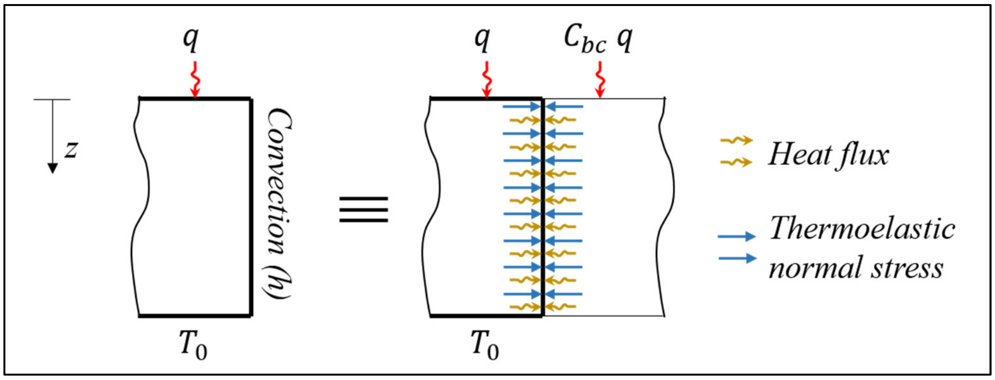

Figure 3.5 Thermoelastic boundary definition for a planar free surface

Under convective conditions, the coefficient of heat convection (h (W/m^{2}K)) quantifies the level of convective heat transfer over a surface area. The role of h is thus similar to that of k, the coefficient of heat conduction inside conductive material. Therefore, replicating a convective thermal boundary may be realized simply by assuming that another solid made of the same material, but with an adapted heat conduction coefficient, is connected to the free surface. Hence, while a C_{bc} value of one corresponds to an adiabatic condition, a zero value implies that the heat conduction is not affected by the presence of the free surface. Assuming a linear behavior for C_{bc} allows defining the appropriate value for each convection coefficient.

The dimensionless Biot number (Bi) given by Eq. (3.18) compares the internal thermal conduction to the surface thermal convection of a given solid (Incropera & De Witt, 1981). A $Bi = 1.0$ means that the conduction and the convection are equivalent. In Eq. (3.18), L_e is an effective length often defined as the ratio between the volume of the solid and its surface. Establishing a linear relation for C_{bc} from Eq. (3.18) is thus straightforward. Eq. (3.19) presents the obtained relation.

In the present problem definition, where the solids are considered as half-spaces, the common definition of L_e is not relevant. In reality, when analysing Eq. (3.19), it becomes clear that Bi may potentially be replaced by L_e, if this effective length is redefined as the separation between the actual solid and the adjoined body. This redefinition thus refers to a gap length (L_g) reflecting the coefficient of convection. Eq. (3.19) also shows the final formulation.

$$Bi = \frac{h}{k} L_e \tag{3.18}$$

$$C_{bc} = f(1 - Bi) = 1 - L_g \tag{3.19}$$

The correction procedure obtained with the combination of the factor C_{bc} and the mirrored thermoelastic cells is equivalent to the procedure described in Ref. (de Mul et al., 1986) for the elastic problem. The thermoelastic and elastic contributions are thus easily combined and solve simultaneously for various thermal boundary conditions. However, when limited to this procedure, both elastic and thermoelastic components generate normal stress distributions which remain active on the free surfaces.

3.7 Thermoelastic normal stress elimination on a free surface

The influence of the remaining thermoelastic normal stress distributions on the displacement of the contact surface may be corrected following an approach similar to the one proposed by Guilbault (Guilbault, 2011) for the elastic problem. The reference procedure overcorrects the influence of the shear stress to compensate for the effect of the normal stress distribution on the displacement of the half-space surface. This approach prevents additional computational efforts. Here, the correction strategy should modify the mirrored heat load to decrease the effects of the thermoelastic normal stress distribution on the displacement as well.

Although the procedure aims at correcting the influence of normal stresses engendered by a heat flux distribution over a given contact surface, the calculation process is essentially elastic, and leads to developments similar to those presented in (Guilbault, 2011). The calculation process involves the following steps: 1- it first calculates the total equivalent normal force present on the surface, as well as its position; 2- it applies an opposite normal force of the same amplitude at the position of the force to be corrected; 3- to avoid the generation of a shear stress distribution on the half-space surface, the process also applies a mirror correction force with respect to the half-space surface; 4- these two forces engender a new normal stress distribution over the half-space surface, which in turn must also be eliminated; 5- the previous steps are then repeated for the half-space surface. This process is alternatively repeated on the free boundary and the half-space surface and converges after an infinite number of iterations.

3.7.1 Basic stress and displacement equations

In agreement with the stress description presented in Section 3.3.2 , when the coordinate system remains as defined before with axis z oriented inward, the internal half-space stress $\sigma_{x_{te}}$ expressed by Eq. (3.20) (Mark Kachanov, Boris Shafiro, 2003) represents the influential thermoelastic stress component. This component is active in the x direction or normal to the free surface at the position $y = 0$. This position is in line with the corrective load located at a mirror position in the classical correction method described in Section 3.5 .

$$\sigma_{x_{te}} = -\frac{qG\gamma}{4\pi k}(1+\nu)\left[\frac{1}{z+\sqrt{x^2+z^2}}\right] \tag{3.20}$$

where q is a heat load acting on the half-space surface and G is the shear modulus.

Eq. (3.21) gives the total equivalent normal force (F_{TE}). This force results from the integration along z of the normal stress distribution over a given surface located at a position x. Eq. (3.21) converts the infinite range of the integral associated with the asymptotic behavior of $\sigma_{x_{te}}$ into a finite integration length. This length starts at the half-space surface and goes down to a defined physical depth (H). Eq. (3.22) gives the position of the line of action (l_{TE}) of F_{TE} along z.

$$F_{TE} = \int_0^{\infty} \sigma_{x_{te}} dz = -\frac{G\alpha}{4\pi k}(1+\nu)\int_0^{H} \frac{1}{z+\sqrt{x^2+z^2}} dz \tag{3.21}$$

$$l_{TE} = \frac{\int_0^{H} z\,\sigma_{x_{te}} dz}{F_{TE}} \tag{3.22}$$

Eq. (3.6) presented before gives the internal half-space elastic stress in the *x* direction. Eq. (3.23) shows a reduced version of the expression when *y* is set to 0:

$$\sigma_{x_e} = \frac{F}{2\pi}\left[\left(1-\frac{z}{\sqrt{x^2+z^2}}\right)\frac{(1-2\nu)}{x^2} - \frac{3zx^2}{(x^2+z^2)^{\frac{5}{2}}}\right] \tag{3.23}$$

As before with Eq. (3.21), for the total equivalent thermoelastic normal force *FTE*, Eq. (3.24) shows the total equivalent elastic normal force (*FE*). Again, this force results from the integration along *z* of the normal stress distribution over a given surface located at a position *x*. The infinite integral is also reduced to the same finite integration length *H*. Eq. (3.25) gives the position of the *FE* line of action (l_E) along *z*:

$$F_E = \int_0^{\infty} \sigma_{x_e} dz = \int_0^{H} \sigma_{x_e} dz \tag{3.24}$$

$$l_E = \frac{\int_0^{\infty} z\,\sigma_{x_E}\, dz}{F_E} \tag{3.25}$$

Eq. (3.11) provides a general formulation of the normal thermoelastic displacement of a half-space surface. Eq. (3.26) reduces this expression along the *x* axis. In this relation, the position *x* corresponds to the distance from the heat load (Barber, 1971). Similarly, Eq. (3.27) formulates the normal elastic displacement of the half-space surface at a distance *x* from the normal force active on the half-space surface (Johnson, 1987):

$$w_{TE} = \frac{q\gamma(1+\nu)}{2\pi k}\ln\left(\frac{s_0}{x}\right) \tag{3.26}$$

$$w_E = -\frac{F(1-\nu)}{2\pi G x} \tag{3.27}$$

Finally, Eq. (3.28) gives the internal elastic displacement in the *x* direction (u_E) along the *x* axis and at a given depth *z* from the half-space surface, when *y* is 0 (Johnson, 1987):

$$u_E = \frac{F}{4\pi G}\left[\frac{zx}{c^3} - (1-2\nu)\frac{x}{c(c+z)}\right] \tag{3.28}$$

where $c = \sqrt{x^2 + z^2}$.

3.7.2 Normal stress elimination process

The remaining thermoelastic normal stress on the free surface results from a combination of the effects of both the initial and the mirror heat loads. Therefore, the adiabatic thermal boundary, which imposes the maximum mirror heat loads, leads to the largest normal stress amplitude. Thus, the following study considers the adiabatic boundary condition (C_{bc} = 1) to analyse the thermoelastic normal stress elimination process.

The following description is illustrated in Figure 2.10. In addition to their contribution to the displacement of the half-space surface (given by Eq. (3.26)), a heat load *Q* acting on a half-space surface at a distance $l_{z_{TE}}$ from the free edge (along the *x* direction) and its mirror load *Q'* engender a superposition of normal stress distributions $\sigma_{x_{te}}$ on the free surface. Eliminating this thermoelastic normal stress combination requires a counterbalancing equivalent normal stress. The proposed procedure replaces the generated normal stresses with their equivalent forces F_{TE} (calculated by Eq. (3.21)). The total antagonistic force is then applied at a distance $l_{x_{TE}}$ from the half-space surface or at the position of the action line of F_{TE} defined by Eq. (3.22). In turn, this correction force generates shear and normal stresses on the half-space surface. A correction force F_{TE}' placed at a mirror position with respect to the surface half-space eliminates the shear stress. These two correction forces then cause additional elastic displacements of the half-space surface, which are deduced from a rotated version of Eq. (3.28). They also cause a superposition of elastic normal stresses (σ_{ze}) in the *z* direction on the half-space surface. These stresses and their equivalent forces in the *z* direction, as well as their acting positions, are established by a formulation equivalent to the one given by Eq. (3.23) to Eq. (3.25) along the *x* axis. An equivalent force F_{E_1}may thus be applied to eliminate the force generated normal to the plan of the half-space surface. This corrective operation again requires the action of a force $F_E{'}_1$ mirroring F_{E_1}. In addition to their contribution to the elastic displacement of the half-space surface calculated with Eq. (3.27), these correction forces cause the reoccurrence of a normal stress distribution on the free surface, which requires the addition of the correction force mirror set comprised of $F_{E_2}$and $F_E{'}_2$. These first few elimination steps conclusively initiate an iterative correction process. Since the positions of the force action line (illustrated by Eq. (3.25)) increase at each iteration, the process is convergent. The present description summarizes the detailed explanations of the procedure published by the authors in Refs. (Guilbault, 2011 ; Yalpanian & Guilbault, 2020). The reader is thus referred to these papers for a complete portrayal.

At the end of the releasing process of the free boundary, the displacement of the half-space surface at the position of the initial heat load Q will combine the displacement contributions w_{TE-Q} and $w_{TE-Q'}$ (Eq. (3.26)) produced by Q and its mirror heat load Q', respectively, the displacement $u_{E-F_{TE'}}$ (Eq. (3.28)) produced by the mirror load F_{TE}', as well as the contributions $w_{E-F_{E1}'}$ (Eq. (2.19)) produced by the mirror load F_{E1}'. To these displacements, the complete iterative process will pile up displacements $\left(w_{E-F_{E'}}\right)_i$ and $\left(u_{E-F_{E'}}\right)_i$ engendered by the elastic correction forces. Hence, the complete iterative correction will cause a final half-space surface displacement $w_{Q_{total}}$ given by Eqs. (3.29-a) and (3.29-b).

$$w_{Q_{total}} = w_{TE-Q} + w_Q \tag{3.29-a}$$

$$w_Q = w_{TE-Q'} + u_{E-F_{TE'}} + \sum_{i=1}^{\infty}\left(w_{E-F_{E'}}\right)_i + \sum_{i=1}^{\infty}\left(u_{E-F_{E'}}\right)_i \tag{3.29-b}$$

In order to avoid the calculation efforts involved in the correction process described by the infinite series in Eqs. (3.29-a) and (3.29-b), the proposed correction strategy assumes instead that a modified mirror heat load Q^* located at $l_{z_{TE}}$ from the free boundary at the mirroring position should produce a displacement of the half-space surface equal to w_Q. Thus, Q^* should

$$Q^* = \left[{}^{w_Q}\!/_{w_{TE-Q'}}\right] Q = nsf_{TE} Q \tag{3.30-a}$$

$$nsf_{TE} = \left[{}^{w_Q}\!/_{w_{TE-Q'}}\right] \tag{3.30-b}$$

be calculated as indicated by Eq. (3.30-a), where nsf_{TE} is the thermoelastic normal stress elimination factor. This factor is thus written as indicated by Eq. (2.31).

Eq. (3.30-b) allows calculating nsf_{TE} for any $l_{z_{TE}}$. The equation system formed by Eq. (3.20) to Eq. (3.28) depends on the Poisson ratio. Here, in order to simplify the calculations, the Poisson ratio is initially fixed at a constant value of 0.3, since this value is compatible with most engineering materials.

The formulation of Eq. (3.30-b) concentrates the influence of the normal stresses generated by heat loads on the surface displacement. To evaluate nsf_{TE}, a series of simulations considering various $l_{z_{TE}}$ distances of the heat load from the free boundary were realized. The investigation examined dimensionless distances $\bar{x} = l_{z_{TE}}/s_0$, where s_0 was fixed at 10 mm. Figure 2.11 displays the obtained results. The results are also summarized by the curve fit given by Eq. (3.31). Figure 2.11 shows that the calculated nsf_{TE} factors are always lower than 3%, and globally below 1%. They thus have no significant effect on the contact pressure calculation. Therefore, it is reasonable to conclude that the influence on the surface displacement of the internal normal stress distributions engendered by a heat load on a half-space may be neglected, and a sole correction of the heat fluxes crossing the free boundaries is sufficient.

Since the nsf_{TE} calculation included (Eq. (3.31)) only considered a 0.3 Poisson ratio, the second half of the investigation examined the changes caused by modifications of the Poisson ratio. While the final results are not included here, they showed that the thermoelastic normal stress effects also remain inconsequential with other Poisson ratios.

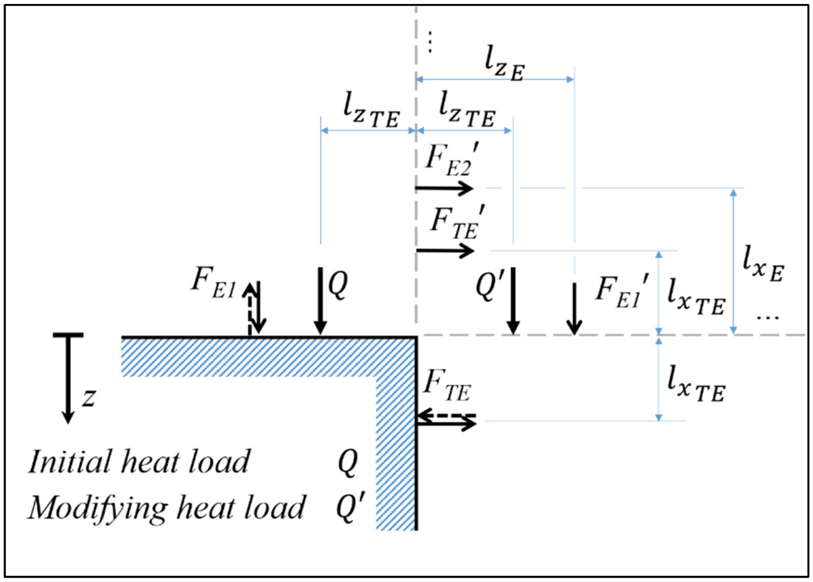

Figure 3.6 First few actions of the artificial stress correction procedure

$$nsf = \frac{\bar{x}^5 - 15.3\bar{x}^4 + 289.6\bar{x}^3 + 125\bar{x}^2 + 32.9\bar{x} + 37.83}{\bar{x}^5 - 15.32\bar{x}^4 + 292.1\bar{x}^3 + 118.2\bar{x}^2 + 35.37\bar{x} + 36.51} \tag{3.31}$$

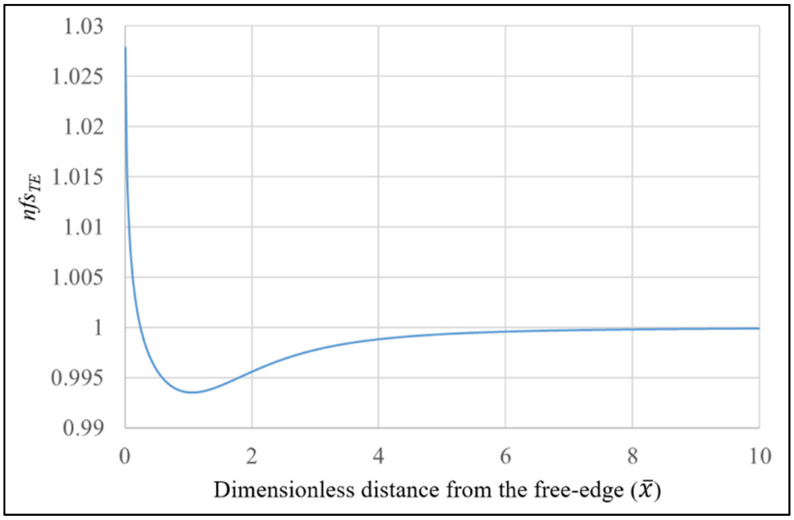

Figure 3.7 Thermoelastic normal stress correction factor

3.8 Validation

Figure 3.8 shows a very thick square solid of area l^2 submitted to a constant heat flux q''. Four straight free boundaries form this solid. To validate the proposed modeling strategy, its displacement predictions are compared to the thermoelastic displacement results obtained from a Finite Element Analysis (FEA) of the same solid submitted to the same heat flux q''. The present comparison considers that the free boundaries are under adiabatic conditions (FEA and proposed method). Figure 3.8 also shows the FEA model of the solid bar. The bar length is 10 *l*, the mesh is made of solid 8 node elements, and the bar cross-section is meshed with 71 x 71 constant length elements, while the lengthwise mesh is progressive and is composed of 100 divisions. Finally, in addition to the constant heat flux q'' applied on the top surface, the lower surface is insulated.

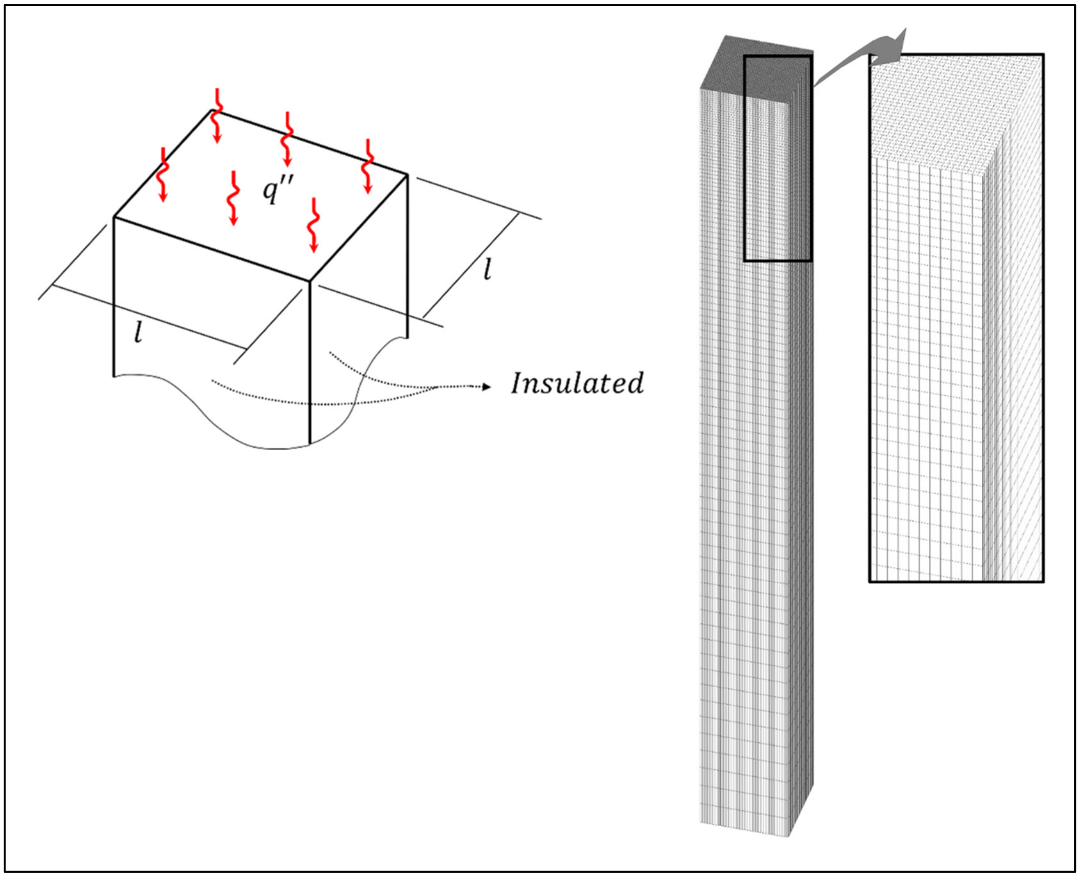

Figure 3.8 Validation model

As mentioned earlier, the proposed method requires the definition of a heat-affected zone radius (s_0). In order to cover the complete area and the additional surface involved during the mirroring procedure, the radius s_0 is set to $2\sqrt{2}l$. Figure 3.9 shows the radius of the included thermoelastic zone when the lower right corner of the area is considered.

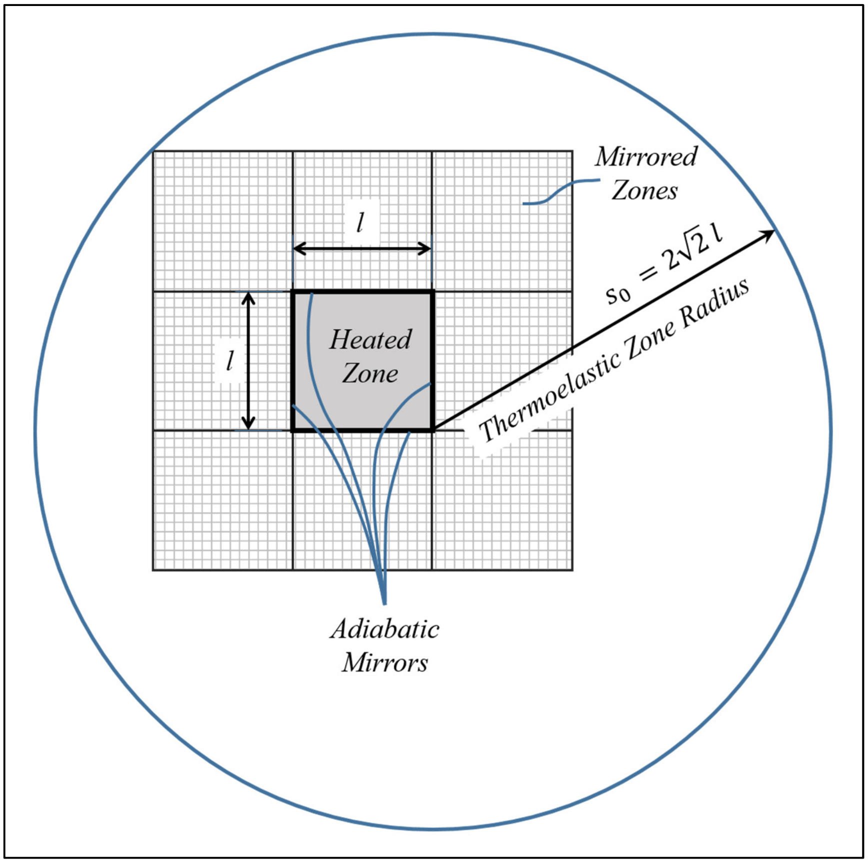

Figure 3.9 Definition of the adiabatic zone and thermoelastic zone radius

Figure 3.10-a superimposes the model predictions (identified as ATE) and the FEA results obtained for the adiabatic condition. In addition, in order to put the influence of the adiabatic thermal condition into perspective, the graph in Figure 3.10-a also includes the thermoelastic displacements predicted by the model when imposing no thermal correction (identified as TE). The presented values were taken along the diagonal direction of the heated zone. They compare the thermoelastic displacement w_{TE} to w_{TE_C}, the thermoelastic displacement calculated at the center of the contact area. The abbreviations TE and ATE refer to the model calculations made considering the thermoelastic and the adiabatic thermoelastic conditions, respectively. The curves in Figure 3.10-a show that the model predictions for the adiabatic thermoelastic conditions (ATE) are in perfect agreement with the results obtained from FEA with adiabatic

thermoelastic conditions. Moreover, a comparison of the TE and ATE curves demonstrates the influence of the free boundary heat flux correction.

Since the proposed solution is designed to be integrated into a contact model composed of rectangular pressure cells, it also requires a division of the surface into rectangular cells. The results of Figure 3.10-a were obtained for a grid made of 71 x 71 square cells. To illustrate the influence of the grid resolution, Figure 3.10-b compares the results obtained for different grid sizes: 71 x 71, 105 x 105 and 141 x 141 square cells. Since Figure 3.10-a demonstrates that ignoring the thermal correction (TE curve) significantly reduces the result accuracy, Figure 3.10-b only includes the displacements calculated when considering the ATE condition. To complete the comparison, Figure 3.10-b also displays the FEA results. Although the numerical noise in all grid sizes is virtually negligible, Figure 3.10-b shows that finer meshes cause less numerical noises. In fact, the curves suggest that the precision of the proposed approach is not really affected by the grid size. On the other hand, the calculation time also depends on the grid size. Table 3.1 indicates the calculation time of each configuration. The computation time of the FEA was 780 sec. Table 3.1 also compares the computation time associated with each grid size to that of the FEA, and indicates the reduction obtained.

Since finer meshes do not significantly improve the precision, and because the computation time substantially increases with the cell numbers, it is reasonable to conclude that the cell size and the grid definition may be solely established from the contact modeling requirements or the elastic part of the problem.

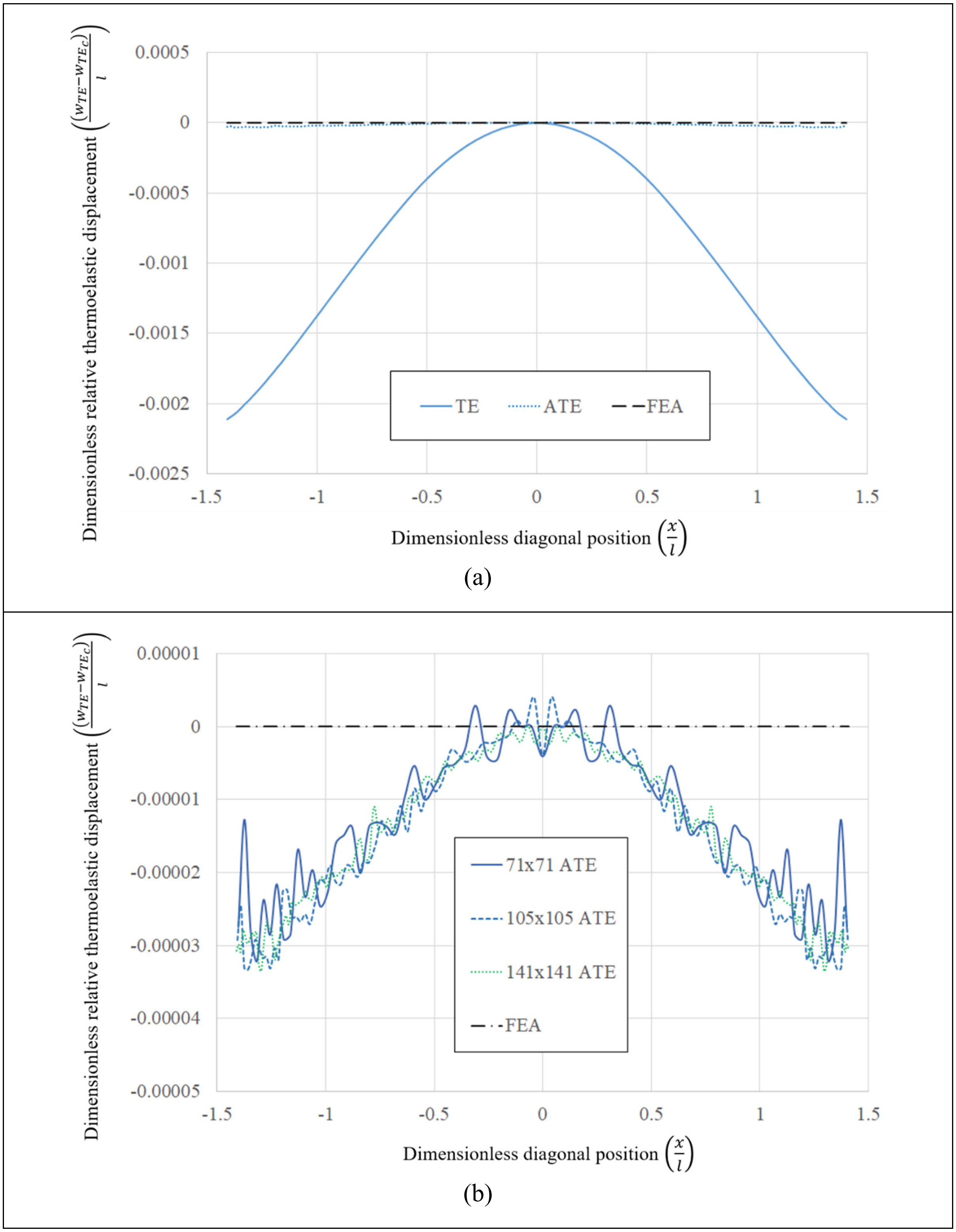

Figure 3.10 Grid size effect comparison for adiabatic thermal boundary

Table 3.1 Computation times for various grid sizes compared to FEA

	Grid size		
	71×71	105×105	141×141
Time (sec)	*10*	*48*	*154*
Time reduction (%)	*98.7*	*93.9*	*80.3*

3.9 Thermoelasticity and thermal boundary definition in TEHL

As mentioned earlier, thermoelasticity potentially changes TEHL conditions. The proposed thermoelastic simulation approach may easily be integrated into an elastohydrodynamic model. The TEHL model put forward in (Najjari & Guilbault, 2014) was reproduced for the present study, and the developed thermoelastic model was integrated into the solution procedure. In order to put the thermoelasticity effects into perspective and illustrate the influence of the thermal boundary condition on TEHL, the analysis below examines 27 configurations combining three levels of the following parameters: 1- the lubricant viscosity, 2- the entraining velocity and 3- the applied load. These configurations are each submitted to three modeling conditions: a) a thermal elastohydrodynamic lubrication or TEHL condition, b) a thermoelastic TEHL, where the half-space intrinsic heat flux is not eliminated from the boundaries or TTEHL condition, and c) a thermoelastic TEHL, where the half-space intrinsic heat flux is eliminated from the boundaries to produce an adiabatic boundary condition or TTEHL-TB condition. Since the adiabatic condition is the more potent condition, the presented analysis does not consider the convective condition. To help in the analysis of the resulting 81 layouts, Section 3.9.2 begins with a description of a specific case. Moreover, before the thermoelastic aspect is incorporated into the EHL model, Section 3.9.1 first demonstrates the capacity and precision of the TEHL model prepared for this investigation. As Ref. (Najjari & Guilbault, 2014) provides a complete description of the original TEHL, the present study does not depict it. The two models are completely equivalent. In particular, they include the non-Newtonian behavior of the lubricant.

3.9.1 TEHL model

In Ref. (Wymer & Cameron, 1974), Wymer and Cameron published experimental film thickness measurements for various line contact conditions. The author of Ref. (Najjari & Guilbault, 2014) validated their model via a comparison with the Ref. (Wymer & Cameron, 1974) results. The present validation adopts the same strategy. Thus, Figure 3.11 superimposes the Wymer and Cameron's film measurements on the model predictions. Table 3.2 provides the roller geometry and the lubricant properties values required for the calculations (Najjari & Guilbault, 2014).

Figure 3.11 demonstrates that the results obtained from the prepared TEHL model conform quite well to the experimental measurements taken along both the rolling and the axial directions. Based on this graphical comparison, the next sections consider that the TEHL model predictions are fully valid.

Table 3.2 Mechanical properties of the solids and the oil tested by Wymer and Cameron (Taken from Ref. (Najjari & Guilbault, 2014))

Cylinder	
Radius R (mm)	4.1
Length L (mm)	13.7
Total cone angle (degree)	7.9
Elastic modulus E (GPa)	206
Poisson ratio v	0.3
Density ρ (kg/m^3)	7850
Thermal conductivity k (W/(m °K))	46
Specific heat (J/(kg °K))	470
Flat surface	
Elastic modulus E (GPa)	75
Poisson ratio v	0.22
Density ρ (kg/m^3)	2500
Thermal conduct k (W/(m °K))	0.78
Specific heat (J/(kg °K))	840
Oil	
Baseline temperature T_0 (°K)	313
Viscosity at 303 °K (Pa.s)	0.900
Viscosity at 393 °K (Pa.s)	0.015
Visc.-Press. coef. at 303 °K (GPa^{-1})	30.2
Visc.-Press. coef. at 393 °K (GPa^{-1})	16.4
Density ρ at 313 °K (kg/m^3)	888
Density ρ at 373 °K (kg/m^3)	853
Thermal conductivity k (W/(m °K))	0.125
Specific heat (J/(kg °K))	2000
Modulus G at 303 °K (GPa)	0.1+3.0*P
Slope factor n at 313 °K	0.570
Slope factor n at 373 °K	0.993

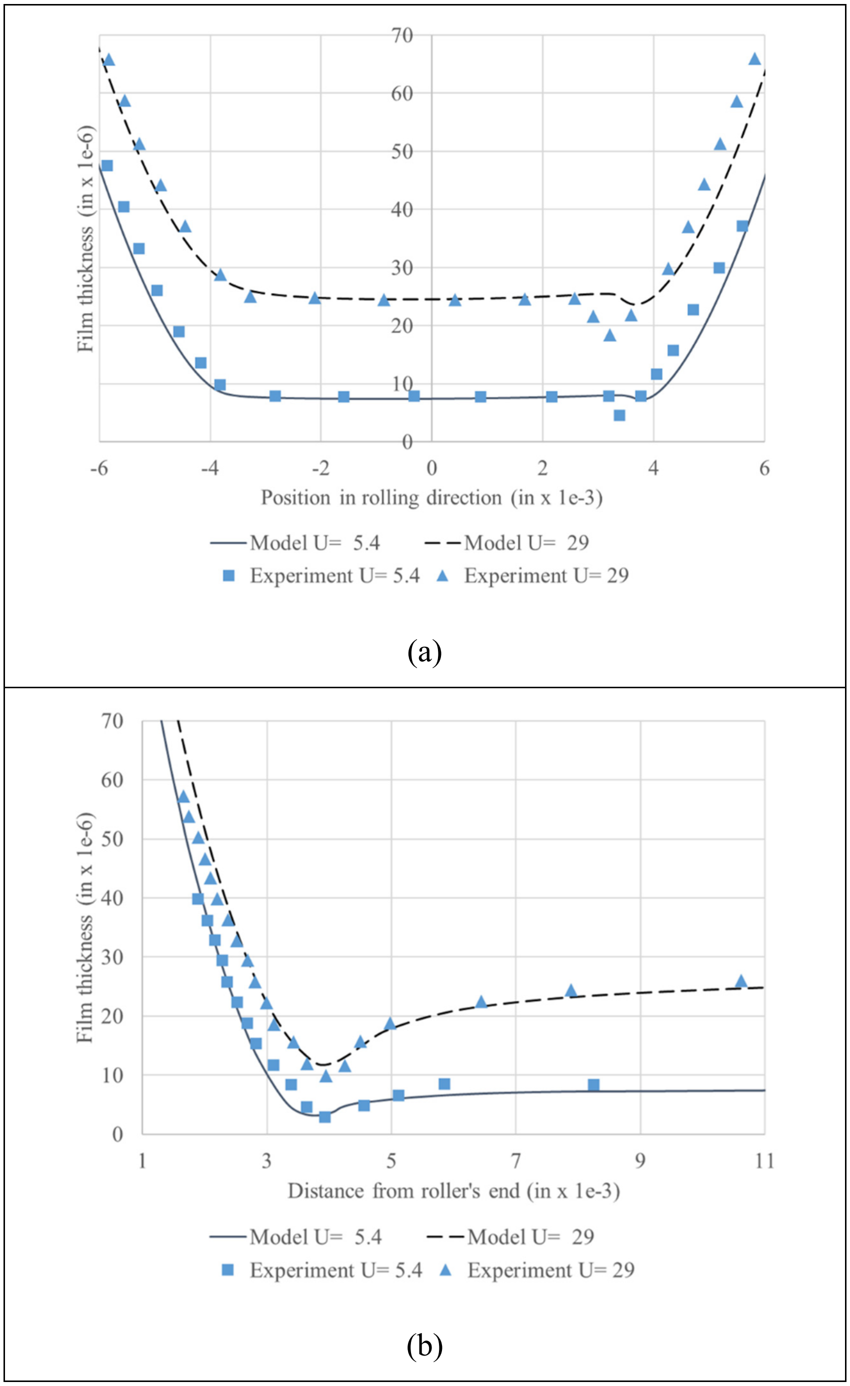

(a)

(b)

Figure 3.11 Comparison of the TEHL film thickness results for two dimensionless velocities ($\overline{U}$) (Experimental results from (Najjari & Guilbault, 2014 ; Wymer & Cameron, 1974)); (a) Central film thickness in rolling direction and (b) Film thickness in the axial direction

3.9.2 Comparison of the EHL, TEHL, TTEHL and TTEHL-TB results obtained for a specific case

The factorial design of Section 3.9.3 considers the contact family described by an equivalent cylinder of radius (R) 20 mm and length (L) 10 mm pressed against a flat surface of the same length. Table 3.3 shows the properties of material of the contact pair and lubricant, respectively. The present section examines the system where the active load (F) is 4000 N, the lubricant entraining speed (*ES*) is 23 m/s, the sliding speed (*SS*) is 2.4 m/s, while the lubricant viscosity grade (*ISO VG*) is 150.

The description below involves the following dimensionless variables: the contact pressure P/P_H, where P and P_H are the contact pressure and the maximum Hertzian pressure, respectively, and the positions $\frac{x}{b}$ and $\frac{y}{b}$ in the rolling and the axial directions, respectively. In these definitions, b denotes the half width of the contact area.

Table 3.3 Mechanical properties of the solids and oil

Solid material	
Elastic modulus E (GPa)	206
Poisson ratio v	0.3
Density ρ (kg/m^3)	7850
Thermal conduct k (W/(m °K))	47
Specific heat (J/(kg °K))	460
Oil	
Baseline temperature T_0 (°K)	313
Viscosity at 313 °K (Pa.s)	0.1335
Viscosity at 373 °K (Pa.s)	0.0132
Visc.-Press. coef. at 313 °K (GPa^{-1})	12.306
Visc.-Press. coef. at 373 °K (GPa^{-1})	9.201
Density ρ at 313 °K (kg/m^3)	890

Density ρ at 373 °K (kg/m^3)	870
Thermal conduct k (W/(m °K))	0.14
Specific heat (J/(kg °K))	1880
Gamma ratio	0.046
Slope factor n at 313 °K	0.60
Slope factor n at 373 °K	0.99

Figure 3.12 compares the contact pressures predicted for the examined conditions: TEHL, TTEHL and TTEHL-TB. In addition, to complete the description and illustrate the influence of variations of the lubricant properties caused by the temperature, the figure also integrates the EHL condition into the graphical comparison. Figure 3.12-a to d display the map plots, while Figure 3.12-e and f show the linear distributions measured along the rolling direction at the mid-position and in the axial direction along the initial contact line, respectively.

A comparison of Figure 3.12-a and b (EHL and TEHL) indicates, for this specific layout, that the influence of the temperature on the non-Newtonian response of the lubricant tends to concentrate the maximal pressure amplitude toward the center of the contact, and to extend the distribution into the outlet zone. It also reduces the outlet spike. Figure 3.12-e and f also clearly depict these effects.

Adding the thermoelasticity consideration without considering the thermal boundary (TTEHL) leads to a contact pressure profile closer to that of a point contact. The results displayed in Figure 3.12-c, e and f evidence this outcome. This tendency is due to the fact that the thermoelasticity contribution depends on the pressure. Since the heat flux at the cylinder and surface ends is not restricted, the thermoelasticity impact becomes more important far from the body limits. Consequently, the thermal deformation tends to inflate the surface more significantly in the middle of the maximum pressure zone.

Eliminating the heat flux at the contact extremities via an adiabatic condition (TTEHL-TB) reduces the influence of the contact boundaries and mitigates the concentration of the thermal deformation in the central portion of the pressure zone. However, even though the generated heat deforms the surface more evenly, the thermal deformation still visibly modifies the pressure distribution. Comparing the plot of Figure 3.12-d with that of Figure 3.12-b reveals, for this specific layout, that the dimensionless pressure increases from 1.2 to 1.32. More specifically, Figure 3.12-e indicates maximum dimensionless pressures of 1.25 and 1.37 for the TEHL and TTEHL-TB simulations, respectively, which corresponds to an increase of 9.6%. While this thermoelasticity effect is not severe, it is clearly not negligible. Moreover, it is important to recall here that the simulation considered an adiabatic condition for the free boundaries, and because that condition causes significant thermal changes in the boundary areas, it results in less impactful consequences on pressure distributions than convective conditions. Therefore, we can reasonably assume that real boundaries, which should be better represented by mixed conduction-convection conditions, allow some level of heat flow, and hence, have a more impactful influence on pressure distributions. It may thus be conjectured that pressure increases caused by free boundaries described by precisely known thermal boundary conditions should be closer to an intermediate response between the increases associated with the TTEHL and the TTEHL-TB. Section 3.9.3 sheds more light on the influence of the thermal boundary condition on the pressure distributions and on the possible interactions among the factors of the factorial design.

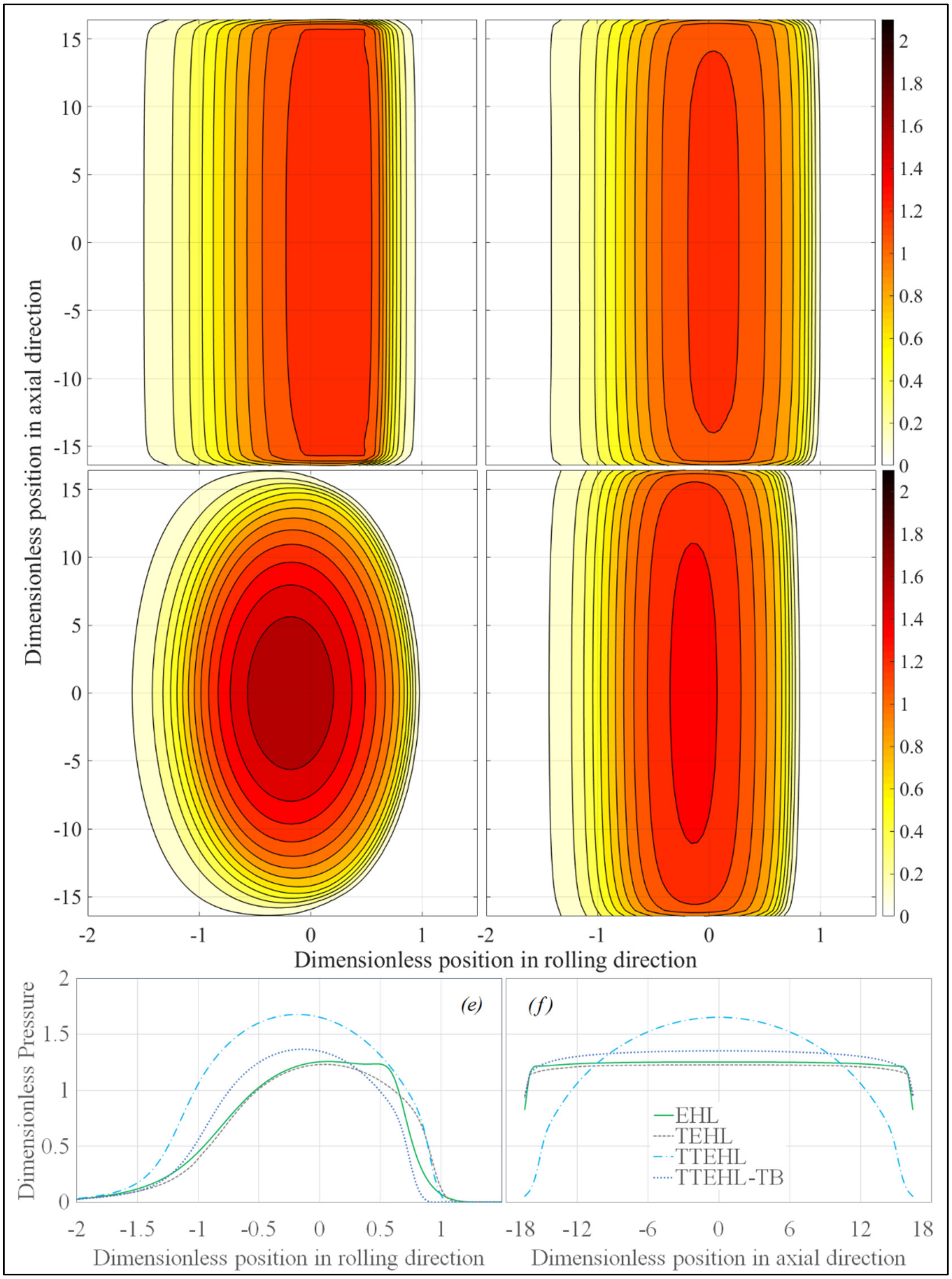

Figure 3.12 Dimensionless contact pressure for four different assumptions: a- EHL, b- TEHL, c- TTEHL, d- TTEHL-TB, e- Dimensionless pressure at the mid-section in rolling direction, f- Dimensionless pressure at the mid-section in axial direction

3.9.3 Factorial design analysis

The considered factorial design constructed for the cylindrical contact family *R* - 20 mm, *L* - 10 mm (cylinder against a flat surface), includes three levels of factor *F* (the applied load), of factor *ES* (the lubricant entraining speed), and of factor *ISO VG* (the lubricant viscosity grade), while *SS* (the sliding speed) is fixed at 2.4 m/s and the lubricant temperature at the contact inlet position is 333°K. Table 3.4 shows the factor levels.

Table 3.4 Factor levels

Factors	Levels		
	-1	0	1
F (N)	*4000*	*6000*	*8000*
ES (m/s)	*3*	*13*	*23*
ISO VG	*100*	*150*	*220*

The proposed investigation analyses the factor effects on three contact parameters: the dimensionless form of the maximum contact pressure (*MP* = P/P_H), the maximum contact temperature measured in°K (*MT*), and a dimensionless form of the minimum film thickness (*MF*). This dimensionless thickness is defined as h_0/R, where h_0 is the minimum film thickness and R is as defined above the equivalent cylinder radius. The materials properties are those indicated in Table 3.3. Figure 3.13, Figure 3.14 and Figure 3.15 present the two-factor interaction plots prepared for *MP*, *MT, MF*, respectively, when taking the three modeling conditions (TEHL, TTEHL and TTEHL-TB) into consideration. In these graphs, the horizontal axe describes the lowest (-1), the middle (0), and the highest (1) levels of the factors defined in Table 3.4. To complete the description, Table 3.5, Table 3.6 and Table 3.7 present the values of the factor main effects and of their interactions calculated for *MP*, *MT, MF*, respectively.

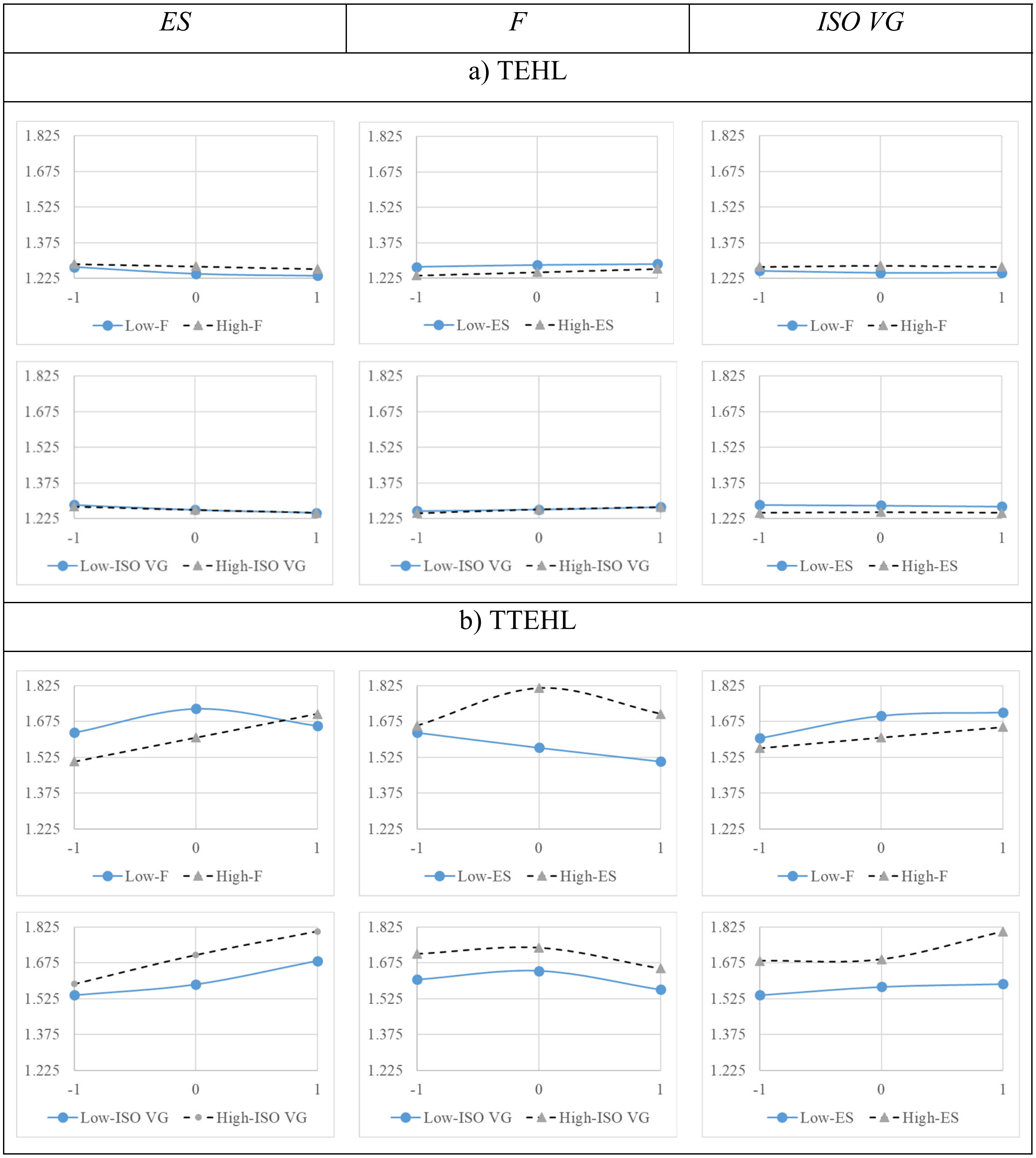
ES
F
ISO VG
a) TEHL
b) TTEHL
1.825
1.675
1.525
1.375
1.225
-1
0
1
Low-F
High-F
Low-ES
High-ES
Low-ISO VG
High-ISO VG

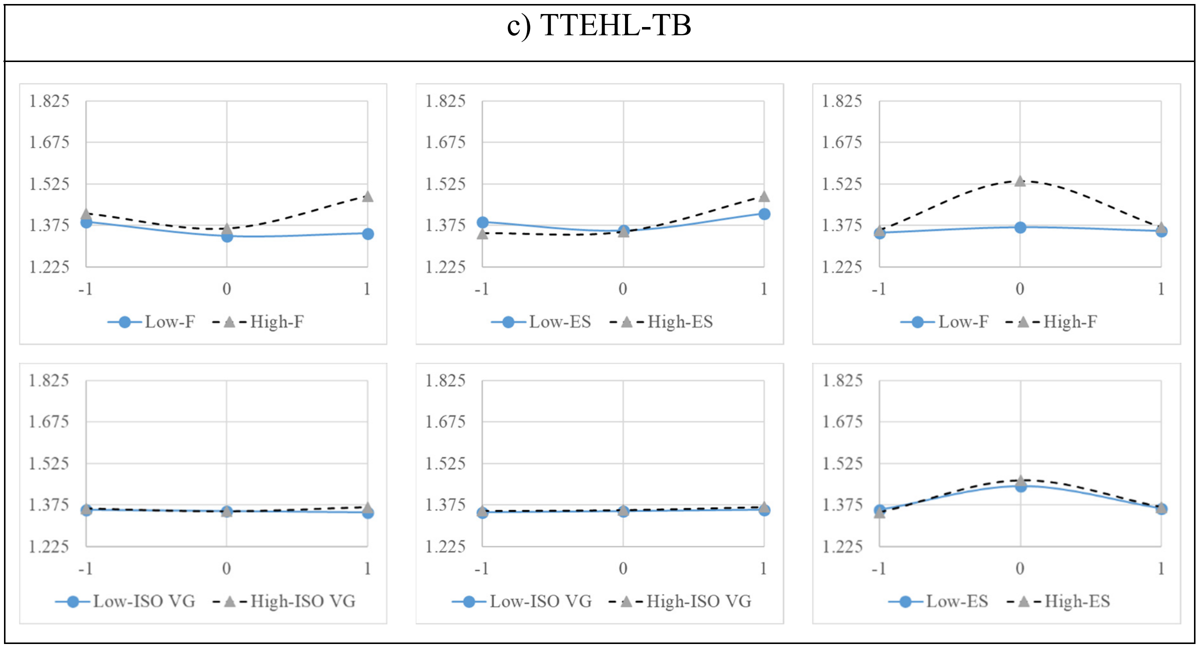
c) TTEHL-TB

Figure 3.13 MP- Interaction plots for the TEHL, TTEHL and TTEHL-TB modeling conditions

Table 3.5 Factor main and interaction effects on MP

Effects	TEHL	TTEHL	TTEHL-TB
F	*0.02422*	*-0.06431*	*0.06396*
ISO VG	*-0.00238*	*0.09737*	*0.00754*
ES	*-0.02951*	*0.15921*	*0.00572*
F-ES	*0.00784*	*0.08529*	*0.05186*
ES-ISO VG	*0.00318*	*0.03892*	*0.00691*
ISO VG-F	*0.00419*	*-0.00930*	*0.00232*
F-ES-ISO VG	*0.00520*	*0.00536*	*-0.00485*

ES	*F*	*ISO VG*
a) TEHL		
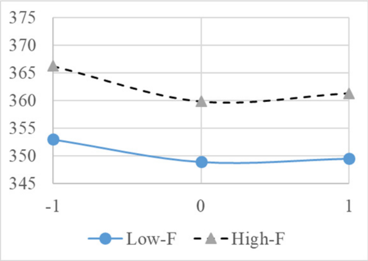	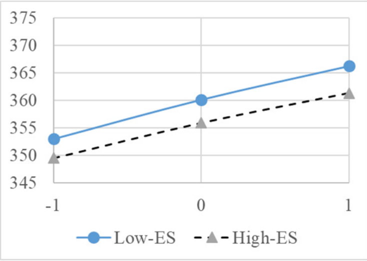	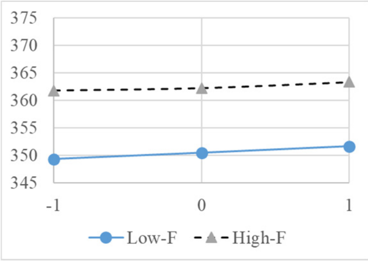
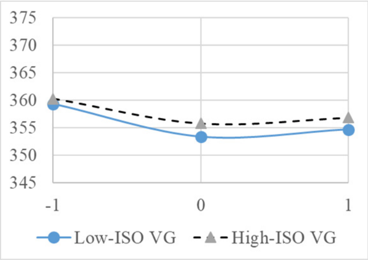	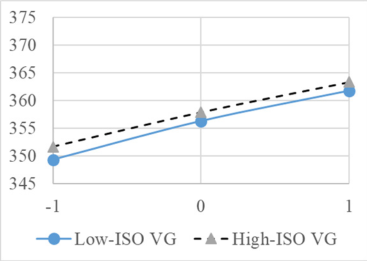	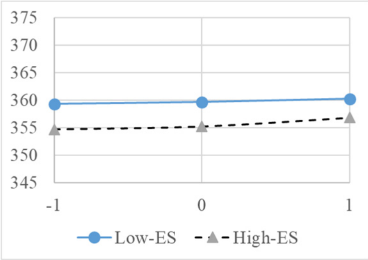
b) TTEHL		
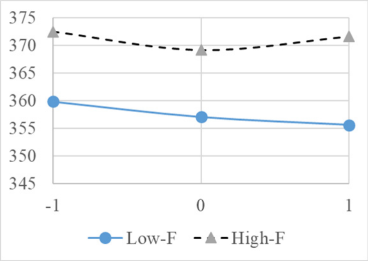	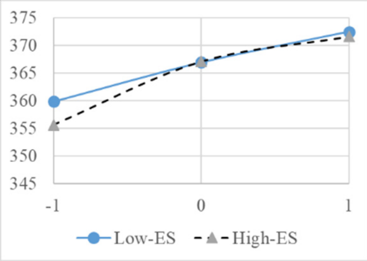	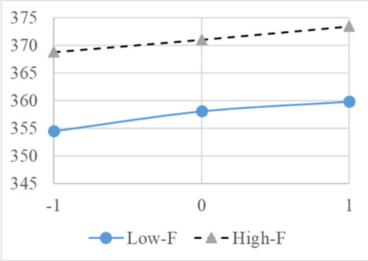
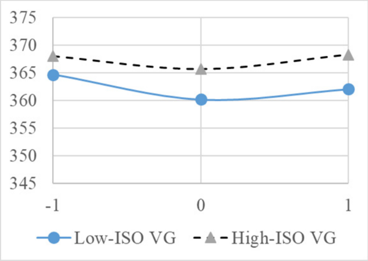	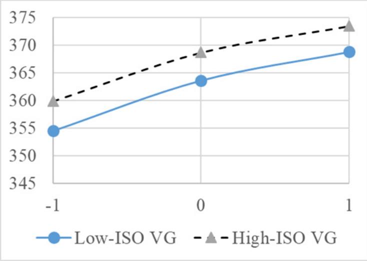	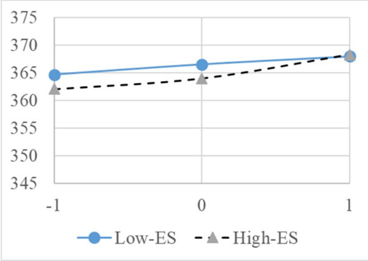

c) TTEHL-TB

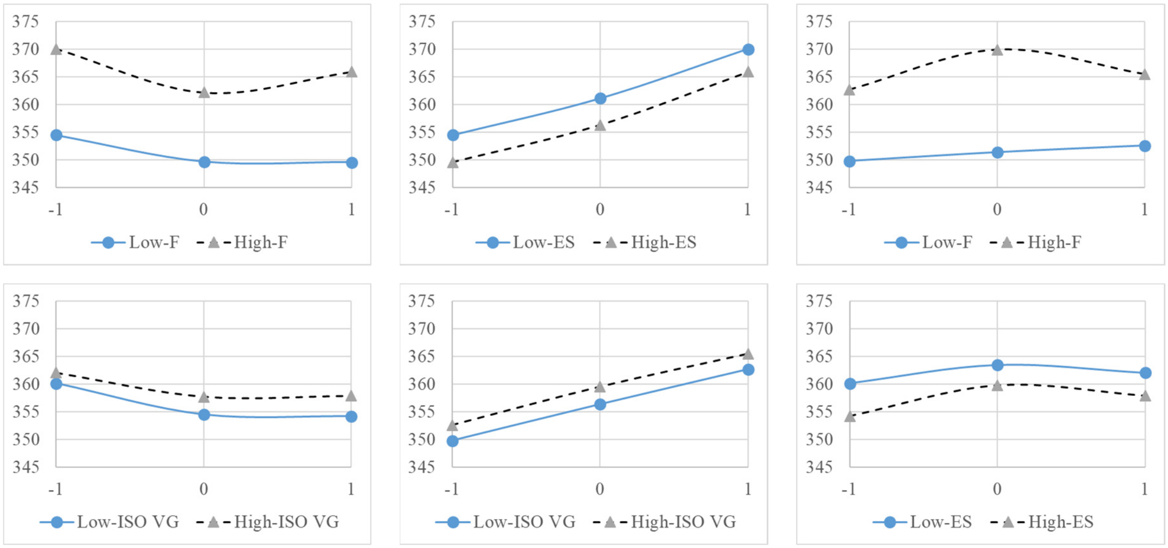

Figure 3.14 MT (measured in˚K)- Interaction plots for the TEHL, TTEHL and TTEHL-TB modeling conditions

Table 3.6 Factor main and interaction effects on MT (measured in˚K)

Effects	TEHL	TTEHL	TTEHL-TB
F	*11.99711*	*13.60256*	*14.78778*
ISO VG	*1.83367*	*5.04144*	*2.90656*
ES	*-4.18822*	*-1.63444*	*-4.61456*
F-ES	*-0.71000*	*1.66200*	*0.39817*
ES-ISO VG	*0.58433*	*1.46083*	*0.90350*
ISO VG-F	*-0.36250*	*-0.32733*	*-0.03000*
F-ES-ISO VG	*-0.25350*	*-0.00125*	*0.31050*

ES	*F*	*ISO VG*
a) TEHL		
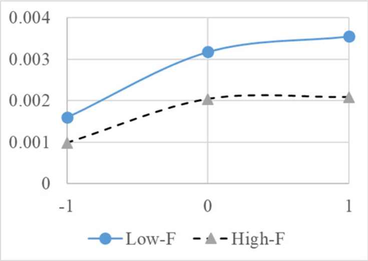	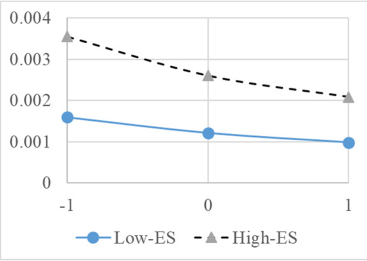	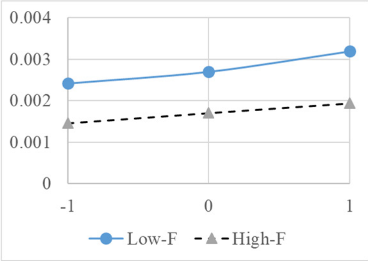
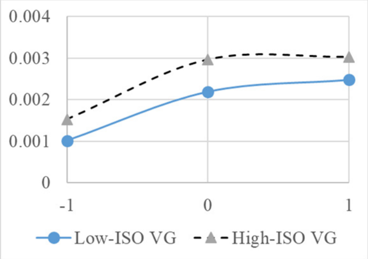	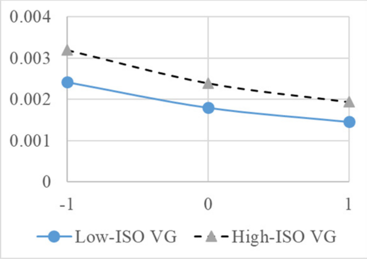	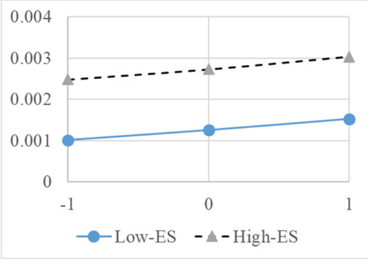
b) TTEHL		
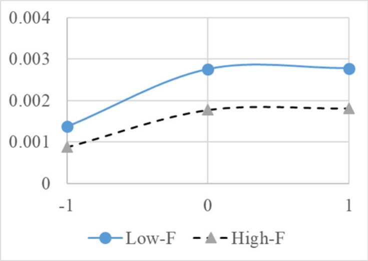	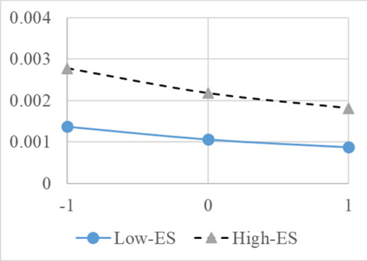	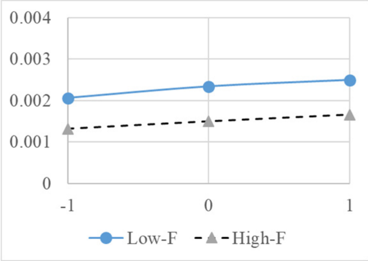
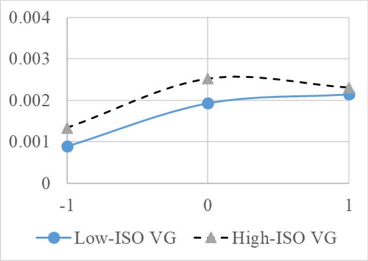	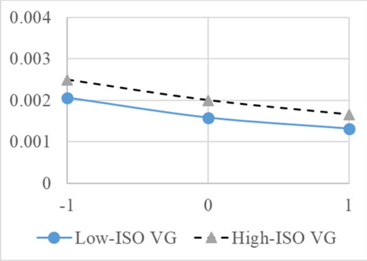	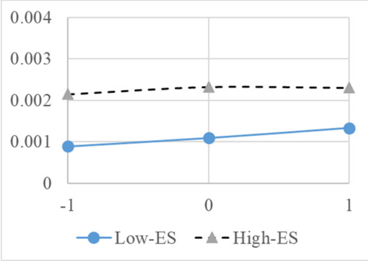

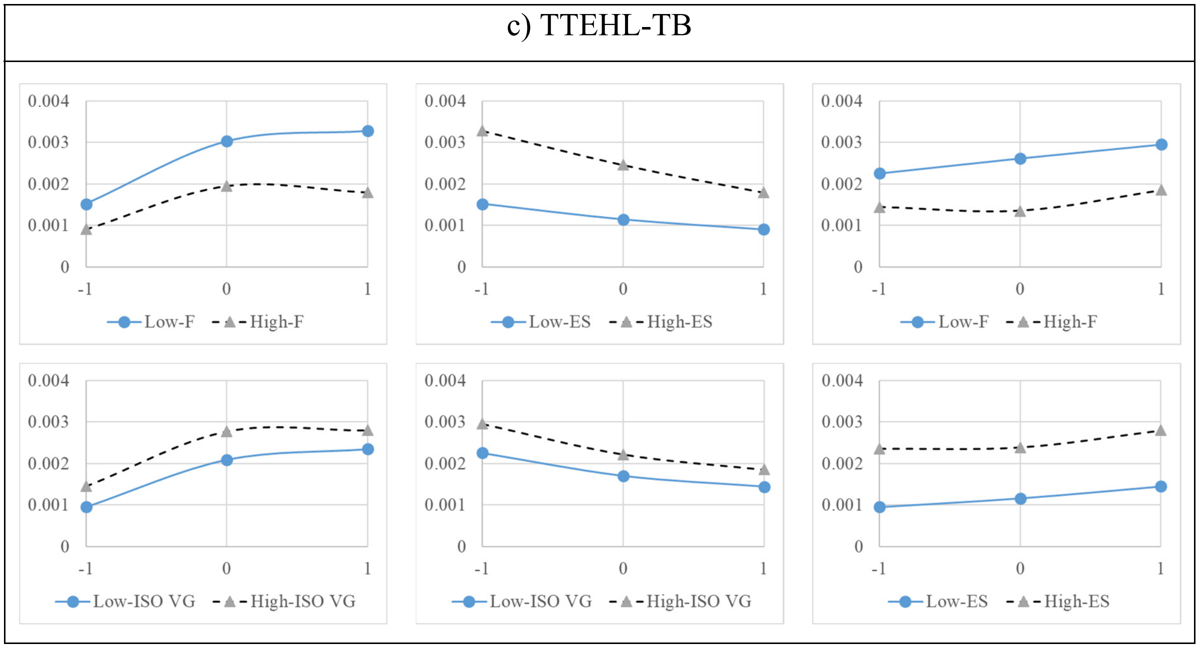
c) TTEHL-TB

Figure 3.15 MF- Interaction plots for the TEHL, TTEHL and TTEHL-TB modeling conditions

Table 3.7 Factor main and interaction effects on MF

Effects	TEHL	TTEHL	TTEHL-TB
F	*-0.00107*	*-0.00082*	*-0.00106*
ISO VG	*0.00062*	*0.00040*	*0.00054*
ES	*0.00148*	*0.00115*	*0.00132*
F-ES	*-0.00043*	*-0.00023*	*-0.00044*
ES-ISO VG	*0.00002*	*-0.00014*	*-0.00002*
ISO VG-F	*-0.00015*	*-0.00005*	*-0.00015*
F-ES-ISO VG	*-0.00002*	*0.00008*	*-0.00003*

Figure 3.13-a and the first column of Table 3.5 show, for the TEHL modeling condition, that *ES* and *F* have opposite effects on *MP*, while the *ISO VG* factor demonstrates a lower influence. The results manifest the clear influence of *F*: *MP* goes up with a load augmentation, and vice

versa. Figure 3.14-a and Figure 3.15-a completed in parallel with the first columns of Table 3.6 and Table 3.7 show the influence of *F* on *MT* and *MF*, respectively. An increase in *F* causes a temperature rise and a film thinning. These first observations are in agreement with common knowledge in lubrication. On the other hand, while, as expected, increasing *ISO VG* engenders a film thickening (Table 3.7) and a temperature rise (Table 3.6) due to shear dissipation, an increased impact of viscosity on *MP* is less obvious. The main effect of *ISO VG* in Table 3.5 shows that it globally tends to have a reducing action on *MP*. However, the plots in Figure 3.13-a suggest that the real impact of *ISO VG* is affected by the other factors. The interaction effects in Table 3.5 confirm this observation. The impacts of the *ES* factor are similar; unsurprisingly, an increase in this factor results in a film thickening (Figure 3.15-a and Table 3.7), and in a temperature reduction (Figure 3.14-a and Table 3.6) caused by the associated lubricant flow intensification, whereas its influence on *MP* is somewhat puzzling. The model predictions show that an increase in *ES* tends to lower the pressure, while Table 3.5 indicates that the interaction effects with the other factors are not dominant.

Altogether, despite light interactions between the factors, the results in Table 3.5 clearly indicate that increasing *F* in TEHL simulations engenders pressure increases, even though the two other factors may tend to lower the rise. On the other hand, the interaction effects presented in Table 3.6 and Table 3.7 indicate that the overall influence of *F* on the lubricant film temperature and thickness is more significantly affected by the two other factors.

When compared with the TEHL condition, Figure 3.13-b and the second column of Table 3.5 associated with the TTEHL modeling assumption indicate that including the thermoelastic deformations strongly modifies the system response. *MP* demonstrates a significant overall increase (30.5%); unrestricted heat flow at the free boundaries concentrates the thermoelastic deformations of the bodies far from their limits, and thus, tends to localize the pressure close to the center of the distribution. The simulations under a TTEHL assumption also substantially affect *MT* and *MF*. Compared to the TEHL predictions, *MT* shows an overall increase of 8.0 °K. (Figure 3.14-b), while *MF* displays a global reduction of 14.2% (Figure 3.15-b). Moreover, comparing the TTEHL results in Table 3.5 to the TEHL column reveals that the main effects of all three factors on *MP* are inverted. Conversely, the same comparison made in Table 3.6 and Table 3.7 shows evaluations of the main effects on *MT* and *MF* indicative of tendencies similar to those obtained under a TEHL assumption. For instance, since the heat generation is proportional to the pressure, increasing the load *F* causes a temperature augmentation (Table 3.6, second column), leading to a reduction of the lubricant viscosity in the maximum pressure zone, which in turn lessens the pressure localization (Table 3.5, second column). This viscosity decrease simultaneously favours a lubricant film thinning (Table 3.7, second column). On the other hand, the factors *ISO VG* and *ES* have more global effects: increasing *ISO VG* causes a distributed heat generation augmentation and a consistent temperature rise (Table 3.6, second column), leading to a viscosity reduction. The diffused nature of the viscosity adaptation does not significantly modify the shape of the thermoelastic deformation distribution, and thus does not alter the *MP* amplification brought in by the TTEHL assumption. An *ES* increase, which is equivalent to a lubricant flow increase, causes a temperature reduction (Table 3.6, second column) and a corresponding viscosity boost, which has consequences similar to an *ISO VG* augmentation. Although both the *ISO VG* and *ES* factors favour a lubricant film thickening (Table 3.7, second column), the distributed character of the viscosity changes prevents any drastic modification of the thermoelastic deformation distribution shape associated with a TTEHL modeling assumption.

Figure 3.13-c and the third column of Table 3.5 portray the *MP* response obtained when considering the TTEHL -TB modeling condition. The Figure 3.13-c plots show trends more akin to those obtained under the TEHL assumption (Figure 3.13-a). Nevertheless, *MP* still shows a global rise of 8.9%, when compared to the TEHL predictions; the controlled heat flow at the boundaries attenuates the pressure concentration engendered by the body thermoelastic deformations. The adiabatic conditions imposed at the body boundaries also reduce the overall *MT* increase from 8.04°K, for the TTEHL assumption, to 1.7°K, on average (Figure 3.14-c), while they lessen the *MF* reduction from the 14.2% observed before to an overall drop of less than 6.7% (Figure 3.15-c). Since the considered adiabatic condition is more forceful than real running conditions, it should be assumed that these error evaluations correspond to the lower bound of the actual imprecision associated with TEHL model predictions.

Specifically, the results obtained considering a TTEHL-TB condition show that, increases of *F* still reduce the lubricant film thickness (Table 3.7, third column) and push up the lubricant temperature (Table 3.6, third column). However, the temperature elevations are distributed more uniformly and remain lower than those associated with the TTEHL assumption. Hence, their influence is not strong enough to engender drastic changes of the pressure distribution shape. While this influence is still greater far from the boundaries, the thermoelastic deformations of the surfaces extend up to the body ends. Therefore, contrary to the TTEHL condition, imposing controlled heat flow at the body boundaries enables *F* increases to intensify *MP* (Table 3.5, third column). The TTEHL-TB assumption also sustains the diffused nature of the *ISO VG* and *ES* influence, which were described above for the TTEHL modeling condition. Accordingly, augmenting *ISO VG* still increases *MF* (Table 3.7, third column) and causes distributed heat generation increases associated with coherent temperature rises (Table 3.6, third column), while *ES* increases still lead to lubrication film thickening (Table 3.7, third column) and provoke temperature reductions (Table 3.6, third column), boosting the viscosity.

In summary, the results presented in the third columns of Table 3.5, Table 3.6 and Table 3.7 demonstrate that the load factor *F* has a dominant influence on *MP*, the pressure parameter, and on *MT*, the temperature parameter, and while both the viscosity *ISO VG* and the entraining speed *ES* factors also demonstrate a clear influence on *MT*, they only marginally affect *MP*. In fact, since *ES* determines the lubricant flow, which controls the volume of lubricant trapped in-between the surfaces and its temperature, and as a direct consequence, its viscosity, the results show that the factor influence on *MT* is greater than that of *ISO VG*. For the same reason, *ES* has a greater impact on *MF* than do *F* and *ISO VG*.

Finally, while the TTEHL assumption, which admits a maximum heat flow at the free boundaries, should be considered as a theoretical and over-simplified modeling approach, at the other end of the spectrum, the TTEHL-TB condition provides conservative evaluations of the intrinsic imprecision of TEHL simulations.

3.10 Conclusion

The first part of this paper implements the heat-affected zone definition proposed by Barber (Barber, 1971) to present thermoelastic influence factors, and enable contact models based on SAM. The goal here is to predict the impacts of thermoelastic deformations. Next, the study develops a modeling approach to include the influence of thermal boundary conditions on problems defined by a contact area delimited by free surfaces. This method introduces mirror heat patches to control the heat flows crossing the free boundaries. The investigation also examines the influence of the thermoelastic stress distributions generated on the free surfaces during the procedure. The study thus proposes a method to release the free surfaces from these stresses. The analysis demonstrates that the thermoelastic stresses have no substantial influence on the final results, and that they may simply be ignored.

The study also compares the predictions obtained from the proposed method to evaluations produced by finite element simulations. This validation demonstrates that the method developed to incorporate the thermoelastic deformations into the modeling of contacts between bodies of finite dimensions provides very accurate descriptions, while significantly reducing the computation burden. Indeed, for the considered problems and equivalent precision levels, when compared to FEA, the proposed method reduced the calculation times by more than 98%.

The second part of the paper introduces the thermoelasticity effects into thermal-elastohydrodynamic lubrication or TEHL modeling of line contact problems. The analysis shows that, when compared to TEHL simulations, the inclusion of thermoelastic deformations changes the pressure profile, and particularly, tends to localize the pressure close to the center of the distribution. The considered factorial design analysis exposes the imprecision level introduced by the TEHL simplification when applied to systems involving heat generation. This analysis assumes that the free boundaries were all under an adiabatic condition. Since this assumption is more restrictive than real operating conditions, the predicted effects of the finite dimensions of the bodies essentially correspond to attenuated impacts. Specifically, the appraisals presented describe lower bounds of the actual imprecision associated with TEHL model predictions. While the deviation from the maximum pressure prediction is larger, the calculation of the film thickness is also significantly affected, whereas the error on the temperature remains low. The configurations examined showed overall increases in the maximum pressure of around 9%, an overall decrease in the film thickness close to 7%, and an overall temperature increase of about 2°K.

CHAPTER 4

A SYSTEMATIC SOLUTION BASED ON THE HALF-SPACE CONCEPT FOR MODELING OF THERMOELASTIC CONTACT BETWEEN BODIES DEFINED BY CURVED FREE BOUNDARIES

Ali Yalpanian[a], Raynald Guilbault[b],

[a,b] Department of Mechanical Engineering, École de technologie supérieure, Université du Québec, 1100 Notre-Dame West, Montreal, Quebec, Canada H3C 1K3

Paper submitted for publication, June 2021

4.1 Abstract

This paper develops a modeling approach for simulation of thermal contacts delimited by curvilinear edges. The study introduces a correction for semi-analytical methods based on the half-space assumption to account for thermal boundary conditions. The approach establishes a correction radius to control the heat flux and adjusts the corrective heat load to handle the thermoelastic normal stress on free surfaces. Compared to Finite element analysis (FEA), the displacement calculated with the approach demonstrates a 99% improvement. A comparison of the complete thermal modification and normal stress elimination with FEA for a thermal contact shows more than 73% improvement, leading to an error margin of under 5%. The calculation burden is also drastically reduced as compared to that of a FEA.

Keywords: Contacts, Numerical simulation, Thermoelastic analysis

4.2 Introduction and literature review

This paper develops an efficient numerical approach to incorporate the influence of curvilinear free boundaries in thermoelastic contact simulations built on the half-space concept. Here, *thermoelastic* refers to the stress-strain response of a solid to a heat source, while *elastic* refers to the elastic stress-strain response of a solid submitted to a pressure. The study considers an aspect which is typical of numerous thermal contacts problems. The following are few examples: elastohydrodynamic contacts involving textured surfaces (D.B. Hamilton, 1966 ; Erdemir, 2005 ; Gropper et al., 2016 ; Manser et al., 2019 ; Siripuram & Stephens, 2004 ; Wakuda et al., 2003), contacts generated during rotational friction welding (Jl et al., 1991 ; W. Li et al., 2016 ; Lindemann et al., 2006 ; Reddy, 2015), and contacts between electrical connectors (Albers et al., 2011 ; Chin-Tu & Bryant, 1994 ; Williamson & Majumdar, 1992).

In reality, when examining simple contact problems not affected by heat, the classical Hertz theory (Hertz, 1896) results in precise evaluations. This theory involves three conditions: 1- a frictionless contact area; it also reckons that the contact zone is tiny as compared with 2- the body dimensions and 3- their curvature radii. Condition 1 imposes a clear restriction. On the other hand, conditions 2 and 3 enforce less evident simplifications; condition 2 excludes the potential effects of neighboring body limits, while condition 3 reduces the solids to half-spaces solely admitting elastic deformations.

Numerous modeling approaches have been developed over the years to examine contact problems contravening the Hertz restrictions (de Mul et al., 1986 ; Hartnett, 1980 ; S. Liu & Hua, 2009). Among these, the Hartnett (Hartnett, 1980) Semi-Analytical Method (SAM) certainly belongs to the most effective. This approach implements the Boussinesq half-space solution (Johnson K.L., 1985). However, in problems involving bodies limited by free boundaries, the half-space concept occasions shear and normal stresses on those limiting surfaces, and thus introduces a certain degree of imprecision close to the edges. Hetényi (Hetényi, 1960, 1970) and Keer (Hanson & Keer, 1995 ; Keer et al., 1983) developed precise solutions for the elimination of these stresses. However, the solutions are rather ponderous. Alternatively, the solution Guilbault (Guilbault, 2011) proposed provides a treatment that is almost as precise, while avoiding increasing the calculation burden. This technique eliminates the normal stress effects on the surface displacements through correction factors. Yalpanian and Guilbault (Yalpanian & Guilbault, 2020) presented a similar method to release curvilinear free surfaces from shear and normal stress distributions. Recently, they proposed a method to include the effects of thermoelasticity in models built on the half-space concept to describe contacts limited by planar free surfaces (Yalpanian & Guilbault, 2021).

The FEA option is also a well-recognized approach for solving non-Hertzian contact problems (Bachtar et al., 2006 ; Chatterjee & Sahoo, 2014 ; Sahoo & Ghosh, 2007 ; Yang & Komvopoulos, 2005). However, properly using FEA commercial software is not always simple, especially when it comes to the contribution of factors such as thermoelasticity (Gropper et al., 2016 ; Lindemann et al., 2006 ; Reddy, 2015). Nevertheless, most noteworthy is the fact that this option still often involves excessive mesh production costs and solution times. Alternatively, SAMs are less affected by these limitations, and thus represent an attractive option for modeling contact problems (Hanson & Keer, 1995 ; Hartnett, 1980 ; Hetényi, 1960, 1970 ; Keer et al., 1983 ; J. Li & Berger, 2003 ; Junshan Li & Berger, 2001). Indeed, since experimental investigations of contact problems carry considerable difficulties, the FEA avenue remains a highly helpful and widely accepted validation tool.

To the best of the authors' knowledge, presently, no SAM can properly handle thermoelastic contacts bordered by curved edges. Therefore, the present work introduces a half-space-based representation that encompasses thermoelastic displacements in thermal contacts bounded by curved free surfaces. The analysis involves two steps: the first integrates the thermal boundary condition at the free surfaces into the solution, while the second concentrates on eliminating the influence of the thermoelastic normal stresses introduced to the boundaries by the half-space hypothesis on the surface displacements. The adopted approach is analogous to the technique put forward in Ref. (Yalpanian & Guilbault, 2021) for straight boundaries. While for straight boundaries, the first step works with straight directions to control the heat flux crossing a given boundary and relate each contact area to a mirror position, with curved boundaries, the procedure considers radial directions instead. This method connects each contact area to a correlated locus external to the boundary, and thus leads to a relation that is valid for both external and internal cylindrical shape alternatives. Moreover, like the solution for straight boundaries, the second step adopts a corrective factor approach to counterbalance the impact of normal stress on the displacements of the half-space top surface.

Section 4.3 describes the fundament of the SAM avenue, after which some common mechanisms of heat generation in contacts are briefly introduced. The next sections develop the thermal boundary simulation procedure and establish the thermoelastic normal stress influence elimination process. Each step of the solution development includes a validation comparing the prediction of the proposed method with results obtained from FEA.

4.3 Fundament of the half-space representation

Based on the Boussinesq half-space solution, the numerical method introduced by Hartnett (Hartnett, 1980) reduces a contact pair to two half-spaces supporting linear deformations. The half-space assumption provides a solution to determine the displacement of the surfaces submitted to a load. Accordingly, Eq. (4.1) establishes the normal displacement at any point (x, y) of the half-space surface induced by a pressure $P(\xi, \zeta)$ distributed on an area A of this surface:

$$w(x, y) = \frac{1 - v^2}{\pi E} \iint_{\mathrm{A}} \frac{P(\xi, \zeta)}{s} d\xi d\zeta \tag{4.1}$$

where w is the elastic surface displacement in the normal direction, E is the Young modulus, v corresponds to the Poisson ratio and $s = \sqrt{(x - \xi)^2 + (y - \zeta)^2}$.

The contact modeling procedure first defines the original distance (g) of the two solids a and b from the tangent plane along with their linear normal deformation (w_a, w_b). Eq. (4.2) expresses this relation. In Eq. (4.2) α represents the normal approach of the bodies. As explained in Ref. (Yalpanian & Guilbault, 2021), Eq. (4.2) also allows including the thermoelastic displacements (w_{TE}) of the half-space surfaces. Eq. (4.3) presents the resulting expression. Figure 4.1 illustrates the variables.

$$\begin{cases} w_a + w_b + g_a + g_b = \alpha & , P > 0 \\ w_a + w_b + g_a + g_b > \alpha & , P = 0 \end{cases} \tag{4.2}$$

$$\begin{cases} w_a + w_b - w_{TE_a} - w_{TE_b} + g_a + g_b = \alpha & , P > 0 \\ w_a + w_b - w_{TE_a} - w_{TE_b} + g_a + g_b > \alpha & , P = 0 \end{cases} \tag{4.3}$$

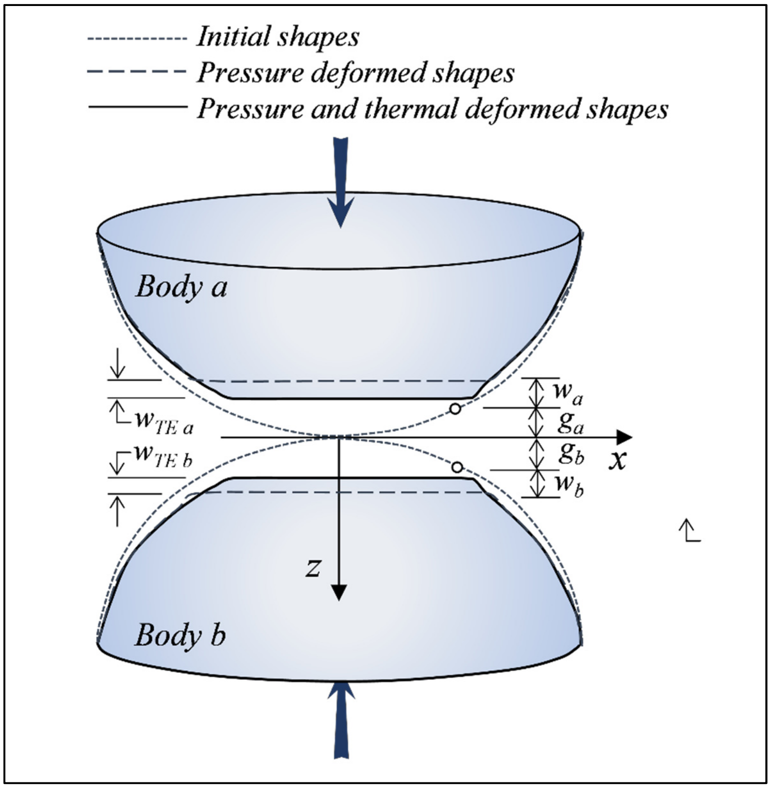

Figure 4.1 Contact model variables

The literature shows that a steady heat source applied on the surface of a half-space leads to infinite thermoelastic displacements of that surface (Yalpanian & Guilbault, 2021). Therefore, to allow modeling thermoelastic displacements of real bodies under steady state conditions, Barber (Barber, 1971) defined a heat affected zone radius (s_0). Figure 4.2 shows the s_0 definition and illustrates its role. Eq. (4.4) completes the description and gives the normal displacement w at a distance s smaller than s_0 from the heat source q.

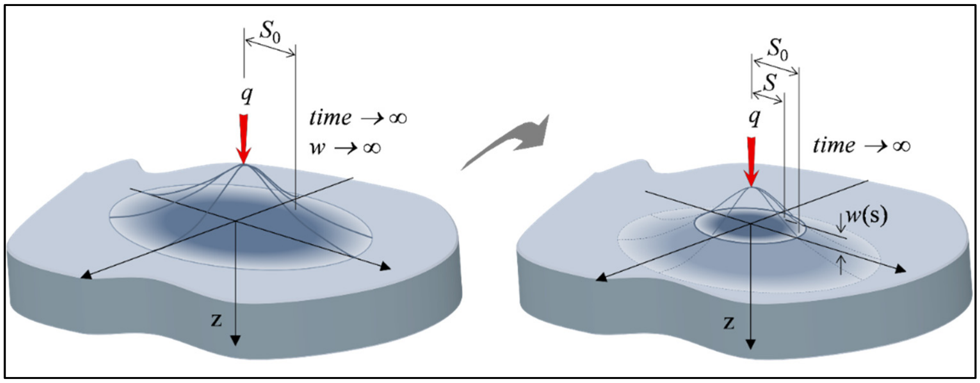

Figure 4.2 Steady state thermoelastic deformation

$$w_{TE} = \frac{q\gamma(1+\nu)}{2\pi k}\log\left(\frac{s_0}{s}\right) \tag{4.4}$$

where γ, k and ν are the coefficient of thermal expansion (°K^{-1}), the thermal conductivity (W/m °K) and the Poisson ratio of the half-space material, respectively.

Accordingly, when a uniform heat flux (q'') acts over a rectangular patch of area *A* and side lengths considerably smaller than s_0, integrating Eq. (4.4) over *A* gives the overall thermoelastic displacement w_{TE} brought in Eq. (4.3). Eq. (4.5) formulates the resulting relation (Yalpanian & Guilbault, 2021):

$$w_{TE} = \frac{\gamma(1+\nu)}{2\pi k}\left\{q''\left(\log(s_0)\iint_A dA - \iint_A \log(s)\, dA\right)\right\} \tag{4.5}$$

4.3.1 Half-space modelling approach for elastic deformation

The Hartnett's SAM divides the so-called blanket contact plane into rectangular contact cells of area *A* and lengths 2*a* and 2*b* along the *x*- and *y*-axes, respectively. Each cell *I* may support a uniform pressure (P_i). Now, assuming that the contact patches may also sustain a uniform heat flux (q''_I), Eq. (4.3) may be rewritten for a displaced rectangular cell *J*, centered at (*x, y*) with respect to the central point of the loaded patch *I* as:

$$\sum_I P_I \times f_{IJ} - \sum_I q''_I \times f_{TE_{IJ}} = \alpha - g_{a_J} - g_{b_J} \tag{4.6}$$

where f_{IJ} represents the influence factors calculated with Eq. (4.1) ($f_{IJ}(x,y) = \left(\frac{1-\nu_a{}^2}{\pi E_a} + \frac{1-\nu_b{}^2}{\pi E_b}\right)\iint_A \frac{1}{s} dA$) and $f_{TE_{IJ}}$ denotes the influence factors defined via Eq. (4.5) ($f_{TE_{IJ}}(x,y) = \left(\frac{\gamma_a(1+\nu_a{}^2)}{2\pi k_a} + \frac{\gamma_b(1+\nu_b{}^2)}{2\pi k_b}\right)\left\{\log(s_0)\iint_A dA - \iint_A \log(s)\ dA\right\}$). The final expression of $f_{TE_{IJ}}(x,y)$ was put forward in (Yalpanian & Guilbault, 2021). Eq. (4.7) gives this expression for one side of the contact pair. On the other hand, the final expression of $f_{IJ}(x,y)$ may be found in many references, such as in (Guilbault, 2011 ; Hartnett, 1980), for example. These influence factors depend on the constant material properties of the solids and the distance between each contact cell *I* and *J*. Hence, they can be calculated only once at the beginning of the numerical process.

$$\begin{aligned} f_{TE_{IJ}} = \frac{\gamma(1+\nu)}{2\pi k}\Bigg[&4\log(s_0)\,ab \\ &- \Bigg\{\left[x_U y_U(\log(x_U{}^2 + y_U{}^2) - 3) + x_U{}^2 tan^{-1}\left(\frac{x_U}{y_U}\right) + y_U{}^2 tan^{-1}\left(\frac{y_U}{x_U}\right)\right] \\ &- \left[x_L y_U(\log(x_L{}^2 + y_U{}^2) - 3) + x_L{}^2 tan^{-1}\left(\frac{x_L}{y_U}\right) + y_U{}^2 tan^{-1}\left(\frac{y_U}{x_L}\right)\right] \\ &- \left[x_U y_L(\log(x_U{}^2 + y_L{}^2) - 3) + x_U{}^2 tan^{-1}\left(\frac{x_U}{y_L}\right) + y_L{}^2 tan^{-1}\left(\frac{y_L}{x_U}\right)\right] \\ &+ \left[x_L y_L(\log(x_L{}^2 + y_L{}^2) - 3) + x_L{}^2 tan^{-1}\left(\frac{x_L}{y_L}\right) + y_L{}^2 tan^{-1}\left(\frac{y_L}{x_L}\right)\right]\Bigg\}\Bigg] \end{aligned} \tag{4.7}$$

Where L and U indices refer to the lower and upper positions, respectively. Hence, $x_L = x - a$, $x_U = x + a$, $y_L = y - b$ and $y_U = y + b$.

4.3.2 Half-space stress formulation

The half-space theory also formulates the elastic shear (τ_{xz}) and normal stresses (σ_x) at a point (x, y, z) of a half-space, when a point force *F* is situated at the origin on the surface (the inward *z*-axis is parallel to the surface normal),

$$\sigma_x = \frac{F}{2\pi}\left[\frac{(1-2\nu)}{d^2}\left\{\left(1-\frac{z}{c}\right)\frac{x^2-y^2}{d^2}+\frac{zy^2}{c^3}\right\}-\frac{3zx^2}{c^5}\right] \tag{4.8}$$

$$\tau_{xz} = -\frac{3F}{2\pi}\frac{xz^2}{c^5} \tag{4.9}$$

where $d = (x^2+y^2)^{\frac{1}{2}}$ and $c = (d^2+z^2)^{\frac{1}{2}}$.

In addition to the stresses induced by a surface pressure, a heat load (q (W)) acting on the half-space surface also generates thermoelastic stresses. These thermoelastic stresses are planar ($\tau_{xz_{te}} = 0$) (Sternberg & Mcdowell, 1957), and may thus be expressed by Eq. (4.10) (Mark Kachanov, Boris Shafiro, 2003):

$$\sigma_{x_{TE}} = -\frac{qG\gamma}{4\pi k}(1+\nu)\left[\frac{1}{z+\sqrt{x^2+z^2}}\right] \tag{4.10}$$

In Eq. (4.10), *G* is the shear modulus, γ is the coefficient of thermal expansion, *k* is the thermal conductivity and ν is the Poisson ratio.

4.4 Heat generation

Although the thermal aspect is usually ignored in contact modeling, real contact configurations often involve some heat generation. Moreover, a large proportion of the heat generated in contact dissipates through the solids and induces thermoelastic deformations which modify the contact conditions. In contact modeling, thermoelastic displacements may be regarded as unidirectional and progressing normal to the contact surface. Most often, the heat generation in dynamic contacts results from dry friction or from lubricant shearing (Balci et al., 2015 ; Sukumaran et al., 2018). On the other hand, in static contacts, it is often an electrical resistance at the surface junction between two bodies that provokes a heat dissipation (Bahrami et al., 2005 ; M. G. Cooper, B. B. Mikic, 1969 ; Mikic, 1974). The present analysis simply assumes that a heat source affects the contact pair and overlooks the heat generation process.

4.5 Thermal boundary

SAMs based on the half-space assumption implicitly lead to significant deviations of the pressure evaluations close to body ends. As already mentioned, under pure pressure loadings, the origin of these deviations is the artificial restraint of the free surfaces prompted by the internal stress distributions (shear and normal) inherent to the assumption (Figure 4.3-a). On the other hand, when including a heat source, both the thermoelastic displacement controlled by the heat flow at the free surfaces and the thermoelastic normal stress distributions produced on the same free surfaces contribute to the deviation (Figure 4.3-b) (Yalpanian & Guilbault, 2021).

The elimination of the thermoelastic normal stress distributions poses no real problem, since strategies such as the one developed in (Yalpanian & Guilbault, 2020) for the elastic problem with curved free surfaces may be adapted to this thermoelastic consideration. In contrast, the internal heat, which must also be harmonized with the free curved boundary presence, necessitates the preparation of a specific procedure.

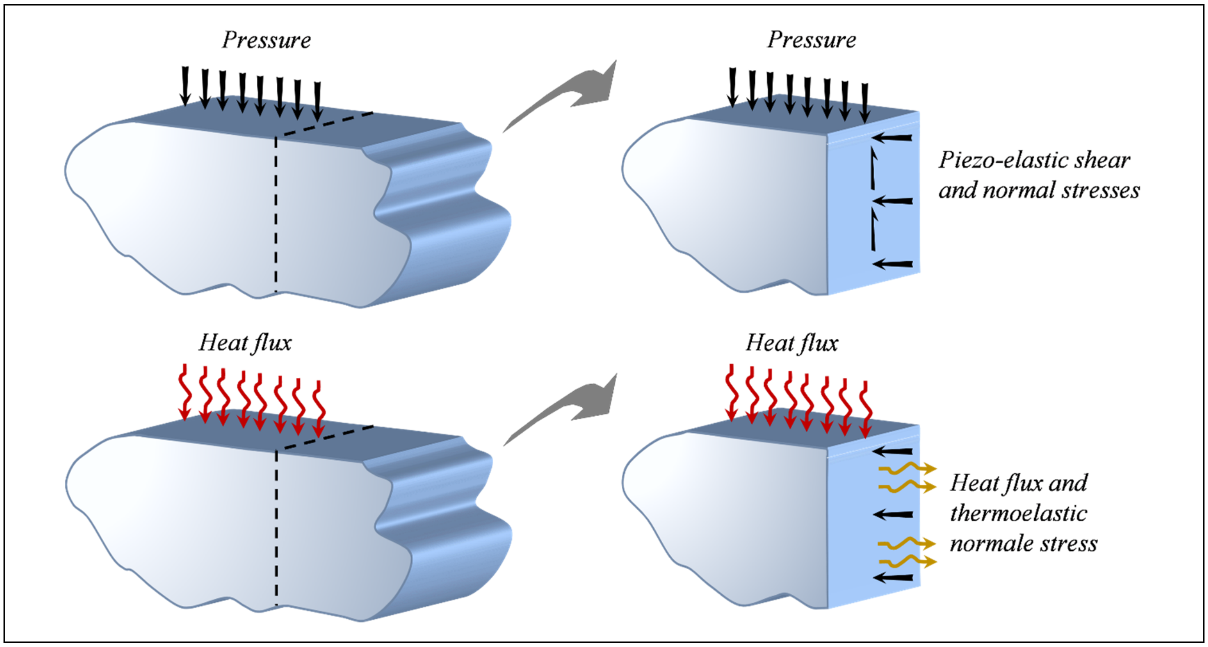

Figure 4.3 Consequences of half-space hypothesis on free edges

The adiabatic boundary is the easiest boundary condition to model. Moreover, an adiabatic simplification may virtually parallel numerous real conditions. Nevertheless, for many free surfaces where a convective heat transfer is dominant, the adiabatic assumption is not valid. Interestingly, however, as suggested in (Yalpanian & Guilbault, 2021), simple adjustments of the position of the correction heat loads allow converting the adiabatic condition into a wide range of convective boundary conditions. Therefore, the first step of the modeling procedure development focuses on the adiabatic boundary condition. It establishes the position of correction heat loads required to transform the condition of a curved free surface from unconstrained heat flux to adiabatic.

Eq. (4.11) formulates the heat flux q''_x (W/m^2) generated in an arbitrary x direction at an internal point (x,y,z) of a half-space, when a steady state heat load q (W) acts over a surface element (ΔA) of this half-space. This formulation refers to a local coordinate system located at the heat load position with axis z oriented inward (Yalpanian & Guilbault, 2021). Thus, Eq. (4.11) allows determining the heat flux crossing a surface selected at the position of a body boundary.

$$q''_x = -\frac{q}{4\pi}\left(\frac{x}{(x^2+y^2+z^2)^{3/2}}\right) \tag{4.11}$$

In contrast with the planar surface condition, adding an identical mirror heat load at an equal distance from the edge along the direction normal to the free surface does not guarantee a precise correction of the heat flux crossing a curved free boundary. In reality, to establish an adiabatic condition and cancel out the boundary crossing heat flux, the mirror heat load generates a counterbalance heat flux distribution of the same resultant amplitude and centroid. Therefore, to produce the same effect on curved free boundaries, the adopted strategy must first determine the resultant of the heat flux distribution as well as its line of action, and then determine the radial position and amplitude of a corrective heat load producing an opposing heat flux distribution.

4.5.1 Heat flux at the free surface

To define corrective heat loads, the resultant amplitude and the line of action of the heat flux induced by a heat load distributed over an arc must be defined along the radial inward and outward directions. The required integral along direction z (normal direction) is analytical, whereas the integral along the heated arc (tangential coordinate θ) is obtained from a numerical procedure. Section 2.5.2 presents all the details. Figure 4.4 displays the parameters required for the process, with R representing the free surface radius, and where r_i denotes the radius of the heat loaded arc, and r_o denotes the radius of the arc supporting the correction heat load canceling out the heat flux crossing the free surface.

Although the following portrayal describes a cylindrical solid of radius R, the process is also valid for a cylindrical hole of the same radius. The following subsections define the half-space internal heat flux generated at a radius R in the outward direction by a heat load $\hat{Q}_{r_i}$ (W/m) distributed over an arc of radius r_i and in the inward direction by a heat load $\hat{Q}_{r_o}$ (W/m) distributed over an arc of radius r_o. All the definitions here refer to the cylindrical coordinate system (r, θ, z) displayed in Figure 4.4.

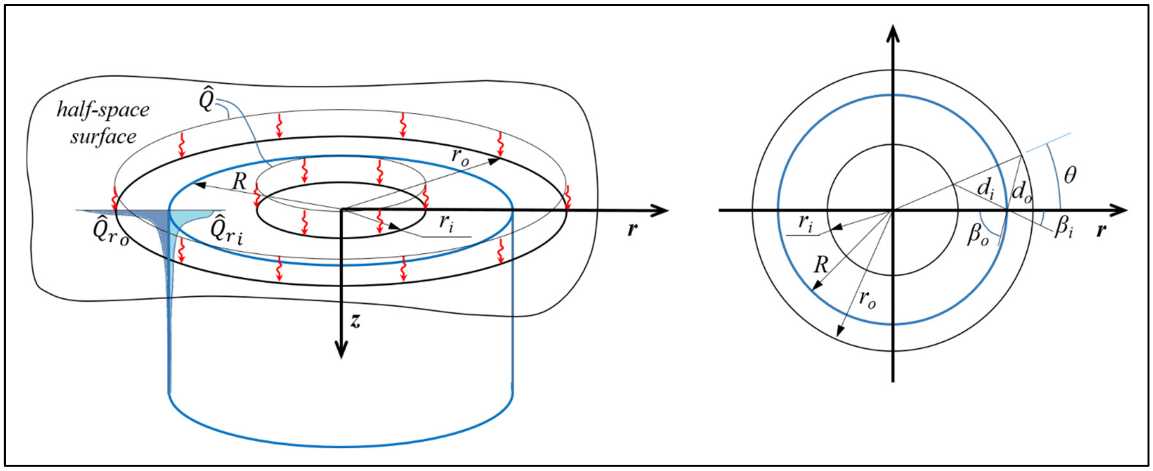

Figure 4.4 Parameters for a cylindrical solid

The equation developments presented below includes the following variable definitions:

${c_{i,o}}^2 = {d_{i,o}}^2 + z^2$ is the distance between a chosen point *Li* at (r_i, β_i, 0) on the loaded ring r_i or *Lo* at (r_o, β_o, 0) on the loaded ring r_o and the location (*R*, 0, *z*) of the heat flux calculation. The variables *di* and *do* are the surface distances between *Li* or *Lo* and the point (*R*, 0, 0), respectively, while β_i and β_o are the related angles shown in Figure 4.4. The next parameters describe dimensionless variables:

$$n_i = \frac{r_i}{R}, n_o = \frac{R}{r_o}, \bar{z} = \frac{z}{R}, \overline{q''}_r = \frac{\pi R q''_r}{\hat{Q}}$$

Where q''_r is the radial heat flux defined by Eq. (4.11) when $x^2 + y^2$ is replaced by r^2 and θ is set to 0, and $\hat{Q}$ is the heat load distributed over the considered arc. Therefore, if $Q = \hat{Q}_{ri,o} r_{i,o} d\theta$ is the total heat load (in W) over the considered arc, Eq. (4.12) rewrites Eq. (4.11) and gives the radial heat flux at the location (*R*, *0*, *z*) prompted by a distributed heat load over a given arc on the surface half-space:

$$q''_r|_{\theta=0} = -\frac{Q}{4\pi}\left(\frac{d_{i,o}\cos(\beta_{i,o})}{{c_{i,o}}^3}\right) \tag{4.12}$$

Integrating the heat flux given by Eq. (4.12) over the heat loaded arc $[-\varphi, \varphi]$, Eq. (4.13) and Eq. (4.14) give the dimensionless heat flux distribution $\overline{q''}_{r_{i,o}}$ generated along the vertical axis *z* at $\theta = 0$ on a surface defined by a radius *R* when a heat load is distributed on the top surface of a half-space over an arc of angle $[0, \varphi]$ and radius r_i or r_o, respectively (see Figure 4.4). The limit angle φ will be considered in more details later.

$$\overline{q''}_{r_i} = -\int_{-\varphi}^{\varphi} \frac{1 - n_i\, cos(\theta)}{\left({n_i}^2 + 1 - 2\, n_i\, cos(\theta)\right)} d\theta \tag{4.13}$$

$$\overline{q''}_{r_o} = -n_o \int_{-\varphi}^{\varphi} \frac{cos(\theta) - n_o}{\left(1 + {n_o}^2 - 2\, n_o\, cos(\theta)\right)} d\theta \tag{4.14}$$

Figure 4.5-a shows the $\overline{q''}_{r_i}$ distributions calculated for five n_i ratios along $\bar{z}$, while Figure 4.5-b presents the corresponding $\overline{q''}_{r_o}$ distributions established for n_o values matching the selected

n_i ratios. A visual inspection of these two plots reveals that the corresponding curves display different behaviors. Therefore, since the ultimate objective is to superimpose opposite heat flux, Figure 4.5-c shows the $\overline{q''}_{r_o}$ distributions better opposing the heat flux of Figure 4.5-a. In fact, the curves in Figure 4.5-c do not display perfectly opposed distributions, but distributions solely offering commensurate resultants. These curves stem from five n_o ratios not equal to the n_i values considered in Figure 4.5-a. Section 2.5.2 will examine the underlying relationship more thoroughly.

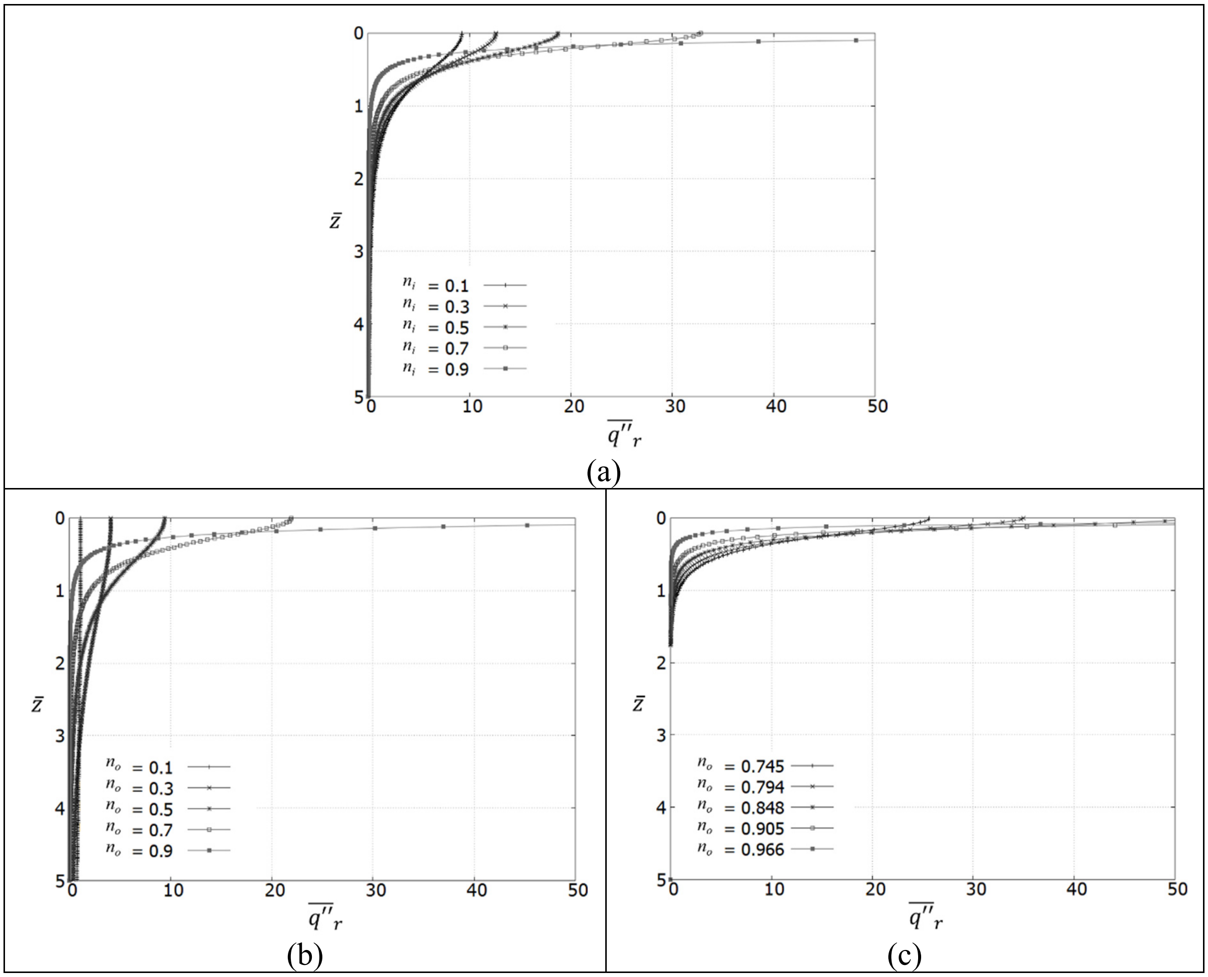

(a)

(b)

(c)

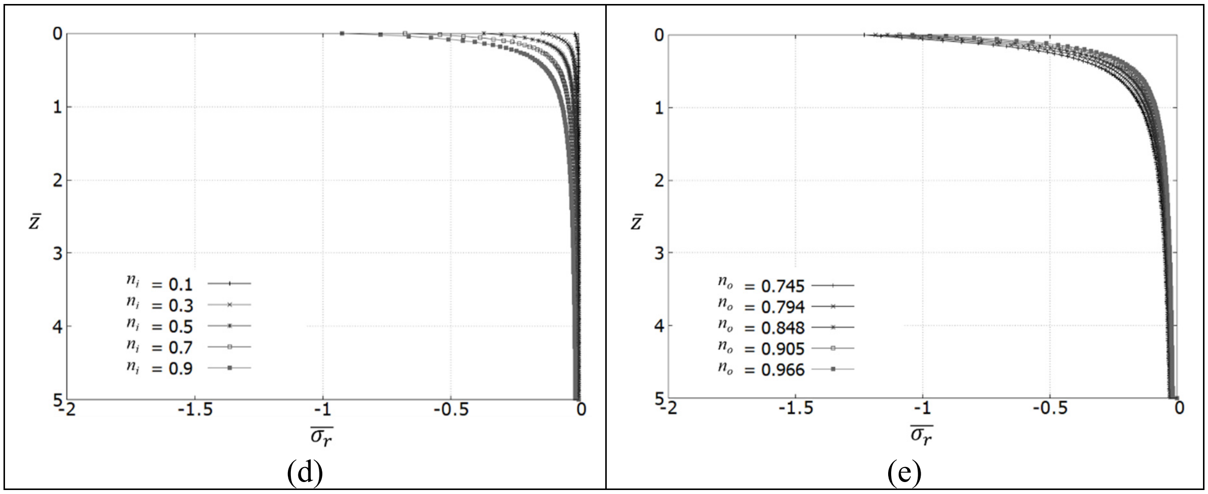

(d) (e)

Figure 4.5 Dimensionless heat flux distributions over a surface of radius R produced by a heat load acting (a) on an arc r_i, (b) on an arc r_o, (c) on an arc r_o selected to produce a heat flux equivalent to the heat distributions in (a); (d) and (e) dimensionless thermoelastic normal stress prompted over a surface of radius R by a heat load distributed (d) on an arc r_i, and (e) on an arc r_o defined by Eq. (2.12)

The heat flux elimination procedure searches for a heat flux resultant (Φ_z) equivalent to the resultant amplitude of the heat flux induced on a surface of radius R by a distributed heat load on the top surface of a half-space. Eq. (4.15) establishes the resultant amplitude of the heat flux Φ_{z_i} from an integration of Eq. (4.12) along $z \in [0,\infty[$ and over an arc of radius r_i when θ is assumed to be $[-\varphi, \varphi]$. Eq. (4.16) presents the corresponding relation Φ_{z_o} defined for an arc load of radius r_o when also assuming the following integration intervals $\theta \in [-\varphi, \varphi]$ and $z \in [0,\infty[$.

$$\Phi_{z_i} = \int_{-\varphi}^{\varphi}\int_{0}^{\infty} q''_r \, dz \, d\theta \bigg|_{r_i} = -\frac{\hat{Q}}{\pi R}\int_{-\pi}^{\pi}\int_{0}^{\infty} \frac{1 - n_i \cos(\theta)}{\left(n_i^2 + 1 - 2\, n_i \cos(\theta) + \bar{z}^2\right)^{3/2}} \, dz \, d\theta \qquad (4.15)$$

$$\Phi_{z_o} = \int_{-\varphi}^{\varphi} \int_{0}^{\infty} q''_r \, dz \, d\theta \Bigg|_{r_O} = -\frac{\hat{Q} n_o}{\pi R} \int_{-\pi}^{\pi} \int_{0}^{\infty} \frac{n_o - cos(\theta)}{\left(1 + n_o{}^2 - 2\, n_o \, cos(\theta) + (n_o \bar{z})^2\right)^{3/2}} dz \, d\theta \qquad (4.16)$$

4.5.2 Heat flux elimination process

To eliminate the heat flow generated across a surface of radius *R* by an arc heat load of radius *ri*, a counteracting exterior heat load imposed on a *ro* arc with equal limits ($\pm\varphi$) should generate a congruous heat flux resultant ($\Phi_{z_i} = \Phi_{z_O}$). The role of this counterbalancing heat load distribution is equivalent to that of a mirror heat load used to free a straight boundary.

A concentrated heat source moved along an arc of radius *ri* smaller than *R* generates a heat flux at the position (*R,0, z*) exclusively in the outward direction. Then again, the same experience along an arc of radius *ro* larger than *R* induces heat flux alternating from the outward to the inward directions. Therefore, to cancel out a heat flux caused by a heat load active at a radius *ri*, the length of the corrective arc must match the portion of the circle of radius *ro* causing a heat flux in the inward direction. This prerequisite defines the appropriate angle φ. Figure 4.6 shows the analyzed portion of arc *ri* and the associated section of arc *ro*.

A first inspection of the plots in Figure 4.5 suggests that although generating a proportionate heat flux resultant may be simple, producing an equivalent heat flux distribution could be much more challenging. Accordingly, the proposed procedure only searches for a heat flux resultant equilibrium. Eq. (4.17) formulates the equilibrium $\Phi_{z_i} = \Phi_{z_O}$ (from Eqs. (4.15) and (4.16)). Besides, since Eq. (4.17) has no closed form solution, an adapted numerical method is required to evaluate the solution. The numerical calculation supposes that a depth *z=10R* corresponds to infinity.

$$\int_{-\varphi}^{\varphi} \frac{1-\ n_i\, cos(\theta)}{\left(n_i{}^2+1-2\, n_i\, cos(\theta)\right)} d\theta = n_o \int_{-\varphi}^{\varphi} \frac{cos(\theta)-n_o}{\left(1+n_o{}^2-2\, n_o\, cos(\theta)\right)} d\theta \qquad (\ 4.17\ )$$

For a heat load distributed over an arc defined by a radius r_i, Eq. (4.17) rapidly indicates that the calculation of the counteracting distributed heat load over the r_o arc necessitates the specification of the two parameters r_i and φ. Indeed, this limit angle φ also hinges on r_o, and furthermore, parameter r_o must also be defined during the process. Thus, to determine r_o and φ, the procedure involves iterative calculations. The procedure also assumes that the limit angle φ is the same for the two arcs sustaining the heat loads (interior r_i and exterior r_o).

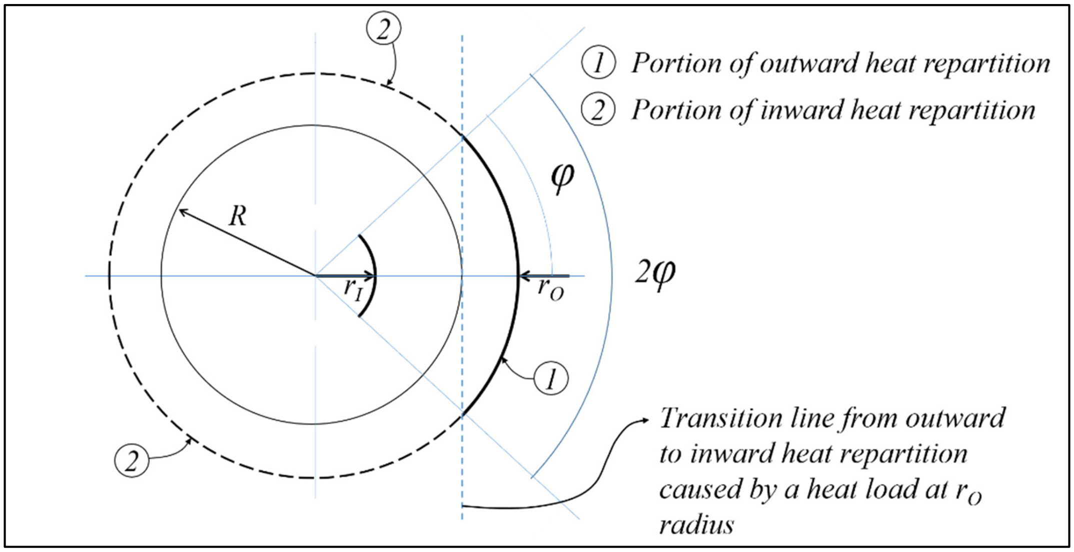

Figure 4.6 Arc limit for heat flux calculation

4.5.2.1 Numerical evaluation of r_o

Parameters n_i and n_o are, by definition, included within the [0-1] range. Therefore, the two sides of Eq. (4.17) may be combined in a graph with a single scale. Figure 4.7 shows the two sides of Eq. (4.17) (*LS* being the left-hand side and *RS* the right-hand side). Then, n_o is established using the graphical solution illustrated in Figure 4.7. This solution strategy is described as follows: 1- for any selected n_i locus, the left-hand side (*LS*) of Eq. (4.17) is calculated numerically; 2- next the *LS* value is assigned to *RS* to determine the related value of

n_o. Eq. (4.18) gives the expression offering the best fit to the results, and hence establishes the relationship between r_o and r_i.

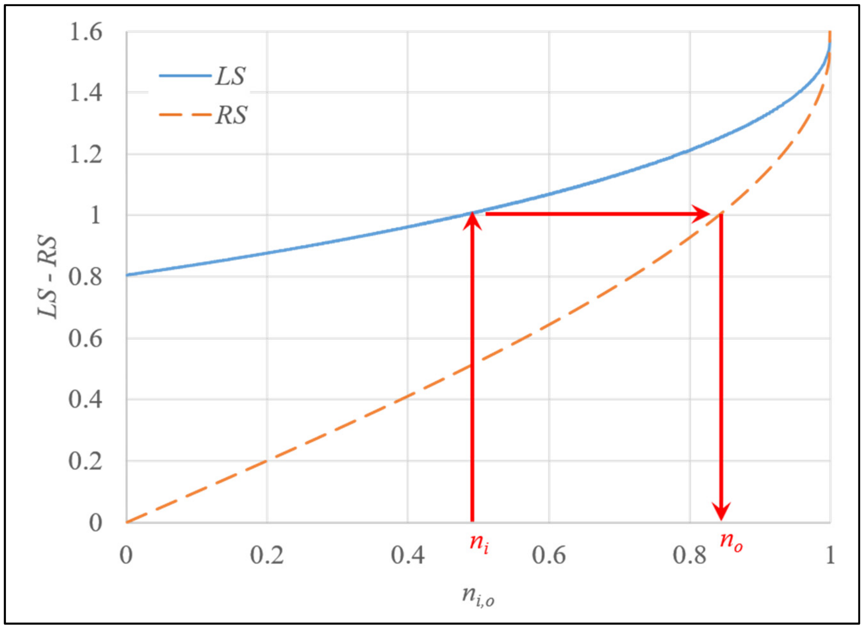

Figure 4.7 Eq. (2.11) solution strategy or n_i-n_o relation graph

$$n_o(n_i) = 0.0505\, n_i^{\,2} + 0.2285\, n_i + 0.7212 \qquad (4.18)$$

Eq. (4.18) allows mapping any heat loaded area located inside the free boundary onto an external counterbalance area. Figure 4.8 displays the external corrective area established for a rectangular patch of the contact zone. In reality, Eq. (4.18) defines a correspondent radius for any location of the initial patch. Therefore, mapping the contour of the initial patch results in a four-sided zone with curved edges. On the other hand, the Hartnett's SAM involves rectangular pressure cells (Hartnett, 1980). Hence, to simplify the procedure, the proposed strategy replaces the curvilinear four-sided zone with a rectangle preserving the surface area of the mapped zone. The substitute rectangle also preserves the aspect ratio of the original mapped patch.

The simplification may be pushed even further; in particular, it could be feasible to set the counterbalance patch area identical to that of the original loaded cell. Nevertheless, while easing the process, this avenue would reduce the modeling precision. Thus, to preserve the model accuracy, the present analysis does not consider this option.

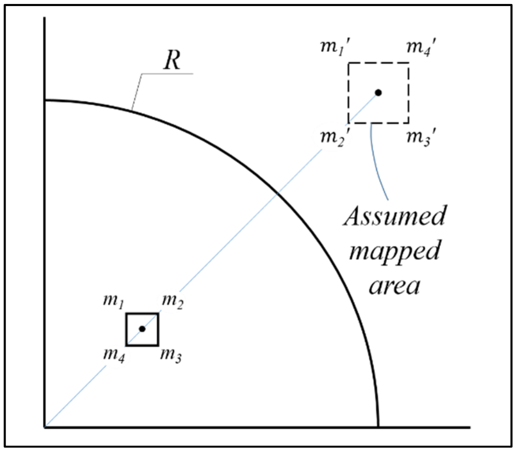

Figure 4.8 Contact cell and correction patch

4.5.3 Adiabatic boundary validation

The section examines the thermal model precision and validates the strategy put forward to describe an adiabatic boundary condition. Therefore, to isolate the adiabatic boundary condition influence and eliminate the repercussion of the thermoelastic normal stresses at the free surface, the procedure examines an axisymmetric structure made of a material presenting an orthotropic coefficient of thermal expansion in the axial direction z. This structure is submitted solely to a uniform heat load distributed over the contact surface. This validation step compares the model predictions to FEA results obtained for the same layout. Both the selected structure and the imposed heat load are symmetrical. Therefore, for this particular system, the FEA may be reduced to a 2D axisymmetric model. This simplified representation offers a better precision and a faster solution than a 3D model. Since the considered contact surface bears no pressure, the combination of the top uniform heat flux with the adiabatic boundary condition at the free surface results in a uniform temperature distribution, and thus, in consistent uniform thermoelastic displacements of the contact surface. Figure 4.9 illustrates the considered problem, where T is the temperature, T_0 is the imposed temperature at the lower boundary and T_H is the resulting temperature at the contact surface. Figure 4.9 also displays the temperature profile along *H*, the axial dimension of the structure. This profile is obviously axisymmetric.

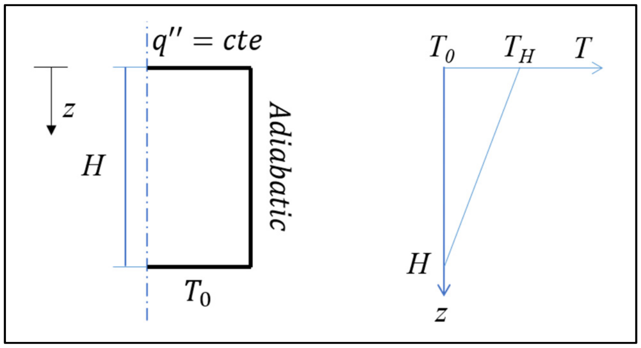

Figure 4.9 Temperature profile

As mentioned in Section 4.3 , the proposed method integrates the definition of a heat-affected zone radius (s_0). In order to cover the complete area and the additional surface involved during the mirroring procedure, the radius s_0 is set to 1.387R. This value was established based on an analysis similar to the one introduced when examining the graph in Figure 4.5-c. Hence, since the center of the circular contact surface belongs to the heat loaded zone, the smallest possible value for n_i is zero. On the other side, the n_o ratio generating an opposed heat flux with an equal resultant amplitude on the R free surface is 0.721. This ratio ($r_o = \frac{R}{n_o}$) leads to $s_0 = 1.387R$. Therefore, this result is assumed to be valid regardless of the position, and is thus applied to all heated contact patches. Figure 4.10 illustrates this description when the considered contact patch is located at the center point of the heat loaded zone.

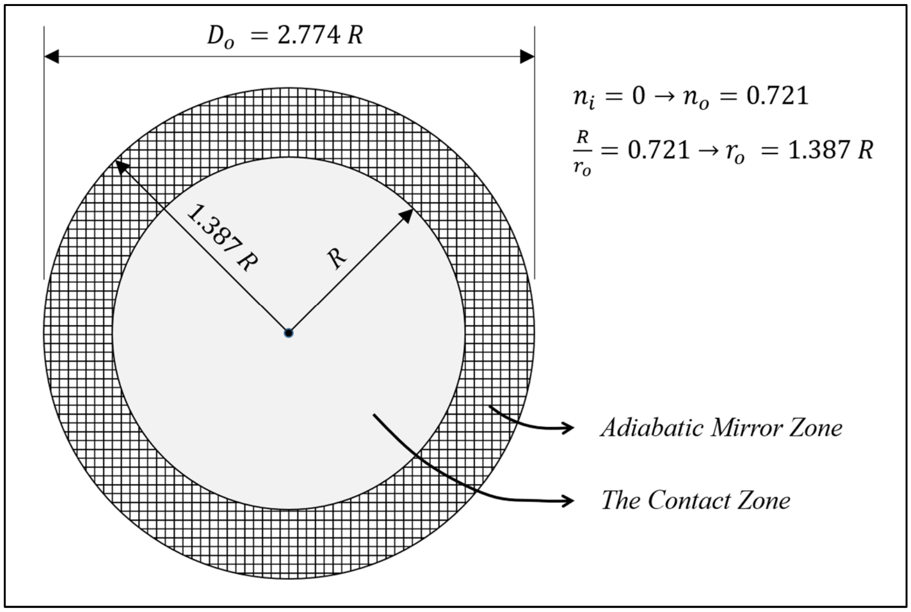

Figure 4.10 Counterbalance zone

Figure 4.11 compares the model predictions and the FEA results. The graph presents dimensionless displacements given by $(w_{TE} - w_{TE_c})/R$, where w_{TE_c} is the thermoelastic displacement calculated at the center of the contact area. The model precision varies with the size of the contact patch. The results presented in Figure 4.11-a were established for a grid made of 50 x 50 square cells. To show the influence of the grid resolution, Figure 4.11-b superimposes the models results obtained with a finer grid size of 100 x 100 square cells to the plot of Figure 4.11-a.

The curves in Figure 4.11-a show that the model predictions correspond almost perfectly to the values determined by FEA simulations. This plot also evidences the influence of the free boundary heat flux correction. A comparison of the RMS deviation from the FEA evaluations indicates that the procedure put forward to correct the free boundary improves the predictions and reduces the RMS deviation associated with the no-correction case by more than 97%. Figure 4.11-b shows that reducing the size (side length) of the contact patch by 35% further improves the results; compared with the uncorrected boundary case, the fine grid reduces the RMS deviation by more than 99%. Table 4.1 compares the calculation times of these three models (no-corrections and two grid sizes) to the duration of the reference FEA simulation. In addition to significant reductions of the computation effort, Table 4.1 shows that the free boundary correction procedure requires no additional time.

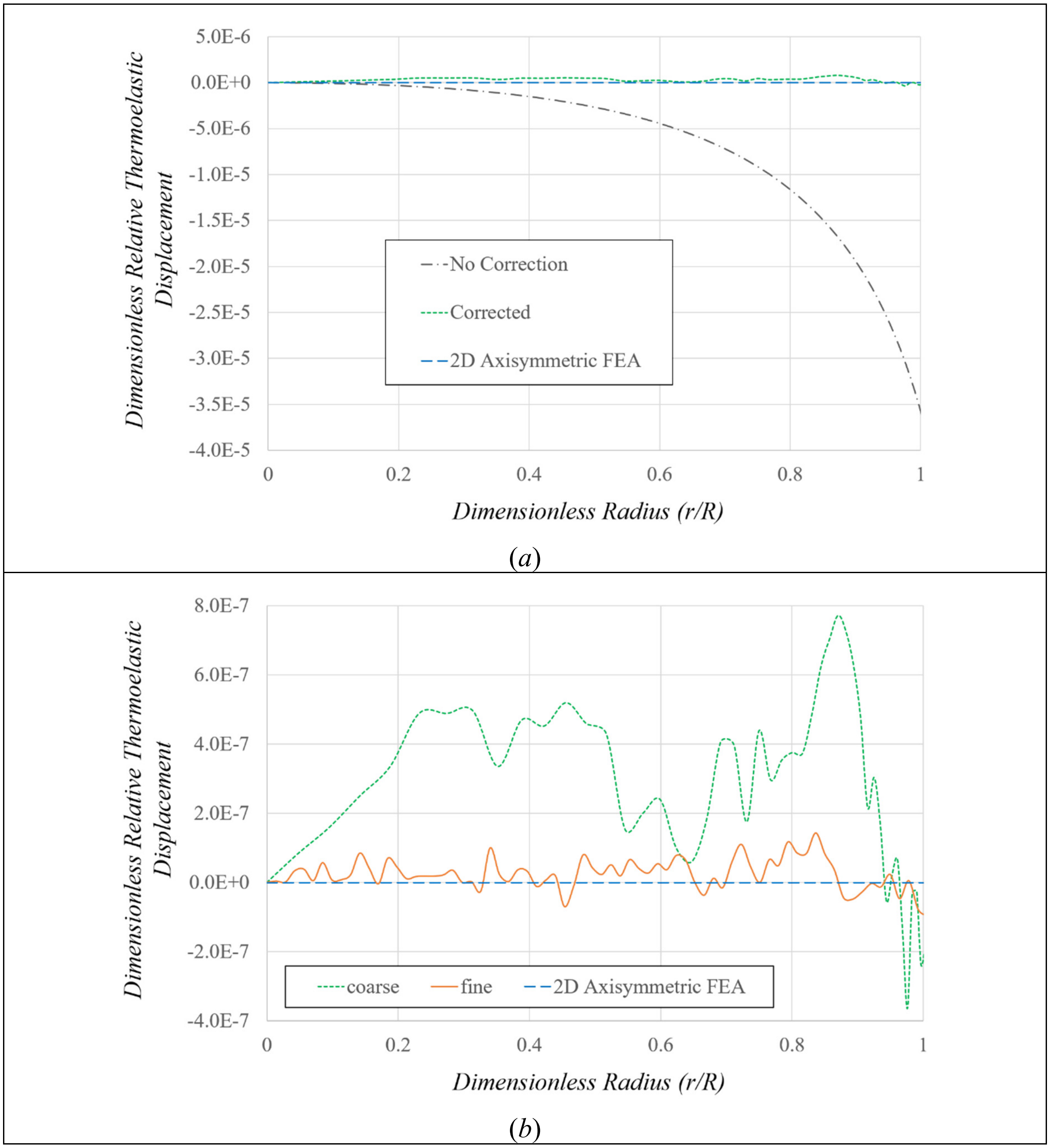

(*a*)

(*b*)

Figure 4.11 Thermal boundary validation

Table 4.1 Computation times for two grid sizes compared with FEA

	Grid size		
	No correction	Corrected free boundary	
	50×50	50×50	100×100
Time (sec)	*2*	*2.5*	*6.5*
Time reduction (%)	*93.5*	*91.9*	*78.9*

4.6 Cylindrical surface relief from normal stress

The present study deploys a solution strategy combining the approaches proposed by the authors in Ref. (Yalpanian & Guilbault, 2021) and Ref. (Yalpanian & Guilbault, 2020). Those approaches were developed to integrate thermoelastic effects in straight edge contacts and to release curved free surfaces from residual normal stress distributions in models based on the half-space assumption, respectively. When including thermoelastic deformations, the residual normal stresses affecting the free surfaces result from the combined effects of both the initial and the correction heat loads. Basically, the proposed strategy adapts the correction heat load to eliminate the consequences of the thermoelastic normal stress distribution on the displacements of the half-space.

Although the procedure aims at correcting the influence of normal stresses induced by a heat flux distribution over a given contact surface, the calculation process is essentially elastic, and leads to developments similar to those presented in Ref. (Yalpanian & Guilbault, 2020). The calculation process involves the following steps: 1- it first calculates the resultant normal force present at the free surface position, as well as its position; 2- it applies an opposite normal force of the same amplitude at the position of the force to be corrected; 3- to avoid the generation of a shear stress distribution on the half-space surface, the process also applies a mirror correction force with respect to the half-space surface; 4- these two forces provoke a new normal stress distribution over the half-space surface, which in turn must also be eliminated; 5- corrective actions similar to the previous steps are then required for the half-space surface. However, as for the correction of the heat flow generated across a surface of radius R, the curved edges defining the contact area require the definition of a corrective outer load located on an arc of radius r_o. Steps 1 to 5 are alternatively repeated to release the free boundary and the half-space surface and converge after an infinite number of iterations. However, after the first iteration, the efforts considered in Step 1 are no longer thermoelastic forces, but rather, elastic forces produced during the correction progression.

The following sections determine the thermoelastic normal stress distributions brought about on a curved surface (radius *R*) by a heat load distributed on the half-space over an arc of radius r_i (Step 1), and establish the position of the neutralizing external load required in Step 5. Steps 2, 3 and 4 do not involve any action specific to the presence of the curved free boundary. The last subsection introduces the complete releasing process.

4.6.1 Thermoelastic formulation

4.6.1.1 Normal stress induced at a radial position R by a heat load distributed over an arc of radius r

The thermoelastic normal stress distribution induced over a cylindrical surface (defined by a radius *R*) by a heat load distributed over an arc of radius *r* on a half-space is calculated using the Fourier integral (Baddour, 2011 ; Spiga & Carpinteri, 1984). Eq. (4.19) formulates this normal stress ($\sigma_{r_{TE}}$) for the position (*R, 0, z*). This equation is valid for both inner (r_i) and outer (r_o) positions of the arc heat load.

$$\sigma_{r_{i,o}TE} = -\frac{\gamma E \hat{Q}_{r_{i,o}}\, r_{i,o}}{k} \int_0^{\infty} \exp(-uz) \frac{J_0(u) J_1\left(\frac{uR}{r_{i,o}}\right)}{\frac{R}{r_{i,o}} u}\, du \qquad (\ 4.19\ )$$

where E is the Module of elasticity (Pa), γ is the thermal expansion (K^{-1}), k is the thermal conductivity (W/m °K), a is a Fourier integration parameter, while J_0 and J_1 are Bessel functions. The following equation (Eq. (4.20)) gives the dimensionless version of this normal stress:

$$\overline{\sigma_{r_{i,o}}}_{TE} = \sigma_{r_{i,o}te}\frac{k}{\gamma E\hat{Q}_{r_{i,o}}r_{i,o}} \tag{4.20}$$

The introduction of the dimensionless parameter n_i into Eq. (4.20) gives the dimensionless thermoelastic normal stress caused by a heat load distributed over a radius *ri* on the half-space surface (Eq. (4.21)). Eq. (4.22) expresses the same relation for *ro*:

$$\overline{\sigma_{r_i}}_{TE} = -\int_0^{\infty} \exp(-uz)\frac{J_0(u)J_1\left(\frac{u}{n_i}\right)}{\frac{u}{n_i}}\,du \tag{4.21}$$

$$\overline{\sigma_{r_o}}_{TE} = -\int_0^{\infty} \exp(-uz)\frac{J_0(u)J_1(un_o)}{n_o u}\,du \tag{4.22}$$

Identical to the above procedure for the correction of the heat flux at the free boundary, the technique proposed for the thermoelastic normal stress suppression works with the resultant force and the line of action of the stress distribution. Eq. (4.23) establishes the resultant force $F_{\sigma_{r_{i_{TE}}}}$ calculated over the free boundary at $\theta = 0$ (see Figure 4.4) and along the *z* direction, when the heat load is distributed over an internal arc [0, 2π] of radius *ri*. Eq. (4.24) gives the corresponding resultant force $F_{\sigma_{r_{o_{TE}}}}$ when the loaded arc is external and has a radius *ro*.

$$F_{\sigma_{r_{i_{TE}}}} = \int_0^{\infty}\int_0^{\infty} \exp(-uz)\frac{J_0(u)J_1\left(\frac{u}{n_i}\right)}{\left(\frac{u}{n_i}\right)}\,du\,dz \tag{4.23}$$

$$F_{\sigma_{r_{o_{TE}}}} = \int_0^{\infty}\int_0^{\infty} \exp(-uz)\frac{J_0(u)J_1(un_o)}{(un_o)}\,du\,dz \tag{4.24}$$

Eq. (4.25) formulates $l_{r_{TE}}$ the position of the resultant force along the axis *z* measured from the half-space top surface.

$$l_{r_{i,o_{TE}}} = \frac{\int_0^\infty z\, \sigma_{rTE}\, dz}{\int_0^\infty \sigma_{rTE}\, dz} \qquad (4.25)$$

4.6.1.2 Normal displacement of the surface of a half-space induced by a heat load distributed over an arc of radius r

Eq. (4.26) writes the thermoelastic displacement ($W_{TE-Q_{r_i}}$) caused at the radius *ri* by a heat load $\hat{Q}_{r_o}$ distributed over the correction arc of radius *ro*. Eq. (4.26) includes the value of *s0* (= 1.387 *R*) considered in the previous sections. This expression result from the integration of Eq. (4.4) along the ring of radius *ro*. This relation considers a specific point (*ri*, *0*). However, because of the axisymmetric nature of the ring shape, Eq. (4.26) represents any point of a ring of radius *ri*. The applied heat charge is $q = r_o \hat{Q}_{r_o} d\theta$ and the distance is $s = \sqrt{{r_o}^2 + {r_i}^2 - 2 r_o r_i \cos(\theta)}$.

$$W_{TE-Q_{r_i}} = \left(\frac{\hat{Q}_{r_o} R}{k n_o}\right) \frac{\alpha(1+\nu)}{2\pi} \Bigg[2\pi \log(1.387) - 2 \int_0^\pi \log\left(\sqrt{1 + n_i {n_o}^2 - 2 n_i n_o \cos\theta}\right) d\theta \Bigg] \qquad (4.26)$$

4.6.2 Elastic formulation

4.6.2.1 Normal stress induced at a radial position R by a normal load distributed over an arc of radius r

The method proposed for the calculation of the elastic normal stresses was originally put forward in Ref. (Yalpanian & Guilbault, 2020); this reference provides a complete description of the procedure. Hence, the present section only recapitulates the concepts behind the approach and highlights the important formulas.

In summary, a pressure active on a half-space results in internal stress distributions. It is well known that placing a counterbalance pressure at a selected position with respect to a specific boundary allows eliminating the internal shear stress over that boundary. Likewise, to free the boundary from the remaining normal stress, the correction procedure must include the addition of an opposite equivalent stress distribution. As indicated above in the description of the five-step solution, the process is iterative and involves lengthy calculations. Therefore, with the objective of eliminating the laborious iterative process, the procedure put forward in Ref. (Guilbault, 2011) and adapted to curved boundaries in Ref. (Yalpanian & Guilbault, 2020) , aims solely at canceling out the impact of the residual normal stress on the displacement of the half-space top surface. The proposed strategy simply accentuates the shear stress correction produced by the corrective load to compensate for the normal stress influence. This adaptation of the counterbalance load contribution is produced by a correction factor. To define this factor, the approach first establishes the normal stress effect on the displacement, and then a simple comparison with the displacement correction produced by the counterbalance load allows to define the required adaptation. As with the heat load correction, the process is based on the resultant force generated by the normal stress distribution (σ_{r_E}) and its line of action. Thus, Ref. (Yalpanian & Guilbault, 2020) first defines the resultant normal force ($F_{\sigma_{r_E}}$) on the free boundary as well as is position (l_{r_E}) along the *z*-axis from the half-space top surface. Thus, $F_{\sigma_{r_E}}$is the resultant of the σ_{r_E} stress induced on a free surface defined by a radius *R* by a load $\hat{F}$ distributed on a ring of radius *r*.

Eq. (4.27) establishes the normal force $F_{\sigma_{r_{i_E}}}$acting at the position $\theta = 0$, $r = R$ and $z = l_{r_{E_i}}$, resulting from a force load distributed over a ring of radius r_i on top of the half-space. Eq. (4.28) gives the equivalent normal force $F_{\sigma_{r_{o_E}}}$ calculated for a force load distributed over a ring of radius r_o. Finally, Eq. (4.29) formulates l_{r_E}.

$$F_{\sigma_{r_{i_E}}} = -\frac{\hat{F}\nu n_i}{\pi}\int_{-\pi}^{\pi}\frac{(1+{n_i}^2\cos(\theta)^2-2n_i\cos(\theta))}{(1+{n_i}^2-2n_i\cos(\theta))^{\frac{3}{2}}}d\theta \tag{4.27}$$

$$F_{\sigma_{r_{o_E}}} = -\frac{\hat{F}\nu}{\pi}\int_{-\pi}^{\pi}\frac{({n_o}^2+\cos(\theta)^2-2n_o\cos(\theta))}{(1+{n_o}^2-2n_o\cos(\theta))^{\frac{3}{2}}}d\theta \tag{4.28}$$

$$l_{r_E} = \frac{\int_0^{\infty} z\,\sigma_{r_E}\,dz}{\int_0^{\infty}\sigma_{r_E}\,dz} \tag{4.29}$$

4.6.2.2 Normal displacement of the surface of a half-space induced by a normal load distributed over an arc of radius r

Eq. (4.30) writes the normal displacement $w_{E_{r_i}}$ induced at a radial position *ri* of a half-space top surface, when a normal load $F_{\sigma_{z_E}}$ (calculated using Eq. (4.33)) is distributed over a ring of radius r_o (Figure 4.13). This formulation was proposed by Lubarda (Lubarda, 2013).

$$w_{E_{r_i}} = \frac{2\hat{F}(1-v)}{\pi G}K\left(\frac{r}{r_O}\right) \tag{4.30}$$

Where *G* is the shear modulus and *K* is the elliptical integral of the first kind.

4.6.2.3 Normal stress produced on a cylindrical section by a radial lateral load

The presented technic replaces the free surface stress distributions resulting from the heat and force loads active on the half-space top surface by their resultant forces ($F_{\sigma_{r_{i_{TE}}}}$, $F_{\sigma_{r_{o_{TE}}}}$, $F_{\sigma_{r_{i_E}}}$, $F_{\sigma_{r_{o_E}}}$). These resultants are distributed radial forces acting around the surface defined by the *R* radius at a position $z = l_r$. Figure 4.12 illustrates this description and shows a radial force F_σ. The elimination process of these normal forces results from the adding of a counteractive distributed force at the same location along the axial direction.

The addition of any force distribution around the cylindric surface (of radius *R*) causes normal stresses and displacements oriented along the *z* axis in response. Therefore, the relations defining the effect of a radial load on the body are also needed. Ref. (Yalpanian & Guilbault, 2020) presents the complete development work leading to the formulation. Therefore, the present article only includes the final expressions required for the thermoelastic normal stress elimination process.

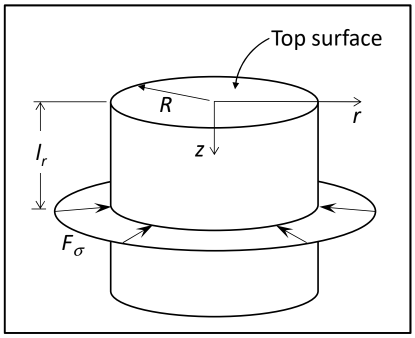

Figure 4.12 Radial force distribution

The procedure replaces the radial force F_σ by a pressure strip of axial thickness *dz*. This thickness is chosen sufficiently narrow to parallel a line load (*dz=0.001R*) (Yalpanian & Guilbault, 2020). Eq. (4.31) formulates the normal stress (σ_{z_E}) induced along the *z* axis at a distance *z* by a pressure strip encircling a cylinder. As indicated by Eq. (4.31), the pressure band results from the overlap of two pressure loads located at *z* and *z* + *dz* distances from the considered position. Eq. (4.32) gives σ_{z_E}. This relation intrinsically assumes that the radial force F_σ acts at *z* = 0.

$$\sigma_{z_E} = \left(\sigma_{z_F} - \sigma_{(z+dz)_F}\right) \tag{4.31}$$

$$\sigma_{z_F} = -\frac{F_\sigma}{\pi\, dz} \times \int_0^\infty \frac{sin(uz)\left(2Ru^3 I_1(uR) I_0(ur) - R^2u^4 I_0(uR) I_0(ur) + Ru^4 r I_1(uR) I_1(ur)\right)}{u^3\left[\left(I_1(uR)\right)^2 (R^2u^2 - 2v + 2) - R^2u^2\left(I_0(uR)\right)^2\right]} d \tag{4.32}$$

where I_0 and I_1 are modified Bessel functions and u is an integration parameter which takes a range of values ($\in$ [0, ∞]).

Eq. (4.33) gives the distributed force ($F_{\sigma_{z_E}}$) resultant (in the axial direction of the cylinder) from the normal stresses σ_{z_E} generated at both z and $-z$ positions.

$$F_{\sigma_{z_E}} = \int_0^R \sigma_{z_E} dr\bigg|_z = \int_0^R \sigma_{z_E} dr\bigg|_{-z} \tag{4.33}$$

Eq. (4.34) establishes the location of the line of action or the radius r_z of the ring supporting the $F_{\sigma_{z_E}}$ distribution (see Figure 4.13), while Eq. (4.35) gives the corresponding position from the edge (r'_z).

$$r_z = \frac{\int_0^R r\, \sigma_{z_E}\, dr}{\int_0^R \sigma_{z_E}\, dr} \tag{4.34}$$

$$r'_z = R - r_z \tag{4.35}$$

4.6.2.4 Axial displacement of a cylindrical section produced by a radial lateral load

Eq. (4.36) depicts the axial displacement w_{z_E} produced by a pressure strip encircling a cylindrical body (Yalpanian & Guilbault, 2020). To reproduce the load condition illustrated in Figure 4.12, the size of the pressure strip is again fixed at $dz = 0.001R$. Eq. (4.37) formulates the displacement generated by the two pressure loads forming the band load. These pressures are located at a distance z and $z + dz$ from the considered position, respectively.

$$w_{z_E} = \left(w_{z_F} - w_{(z+dz)_F}\right) \tag{4.36}$$

$$w_{z_F} = \frac{F_\sigma}{2\pi G\ dz} \times \int_0^\infty \frac{cos(kz)R\big(RkI_0(kR)I_0(kr) - krI_1(kR)I_1(kr) + 2I_1(kR)I_0(kr)(v-1)\big)}{k\left[\big(I_1(kR)\big)^2(R^2k^2 - 2v + 2) - R^2k^2\big(I_0(kR)\big)^2\right]} d \qquad (4.37)$$

4.6.3 Normal stress relief procedure for a cylindrical surface

The thermoelastic normal stress present on the free surface results from a combination of the effects of both the initial and the counterbalance heat loads. Moreover, since an adiabatic boundary condition means the absence of a crossing heat flux, this condition imposes the maximum counterbalance heat loads, and as a consequence, leads to the largest normal stress amplitude. Thus, the present section first considers this severest condition to develop the elimination process of the thermoelastic normal stress active on a curved free surface. Since the proposed approach follows the strategy initially put forward in Ref. (Guilbault, 2011), it neutralizes the normal stress influence on the displacement via an overcorrection factor or a thermoelastic normal stress elimination factor (nsf_{TE}), which modifies the correction brought in by a counterbalance heat load.

As described earlier, in addition to their contribution to the displacement of the half-space surface $W_{TE-Q_{r_i}}$(given by Eq. (4.23)), a heat load distributed over an arc of radius r_i and its counterbalance heat load *Q'* distributed over an arc of radius r_o engender a superposition of normal stress distributions ${\sigma_{r_{i,o}}}_{TE}$ on the free surface. Hence, eliminating the thermoelastic stress accumulation requires an opposite equivalent normal stress. The following description details the five-step procedure introduced in Section 4.6 . Figure 4.13 also portrays the operation.

The procedure replaces the normal stress distribution with their resultant force $F_{{\sigma_{r_{i,o}}}_{TE}}$ (given by Eqs. (4.23) and (4.24))). As indicated earlier, these forces are radial ring loads acting around the cylindrical free surface at the axial position ${l_{r_{i,o}}}_{TE}$ (calculated by Eq. (4.25)). The required antagonistic ring loads $F_{{\sigma_{r_{i,o}}}_{TE}}$ are thus applied at the corresponding distances from the half-space top surface. However, in response, this corrective action also generates shear and normal stresses on the half-space surface. The shear stress is easily canceled out by the mirroring approach. Thus, the procedure introduces equal loads in symmetrical positions with respect to the half-space surface ($F'_{\sigma_{r_{i,o}}{}_{TE}}$). These correction and counterbalance forces (two $F_{\sigma ri,o_{TE}}$ - $F'_{\sigma ri,o_{TE}}$ pairs) cause a build-up of elastic normal displacement w_{z_E} (calculated by Eq. (4.36)) and stresses σ_{z_E} on the half-space surface in the *z* direction (Eq. (4.31)). The resultant forces $F_{\sigma_{z_E}}$ and the radius r_z of the rings supporting their distributions are calculated with Eq. (4.33) and Eq. (4.34), respectively. Opposing force distributions of the same amplitudes are then applied to cancel out these normal loads. To avoid the development of a shear stress distribution over the free surface of radius *R*, this corrective operation again requires the action of distributed forces $F'_{\sigma_{z_E}}$ counterbalancing $F_{\sigma_{z_E}}$. The radius of the ring supporting the $F'_{\sigma_{z_E}}$ distribution is calculated via Eq. (4.38), which is the force load version of the heat load formulation given by Eq. (4.18). Ref. (Yalpanian & Guilbault, 2020) provides a detailed description of the development of Eq. (4.38). The reader is thus referred to these papers for a complete portrayal. In Eq. (4.38) the definition of $n_{i,o}$ remains the same as the one considered in Eq. (4.18). However, the radius involved in their calculation are associated with normal stress distributions. Thus, r_i becomes r_{z_i} and is determined with Eq. (4.34), while radius r_o becomes r_{z_o}. The adapted $n_{i,o}$ definitions are given below. These correction forces ($F_{\sigma_{z_E}}$, $F'_{\sigma_{z_E}}$) cause the reoccurrence of a normal stress distribution on the free surface. This new stress distributions require the addition of the correction forces $F_{\sigma_{r_{i,o}}{}_{E-2}}$ as well as their counterbalance part $F'_{\sigma_{r_{i,o}}{}_{E-2}}$. These first few elimination steps clearly describe an iterative correction process. Moreover, it should be noted that, since the positions of the force action line increase at each iteration, the process is convergent.

$$n_o(n_i) = \frac{p_1 {n_i}^4 + p_2 {n_i}^3 + p_3 {n_i}^2 + p_4 n_i + p_5}{{n_o}^5 + q_1 {n_o}^4 + q_2 {n_o}^3 + q_3 {n_o}^2 + q_4 n_o + q_5} \tag{4.38}$$

where $n_i = \frac{r_{z_i}}{R}, n_o = \frac{R}{r_{z_o}}$ and

$p_1 = 0.2381$ $p_2 = -0.1652$ $p_3 = -0.00943$ $p_4 = 0.02335$ $p_5 = 9.47e-5$

$q_1 = -3.1$ $q_2 = 3.935$ $q_3 = -2.214$ $q_4 = 0.4578$ $q_5 = 0.008826$

At the end of the boundary releasing operation, the displacement of the half-space surface at the position of the initial heat load $\hat{Q}_{r_i}$ will combine the effect of the counterbalancing heat load $\hat{Q}_{r_o}$ deduced from Eq. (4.26), the displacements caused by the counterbalancing thermoelastic forces marked by a *prime* $F'_{\sigma_{r_{i,o_{TE}}}}$ and $F'_{\sigma_{z_E}}$ (deduced from Eq. (4.36) and Eq. (4.30), respectively), and to this initial corrective passage, the progression of the iterative scheme will add on the displacements induced by the succession of the corrective elastic forces $F'_{\sigma_{r_E}}$and $F'_{\sigma_{z_E}}$ (also deduced from Eq. (4.36) and Eq. (4.30)).

Hence, the complete iterative scheme will produce the thermoelastic surface displacement caused by a heat flux q'' acting on a patch inside the contact area ($w_{Q_{total}}$) expressed by Eq. (4.39).

$$w_{Q_{total}} = w_Q + w_{Q^*} \tag{4.39}$$

$$w_{Q^*} = W_{TE-Q_{r_i}} + \sum_{u=1}^{\infty} \left(w_{z_E}\right)_u + \sum_{u=1}^{\infty} \left(w_{E_{r_i}}\right)_u \tag{4.40}$$

Similar to the strategy used in Ref. (Yalpanian & Guilbault, 2021) to avoid the calculation efforts involved in the correction process described by the infinite series in Eq. (4.40), this study assumes that a modified counterbalance heat load q''^{*} should produce a displacement of the half-space surface equal to w_{Q^*}. Consequently, q''^{*} should be calculated as indicated by Eq.

(4.41), where *nsf*nsf_{TE} is the thermoelastic correction factor. This factor is thus written as indicated by Eq. (4.42).

$$q''^{*} = nsf_{TE}\, q'' \tag{4.41}$$

$$nsf_{TE} = \left[{w_{Q^*}}\big/{W_{TE-Q_{r_i}}} \right] \tag{4.42}$$

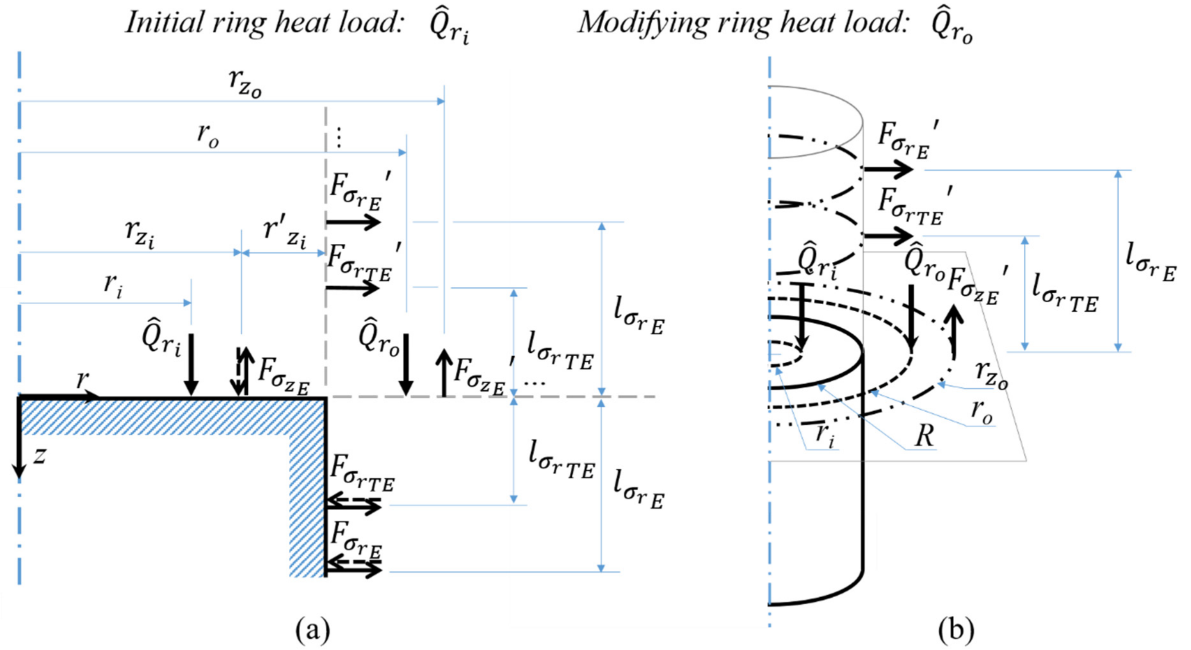

Figure 4.13 First actions of residual thermoelastic normal stress suppression operation

Eq. (4.42) allows calculating nsf_{TE} for any r_i (radius of the arc submitted to the heat load). The obtained equation system depends on the Poisson ratio. To evaluate nsf_{TE}, a series of simulations considering various r_i radius of the heat load distribution were realized. The investigation examined dimensionless distances n_i, and as before fixed s_0 at 1.387R (see Figure 4.10). The 3rd degree polynomial curve fit given by Eqs. (4.43) and (4.44) summarizes the results, and since the nsf_{TE} factor depends on the Poisson ratio, the constants in Eq. (4.44) are functions of this parameter.

$$nsf_{TE} = a_0 + a_1 \mathrm{n}_I + a_2 \mathrm{n}_I{}^2 + a_3 \mathrm{n}_I{}^3 \quad (4.43)$$

$$a_0 = 1.7875 - 4.0549\,v + 1.6402\,v^2 \quad (4.44)$$

$$a_1 = 0.0947 - 0.4272\,v + 0.1734\,v^2$$

$$a_2 = 0.1598 - 2.5160\,v + 1.0164\,v^2$$

$$a_3 = 0.5494 - 1.8067\,v + 0.7316\,v^2$$

4.7 Summary of the proposed approach

The following steps summarize the approach detailed in the previous sections to release the free boundaries from the artificial stress generated during the modeling of thermoelastic contacts between bodies limited by curved surfaces. These actions concern the thermoelastic aspect of the problem and should be coupled with the procedure put forward in Ref. (Yalpanian & Guilbault, 2020) for the elastic contribution:

1) The pressure-heat patches defined over the contact area may each simultaneously sustain a constant pressure load and a constant heat load;
2) The procedure in Ref. (Yalpanian & Guilbault, 2020) allows defining the corrective pressure patch size and position for the correction pressure;
3) Eq. (4.18) maps the pressure-heat patch on a corrective heat patch and establishes the location of the correction heat load;
4) Compute the area of the corrective heat patch and exchange it for a square patch of equal area (see Figure 4.6);
5) Impose the heat q'' (equal to the original on the pressure-heat patch) on the corrective patch to control the heat flux crossing the free boundary;

Calculate nfs_{TE} with Eqs. (4.43) and (4.44), and multiply the heat flux q'' defined in Section 4.3 by nfs_{TE} to obtainq''^{*}. q''^{*} eliminates the thermoelastic normal stress caused on the curved surface of radius *R* by the heat load.

4.8 Validation of the model

Figure 4.14-a shows the contact system considered for the model validation. The problem definition assembles two long cylinders of radius $R = 10$ mm pressed against each other with a 10 kN load. In addition, a uniform heat source is distributed over the contact area, while the free surfaces are submitted to an adiabatic boundary condition. In the following models, if not mentioned specifically, the heat flux is $q'' = 28.125\ \text{kW/m}^2$. The Poisson ratio of the cylinder material is 0.3.

The following validation compares the contact pressure distributions established by the proposed model with results obtained from 2D axisymmetric FEA. This 2D FEA simplification provides accurate and useful validation results. However, it is limited to fully symmetric geometry, support and loading conditions. On the other hand, the developed model is equivalent to 3D FEA and can handle any practical conditions. Figure displays a representative contact model composed of rectangular pressure-heat cells. As mentioned before, Eq. (4.18) maps each four-sided cell belonging to the contact zone to an external corrective patch.

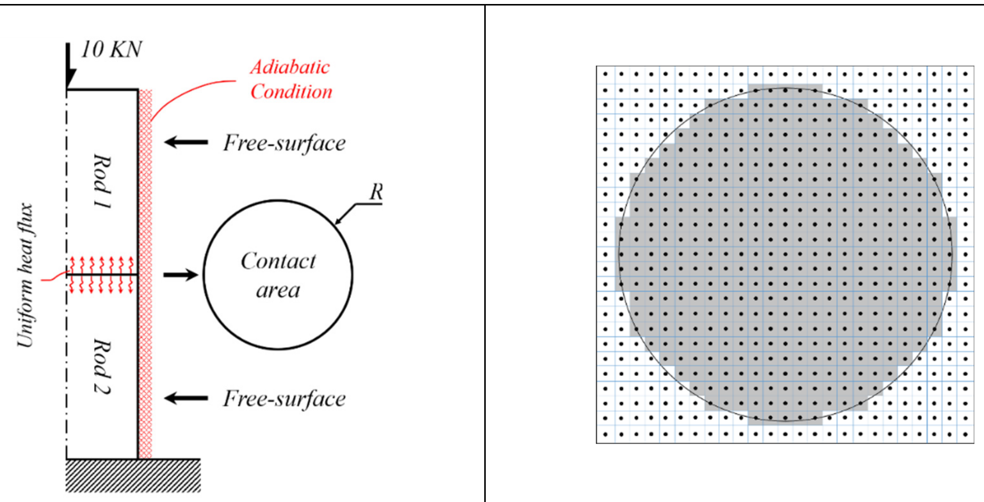

(a) (b)

Figure 4.14 (a) Rod problem (b) Contact mesh with rectangular pressure-heat patches

To illustrate the nsf_{TE} role, Figure 4.15-a juxtaposes the FEA results and the pressure definition determined by the Hartnett's method over the contact zone when considering two conditions. The first one solely imposes the adiabatic boundary condition on the free surface, and neglects the influence of the thermoelastic normal stress or sets nsf_{TE} at one. This condition is designated as the *Partial correction*. The second one imposes the adiabatic boundary condition on the free surface, and eliminates the impact of the thermoelastic normal stress or integrates the nsf_{TE} values established via Eqs. (4.43) and (4.44) for each correction heat patch. This condition is designated as the *Complete correction*. It is also important to mention here, that, for all test cases, the influence of the elastic normal stress produced on the free surfaces by the pressure load is eliminated following the procedure developed in Ref. (Yalpanian & Guilbault, 2020). Figure 4.15 displays dimensionless graphs: the horizontal axes correspond to radial positions $\bar{r} = r/R$, while the vertical axes show pressure values $\bar{P} = P/P_{ave}$, where P_{ave} is the average pressure. The model predictions presented in Figure 4.15-a were calculated with a relatively coarse mesh composed of 50 pressure-heat patches along the horizontal and the vertical directions of the contact area illustrated in Figure 4.14-b. Therefore, to describe the influence of the pressure-heat patch size, Figure 4.15-b compares the model predictions realized for the same system with a complete correction and three finer mesh definitions: 50, 100 and 150 pressure-heat patches along the horizontal and the vertical directions of the contact area. Table 4.2 shows the percentages of pressure difference calculated for the three mesh predictions in comparison with the FEA results. Table 4.3 completes the description with a comparison of the model calculation times with that of the 2D FEA. The 2D FEA required 820 sec to establish the results shown in Figure 4.15.

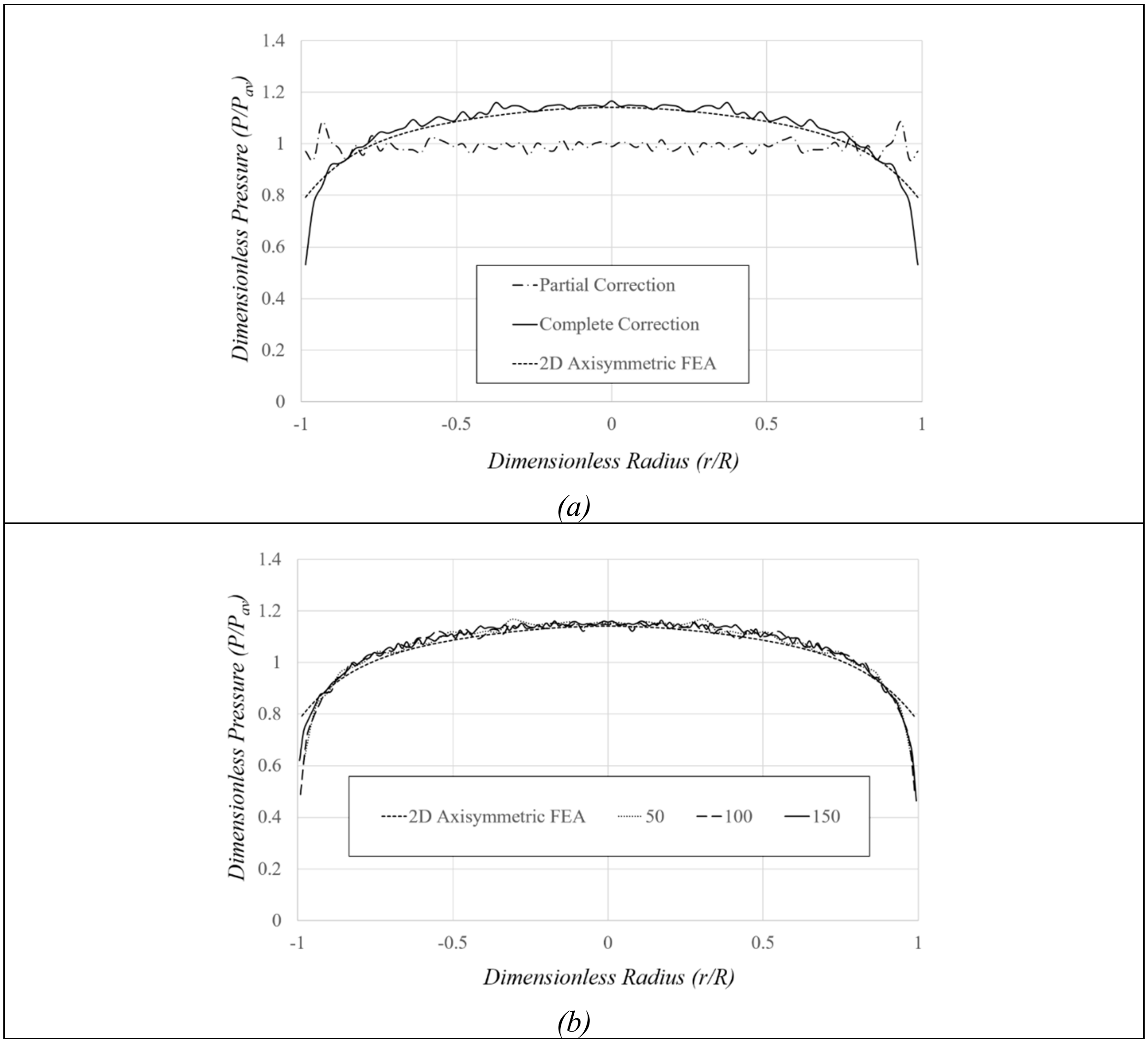

Figure 4.15 (a) Comparison of dimensionless contact pressures obtained from the proposed model to 2D axisymmetric FEA results; (b) Comparison of dimensionless contact pressures obtained from the proposed model with three mesh sizes to 2D axisymmetric FEA results

Table 4.2 Pressure differences for the three mesh sizes compared with the 2D Axisymmetric FEA

	Number of patches along *R*		
	50 x 50	100 x 100	150 x 150
Max deviation* (%)	*4.4%*	*4.2%*	*3.9%*

* *With the exception of the vicinity of the free edge*

Table 4.3 Computation times for the three mesh sizes compared with the 2D FEA duration of 820 sec

	Mesh size		
	50	100	150
Time (sec)	*13*	*177*	*1266*
Time reduction	*807*	*643*	*-446*
Reduction (%)	*98,4*	*78,4*	*-54,4* *(increase)*

Figure 4.15-a shows that, while the *Partial correction* maintains a visible difference when compared e the reference FEA results, the *Complete correction* condition offers evaluations in close agreement. The 18.5% average difference level of the *Partial correction* reduces to 5% with a complete elimination of the influence of the thermoelastic normal stress. This correction corresponds to a 73% gain in precision.

The graph in Figure 4.15-a also display a noticeable noise in the predictions. It may be suspected that this perturbation is attributable to the mesh size. Figure 4.15 compares different mesh sizes composed of regular reckon patches (constant area). A visual comparison shows that a reduction of the patch area leads to a drastic diminution of the remaining noise. The curves also seem to indicate that the 100 and 150 regular patch meshes provide equivalent noise reductions. Table 4.2 gives a precise evaluation of the maximum difference between the model predictions and the reference results; compared with the 100-patch mesh, the 150-patch case reduces by 0.3% the maximum difference. In reality, even compared with the 50-patch mesh the difference reduction obtained with the finer mesh remains quite low (0.5%); the maximum difference amplitude of 4.4% demonstrated by the 50-patch mesh indicates that these larger patches already provide high-quality results.

In fact, the considered contact mesh is composed of rectangular patches, which only approximate the curved boundary definition, and thus constitute an obvious imprecision source. Although the present study did not evaluate this avenue, it remains rational to believe that curvilinear trapezoidal contact patches would increase the precision. However, since the proposed approach is conceived to work with the Hartnett SAM, which works with rectangular contact patches, modifying the patch form was not an option. Moreover, the analysis presented in Ref. (Yalpanian & Guilbault, 2020) demonstrates for contact pressures not affected by a thermoelastic contribution that, reducing the size of rectangular patches close to the boundary provides sufficient precision improvements. Based on those observations and the result of Figure 4.15-b, this conclusion may be assumed to be applicable to thermoelastic contact problems. Thus, this reasoning or the fact that the precision close to the contact area edge may be further improved explains why the evaluation of the result deviation presented in Table 4.2 exclude the zone close to free boundary.

It is also important to underline that the complete correction realized with the insertion of nsf_{TE} into the model does not affect the solution times compared with a simple thermal boundary correction (*Partial correction)*. But more importantly, in contrast to those required for FEA, these solution times globally remain low. Table 4.3 reports the calculation time required for each mesh size, as well as the corresponding time economy. These values reveal that the calculation times grows exponentially with the patch number. For instance, the time needed for the 150-patch mesh solution even exceeds that of the FEA. In reality, since the 50 and 100-patch meshes assure an equivalent precision, the 150-patch mesh corresponds to an excessive refinement, and solely served to establish the convergence of the mesh accuracy. Therefore, it should not be further considered in the description of the model performance. The values in Table 4.3 show that compared with the FEA simulation, this 50-patch mesh saved more than 98% of the calculation time. It seems also worth to mention here that all the presented calculations were realized on a Quad core 3.4 GHz CPU computer.

To complement the portrayal of the model precision Figure 4.16 compares the 50-patch mesh results to evaluations obtained from the previous 2D FEA and a full 3D FEA. The 2 FEA meshes considered in this comparison involved 25 elements along the radial direction, or 50 elements along the diameter. The calculation times were 13 sec, 820 sec and 1532 sec for the proposed model, the 2D FEA and the 3D FEA, respectively. The graph clearly shows that the 3D FEA model produces result oscillations of the same type of those associated with the proposed model. However, the amplitude of the variations resulting from the proposed model predictions are significantly lower, while the proposed model is more than 117 times faster. Of course, the required time in 3D FEA increases by the power of three as the number of elements increase. In fact, the curve smoothing introduced by the 2D FEA evaluations is a sole consequence of the neglection of the third dimension.

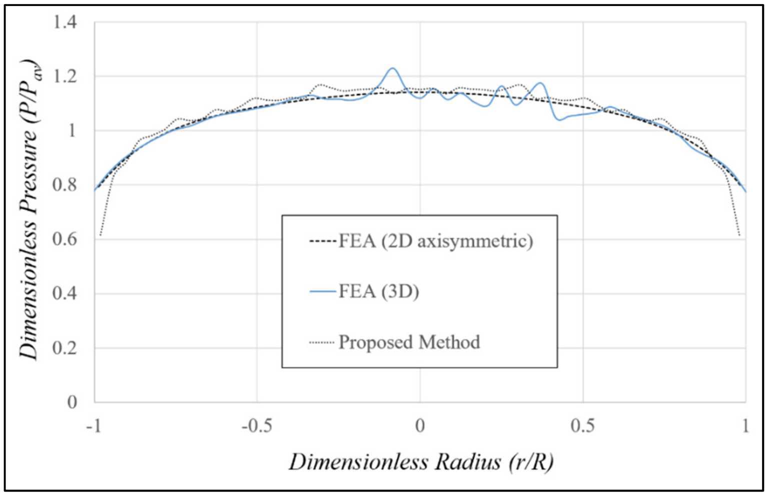

Figure 4.16 Comparison of the result precision obtained from the proposed method, 3D FEA and 2D axisymmetric FEA assuming 50 diagonal elements in every case

Finally, to provide a broader picture of the proposed approach precision, the following compares the model predictions to FEA evaluations made for eight configurations. These layouts combine two values of the radius R:10 mm and 15 mm, two heat fluxes q'' of 14.0625 kW/m^2 and 28.125 kW/m^2, and two Poison ratios (ν) 0.3 and 0.4, while the force load remains constant for all cases and again fixed at 10 kN. This instancing exclude the *Partial correction* discussed above. The calculations were all realized with 50 elements along the horizontal and vertical directions of the contact area. Therefore, the evaluations realized for the larger radius (R = 15 mm) involved contact patches 2.25 times larger than those of the R = 10 mm cases. This approach allows also integrating the influence of the mesh size into the description. Figure 4.17 presents the dimensionless pressure graph obtained for all layouts.

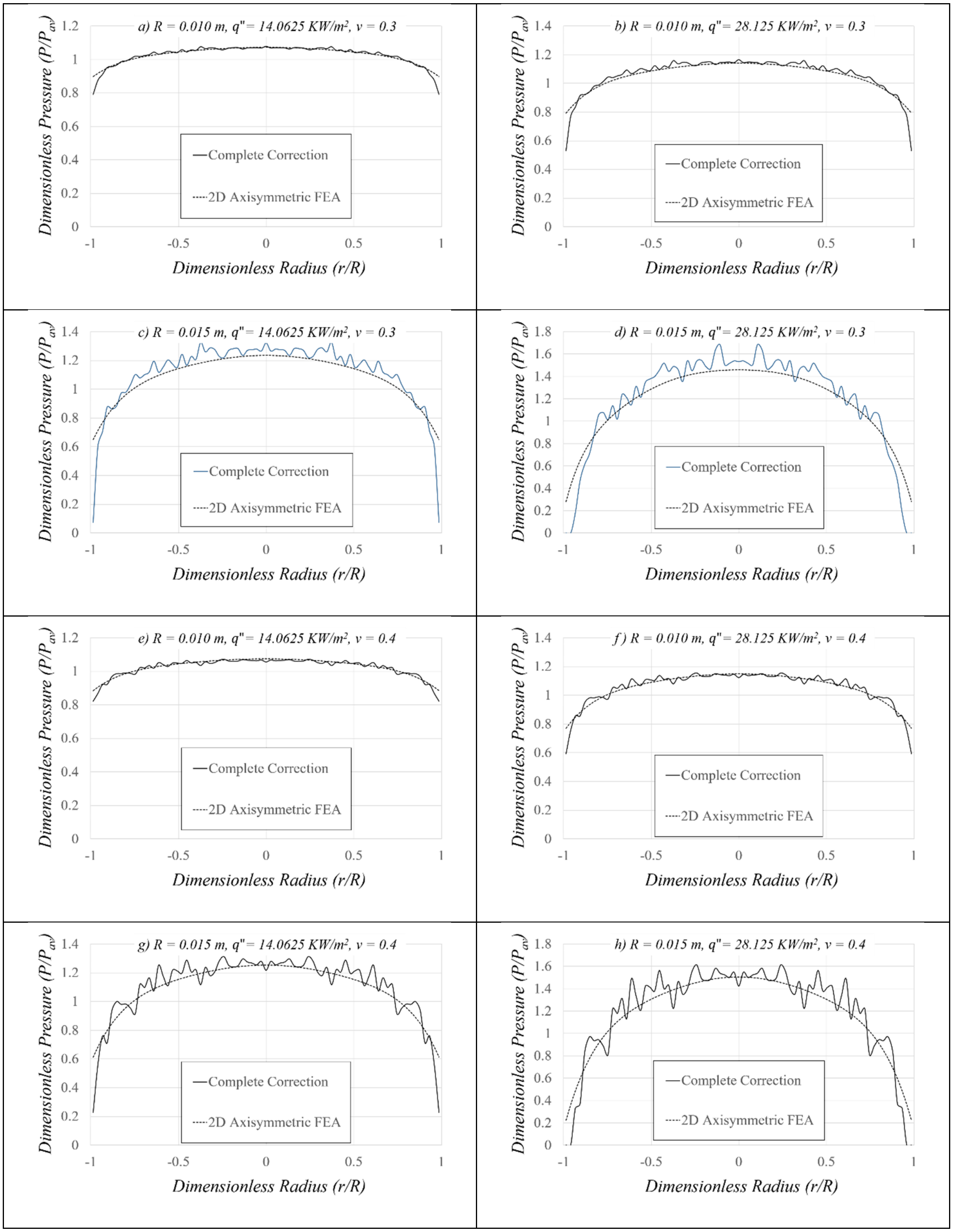

Figure 4.17 Dimensionless contact pressures obtained for different layouts

The graphs in Figure 4.17 show that the predictions of the proposed modeling approach match quite well the FEA results for all layouts. Thus, the model maintains high precision levels with different Poison ratios and heat flux. On the other hand, the more visible result fluctuations generated by the less refined mesh used with the *R*=15 mm layouts confirm the influence of the contact patch size.

4.9 Conclusions

The primary part of this work develops a modeling strategy based on influence factors to allow SAM predicting the impacts of thermoelastic deformations on contacts between bodies delimited by curved free boundaries. The proposed strategy represents an extension of the approach initially developed for bodies defined by straight surfaces. The objective is to control the heat flux crossing the free surfaces. The present study concentrated on imposing adiabatic conditions. However, the developed technic could easily be extended to any thermal conditions of the boundaries. With straight surfaces, the adiabatic condition involves a counterbalance heat load of amplitude equal to that of the contact heat load, but placed at a mirror position with respect to the free boundary. This flux control operation over curved boundaries benefits from a precise adaptation of both the position and size of the counterbalance heat patch. Thus, this study formulates the mapping relation linking the heat load to its counterbalance part. In fact, since the proposed approach is designed to work with the Hartnett's elastic contact model, which works with rectangular contact patches, the developed expression defines counterbalance patches for rectangular pressure-heat patches.

A comparison of the thermoelastic displacements predicted by the model with FEA results indicate that the developed thermal boundary rectification decreases the errors inherited from the half-space concept up to 99%. The proposed modeling strategy also significantly reduces the computation burden. Indeed, for the considered problems and equivalent precision levels, when compared with FEA, the proposed method reduced the calculation times by more than 92%.

The second part of this paper completes the free boundary release procedure, and introduces a corrective factor to remove the effect of the thermoelastic normal stress. In addition to the heat flux aspect, the half-space assumption also introduces inherent normal stress distributions on free surfaces. In order to preserve the advantageous calculation speed provided by the half-space approach, the correction strategy solely aims at canceling the half-space top surface displacements caused by the normal stress, and pays no attention the stress itself. The technic put forward introduces a correction factor to adjust the amplitude of the counterbalance heat load controlling the heat flux crossing the free boundary. A unique equation defines this correction factor. The complete free boundary correction procedure thus comprises two steps: the first determines the dimensions and location of the counterbalance heat patch controlling the heat flux crossing the curved free boundary, and the second adjusts the heat amplitude on this corrective patch to cancel out the thermoelastic normal stress influence.

The last part of the paper compares the predictions obtained from the proposed method to evaluations produced by finite element simulations. This final validation demonstrates the model capacity of accurately coping with bodies of various dimensions and made of various materials, as well as with different heat source intensities. In parallel with its manageability and efficacy, the proposed modeling approach is also faster than FEA. Indeed, when compared with FEA, for the considered problems and the obtained precision levels higher than 95%, the proposed method offered calculation time reductions higher than 98%.

CONCLUSION AND RECOMMENDATIONS

While improvement of the characteristics of bearings and contacts in general is a constant need of the industry, advancements in smart surface engineering and coating technologies have given the opportunity of increasing the fatigue and wear life of the contact surfaces by introducing different surface textures. The present study aimed to provide the proper tool for a thorough analysis of such surfaces by introducing a fast and reliable method for modeling contact surfaces with different negative or positive asperity geometries by adding the curved edge treatment and also thermoelastic consideration capability to the well-known half-space semi-analytical method. In the process of developing this reliable method, this study made the following main contributions:

1) Treating the curved free-edge of a contact in a half-space based method by proposing the position of the counterbalance pressure and applying an overcorrection factor in order to completely eliminate the superfluous effects of the half-space assumption;

2) Integrating the thermoelasticity effect to the half-space based method using a simple thermoelastic influence factor; and introducing the straight free-edge treatment to a thermal contact considering thermoelasticity effects while taking into account the thermal boundary condition at the free-surface;

3) Treating the curved free-edge of a contact considering thermoelasticity by proposing the position of the counterbalance heat patch and applying an overcorrection factor in order to completely eliminate the superfluous effects of the half-space assumption and modifying the introduced over correction factor to account for the thermal boundary condition.

As the first contribution, Chapter 2 (Article 1) presents a thorough study of the contacts with curved edges in a dry contact that can easily be applied on any type of contact, including lubricated contacts. The performed analysis identified the residual stresses of half-space assumption on the curved free-surface. This process, first, finds a radial position for a counterbalance load that eliminates the residual shear stresses on the free-surface generated by applying the main load on the contact surface. Applying the counterbalance load reduces the errors intrinsic to the half-space assumption by up to 92%. The process further improves the precision of the method by introducing a modifying factor for the counterbalancing load. This modifying factor is obtained from a cyclic stress elimination approach designed to eliminate the remaining residual normal stress on the curved free-surface. Applying this modifying factor results in further reduction of the error in comparison with FEA results (up to 96%). For the studied cases, considering equivalent precision, the proposed approach shows calculation times at least 9 times lower than those of the FEA. Contributions of the first article further improves the capability of the half-space based SAM for practical uses.

The limitations of Article 1 and further recommendations include:

- The curved edges validated in this study are limited to closed circular edges. A future study could consider other geometrical curved edges and the mixed curved and straight edges.

- The validation in this study is performed by comparing the obtained results with those of FEA. If possible, a comparison with an experimental data could give a better insight to this subject.

- Current study considers only elastic behavior. It could be beneficial if the future studies take into account the plastic behavior of the contact materials as well.

As for the second contribution, Chapter 3 (Article 2) generalizes the simulation method even further to include thermoelasticity effect as well. Doing so, thermal response of the contacting solids is also being taken into account. In order to integrate thermoelasticity consideration in the simulation method, the second article, first, uses the thermoelasticity formula proposed by Barber (Barber, 1971) to develop an additional factor to implement thermoelasticity consideration into the developed contact analysis method. This approach greatly simplifies the integration of thermoelasticity into the already prepared fast SAM. The next step to achieve a general contact analysis model is to consider the straight free-edges while taking into account thermoelasticity. To consider the free edges, the study calculates the heat flux that crosses the free-surface because of half-space assumption. Then, it proposes a counterbalance load for eliminating this heat flux resulting in an adiabatic thermal condition. Afterwards, a modification factor accounts for other thermal boundary conditions at the free border. Comparing the results obtained using the proposed method for an adiabatic thermal boundary condition with the results obtained from FEA verifies the accuracy and precision of the proposed method. It also shows a 98% reduction in calculations time.

In the next step, the study successfully applied the proposed method in contact analysis of an elastohydrodynamicaly lubricated contact by demonstrating the effects of considering thermoelasticity effects and free-edge considerations using a factorial analysis. The results obtained considering thermoelasticity and adiabatic thermal boundary at the free-edge demonstrated an overall increases in the maximum pressure of around 9%, an overall decrease in the film thickness close to 7%, and an overall temperature increase of about 2°K. This is what was missing from non-thermoelastic analysis of TEHL, which is achieved as part of the main goal of preparing a through contact analysis model.

The limitations of Article 2 and further recommendations include:

- The thermoelasticity approach considered in this study is in steady state. This assumption both simplifies the process and considerably reduces the time consumption of the process. To obtain a more general model, future studies could consider time dependency as well. This requires a careful attention at time consumption.

- In this part of the study only straight free-edges are considered. The next part of this thesis will focus on curved free-edges for thermoelastic contacts.

- While the thermal boundary condition modification factor is proposed in this study, a further development of this thermal boundary factor could be a more precise tool for more general thermal boundary conditions at the free-surface.

In terms of the last contributions of this study, as mentioned earlier, in Chapter 4 (Article 4) the focus is on handling curved free-edges while considering thermoelasticity in a thermal contact analysis. Doing so, this study achieves the intended goal of creating a contact analysis method that is rather fast and reliable while considering most practical phenomena in mechanical contacts. The proposed modeling strategy that is based on influence factors as well, first, identifies a corresponding radius for applying a counterbalancing heat load by calculating the heat flux that crosses the considered curved free-surface and countering it. Countering the crossing heat flux results in an adiabatic thermal boundary condition at the thermal free-surface, which is the primary concentration of this study. However, the developed technic could easily be extended to any thermal boundary. Therefore, this study formulates the mapping relation linking the heat load to its counterbalance part. A comparison of the thermoelastic displacements predicted by the model with FEA results indicate that, for a case with adiabatic boundary conditions at the free-surface, the errors intrinsic to half-space assumption decline up to 99% while reducing the computation times by more than 92%.

The next part of this study eliminates the effects of the remaining normal stress that is generated at the curved free-surface by half-space assumption, when applying a heat load on the contact surface. To do so, the process calculates a correction factor for the applied counterbalance heat load. Therefore, the complete free boundary correction procedure includes two steps: the first determines the dimensions and location of the counterbalance heat patch controlling the heat flux crossing the curved free boundary, and the second modifies the counterbalancing heat load to cancel out the thermoelastic normal stress influence. Implementing the final model and comparing the results obtained for different cases with the results obtained from FEA proves that current method improves the precision more than 95% while reducing the required time up to 98% percent.

The limitations of Article 3 and further recommendations include:

- As before, the curved edges validated in this study for thermal analysis are limited to closed circular edges. A future study could consider other geometrical curved edges and the mixed curved and straight edges.

- This work could benefit from further developing the correction factor for more generalized thermal boundary conditions at the free-surface.

Overall, after achieving the aforementioned contributions, this research presents a fast and reliable tool for analysis of a practical contact considering complete thermal aspects of a contact analysis. By using this tool, while gaining superior precision, the additional calculation time can be avoided. This approach will specifically advance lubricated contact modeling quality and swiftness because of its simplicity, speed, and agility. Thus, the excessive experimental trials and, consequently, their computational costs can be avoided for practical contacts.

This model is a practical tool specifically for analysis and development of the contacts with textured or grooved surfaces. As mentioned earlier in Section 1.12 , this kind of contacts has drawn a lot of attention like the studies performed in (Manser et al., 2019 ; Morris et al., 2018 ; Siripuram & Stephens, 2004 ; Tala-Ighil et al., 2007). Because of their benefits and importance, these textured surfaces are being used by well-known bearing manufacturers like SKF (SKF, 2012).

LIST OF BIBLIOGRAPHICAL REFERENCES

A09A0016. (2010). Aviation Investigation Report. *Transportation Safety board of Canada*.

Adams, G. G., & Nosonovsky, M. (2000). Contact modeling - forces. *Tribology International*, *33*(5), 431-442. https://doi.org/10.1016/S0301-679X(00)00063-3

Akbari, M., Sinton, D., & Bahrami, M. (2009). Moving heat sources in a half-space: effect of source geometry. *ASME 2009 Heat Transfer Summer Conference- Proceedings paper*, 685-694. https://doi.org/10.1115/ht2009-88562

Albers, A., Martin, P., & Lorentz, B. (2011). Modeling and design of contacts in electrical connectors. *ICED 11 - 18th International Conference on Engineering Design - Impacting Society Through Engineering Design*, *4*, 268-277.

Bachtar, F., Chen, X., & Hisada, T. (2006). Finite element contact analysis of the hip joint. *Medical and Biological Engineering and Computing*, *44*(8), 643-651. https://doi.org/10.1007/s11517-006-0074-9

Baddour, N. (2011). *Two-Dimensional Fourier transforms in polar coordinates*. *Advances in Imaging and Electron Physics* (Vol. 165). (S.l.) : Elsevier Inc. https://doi.org/10.1016/B978-0-12-385861-0.00001-4

Bahrami, M., Yovanovich, M. M., & Culham, J. R. (2005). Thermal contact resistance at low contact pressure: Effect of elastic deformation. *International Journal of Heat and Mass Transfer*, *48*(16), 3284-3293. https://doi.org/10.1016/j.ijheatmasstransfer.2005.02.033

Bair, S., & Khonsari, M. M. (2006). Reynolds equations for common generalized Newtonian models and an approximate Reynolds-Carreau equation. *Proceedings of the Institution of Mechanical Engineers, Part J: Journal of Engineering Tribology*, *220*(4), 365-374. https://doi.org/10.1243/13506501JET79

Balci, M. N., Yildirim, B., & Dag, S. (2015). Analysis of frictional contacts with heat generation considering temperature dependent properties. *International Journal of Mechanical Sciences*, *101-102*, 59-69. https://doi.org/10.1016/j.ijmecsci.2015.07.015

Bansal, D. (2009). *Tribological Investigation of Electrical Contacts*. Georgia Institute of Technology.

Barber, J. R. (1971). The solution of heated punch problems by point source methods. *International Journal of Engineering Science*, *9*(12), 1165-1170. https://doi.org/10.1016/0020-7225(71)90081-4

Barber, J. R. (1980). The Transient Thermoelastic Contact of A Sphere Sliding on A Plane. *Wear*, *59*(June 1979), 21-29.

Belforte, G., Conte, M., Bertetto, A. M., Mazza, L., & Visconte, C. (2009). Experimental and numerical evaluation of contact pressure in pneumatic seals. *Tribology International*, *42*(1), 169-175. https://doi.org/10.1016/j.triboint.2008.04.010

Bhaumik, S. K., Sujata, M., Kumar, M. S., Venkataswamy, M. A., & Parameswara, M. A. (2007). Failure of an intermediate gearbox of a helicopter. *Engineering Failure Analysis*, *14*(1), 85-100. https://doi.org/10.1016/j.engfailanal.2005.12.006

Bryant, M. D. (1988). Thermoelastic solutions for thermal distributions moving over half space surfaces and application to the moving heat source. *Journal of Applied Mechanics, Transactions ASME*, *55*(1), 87-92. https://doi.org/10.1115/1.3173665

Budinski, M. K. (2014). Failure analysis of a bearing in a helicopter turbine engine due to electrical discharge damage. *Case Studies in Engineering Failure Analysis*, *2*(2), 127-137. https://doi.org/10.1016/j.csefa.2014.05.003

Burton, R. A. (1980). Thermal Deformation in Frictionally Heated Contact. *Wear*, *59*(June 1979), 1-20.

Chatterjee, B., & Sahoo, P. (2014). Finite element based contact analysis of fractal surfaces - Effect of varying elastic modulus. *Procedia Engineering*, *90*, 116-122. https://doi.org/10.1016/j.proeng.2014.11.823

Chen, W. W., & Wang, Q. J. (2009). A Numerical Static Friction Model for Spherical Contacts of Rough Surfaces, Influence of Load, Material, and Roughness. *Journal of Tribology*, *131*(2), 021402. https://doi.org/10.1115/1.3063814

Chin-Tu, L., & Bryant, M. D. (1994). Thermoelastic evolution of contact area and mound temperatures in carbon graphite electrical brushes. *Wear*, *174*(1-2), 137-146. https://doi.org/10.1016/0043-1648(94)90095-7

Chu, L. M., Hsu, H. C., Lin, J. R., & Chang, Y. P. (2009). Inverse approach for calculating temperature in EHL of line contacts. *Tribology International*, *42*(8), 1154-1162. https://doi.org/10.1016/j.triboint.2009.03.017

CONTE, M., MANUELLO, A., L.MAZZA, & C.VISCONTE. (2006). Measurement of Contact Pressure in Pneumatic Actuator Seals. *International Conference on Tribology*, (September). Repéré à https://www.researchgate.net/publication/309726591

Crook, A. W. (1962). The Lubrication of Rollers III: A Theoretical Discussion of Friction and the Temperatures in the Oil Film. *Wear*, *5*, 246.

D.B. Hamilton, J. A. W. A. C. M. A. (1966). A Theory of Lubrication by Micro- irregularities. *Journal of Basic Engineering*, 177-185.

de Mul, J. M., Kalker, J. J., & Fredriksson, B. (1986). The Contact Between Arbitrarily Curved Bodies of Finite Dimensions. *Journal of Tribology*, *108*(1), 140-148. https://doi.org/10.1115/1.3261134

Dowson, D. (1997). *Elastohydrodynamics : fundamentals and applications in lubrication and traction*. *Tribology series*. (S.l.) : Elsevier Science B.V.

Dowson, D., & Higginson, G. R. (1959). A Numerical Solution to the Elasto-Hydrodynamic Problem. *Journal of Mechanical Engineering Science*, *1*(1), 6-15. https://doi.org/10.1243/jmes_jour_1959_001_004_02

Effertz, P. S., Fuchs, F., & Enzinger, N. (2017). Modelling the flash formation of linear friction welded 30CrNiMo8 high strength steel chains. *International Journal of Advanced Manufacturing Technology*, *92*(5-8), 2479-2486. https://doi.org/10.1007/s00170-017-0338-6

Erdemir, A. (2005). Review of engineered tribological interfaces for improved boundary lubrication. *Tribology International*, *38*(3), 249-256. https://doi.org/10.1016/j.triboint.2004.08.008

Etsion, I., Kligerman, Y., & Halperin, G. (1999). Analytical and experimental investigation of laser-textured mechanical seal faces. *Tribology Transactions*, *42*(3), 511-516. https://doi.org/10.1080/10402009908982248

Ghosh, M. K., & Hamrock, B. J. (1983). Thermal Elastohydrodynamic Lubrication of Line Contacts. *NASA Technical Memorandum 83424*.

Gohar, R., & A. Cameron. (1963). Optical Measurement of Oil Film Thickness under Elasto-hydrodynamic Lubrication. *Nature*, *200*, 458-459. Repéré à http://docs.lib.purdue.edu/icec/1226

Greenwood, J. A. (1972). An extension of the Grubin theory of elastohydrodynamic lubrication. *Journal of Physics D: Applied Physics*, *5*(12), 2195-2211. https://doi.org/10.1088/0022-3727/5/12/309

Greenwood, J. A., & Kauzlarich, J. J. (1973). Inlet shear heating in elastohydrodynamic lubrication. *Journal of Lubrication Technology*, *95*(4), 417-423. https://doi.org/10.1115/1.3451844

Gropper, D., Wang, L., & Harvey, T. J. (2016). Hydrodynamic lubrication of textured surfaces: A review of modeling techniques and key findings. *Tribology International*, *94*, 509-529. https://doi.org/10.1016/j.triboint.2015.10.009

GRUBIN, A. N., VINOGRADOVA, I. E., & KETOVA, K. F. (1949). *Investigation of the contact of machine components*. Moscow : Central Scientific Research Institute for Technology and Mechanical Engineering.

Guilbault, R. (2011). A Fast Correction for Elastic Quarter-Space Applied to 3D Modeling of Edge Contact Problems. *Journal of Tribology*, *133*(3), 031402. https://doi.org/10.1115/1.4003766

Guilbault, R. (2013). A simplified thermal analysis of elastohydrodynamic contacts. *Journal of Tribology*, *135*(2), 1-13. https://doi.org/10.1115/1.4023085

Guilbault, R., Gosselin, C., & Cloutier, L. (2005). Express Model for Load Sharing and Stress Analysis in Helical Gears. *Journal of Mechanical Design*, *127*(6), 1161. https://doi.org/10.1115/1.1992509

Habchi, W., & Vergne, P. (2015). On the compressive heating/cooling mechanism in thermal elastohydrodynamic lubricated contacts. *Tribology International*, *88*, 143-152. https://doi.org/10.1016/j.triboint.2015.03.025

Habchi, W., Vergne, P., Bair, S., Andersson, O., Eyheramendy, D., & Morales-Espejel, G. E. (2010). Influence of pressure and temperature dependence of thermal properties of a lubricant on the behaviour of circular TEHD contacts. *Tribology International*, *43*, 1842-1850. https://doi.org/10.1016/j.triboint2009.10.002

Habchi, Wassim. (2008). *A Full-System Finite Element Approach to Elastohydrodynamic Lubrication Problems : Application to Ultra-Low-Viscosity Fluids*. L'Institut National des Sciences Appliquées de Lyon.

Hamrock, B. J., & Dowson, D. (1976). Isothermal Elastohydrodynamic Lubrication of Point Contacts - 1. Theoretical Formulation. *NASA Technical Note*, *98 Ser F*, 31. https://doi.org/10.1115/1.3452801

Hanson, M. T., & Keer, L. M. (1995). Mechanics of edge effects on frictionless contacts. *International Journal of Solids and Structures*, *32*(3-4), 391-405. https://doi.org/10.1016/0020-7683(94)00153-N

Hartnett, M. J. (1980). A general numerical solution for elastic body contact problems. *Solid contact and lubrication*, *30*, 51-66.

Herák, D., Chotěborský, R., Sedláček, A., & Janča, E. (2018). Exploitation of Hertz’s contact pressures in friction drives. *Research in Agricultural Engineering*, *52*(No. 3), 107-113. https://doi.org/10.17221/4886-rae

Hertz, H. (1896). *Miscellaneous Papers*. *MACMILLAN & CO.* (S.l.) : (s.n.).

Hetényi, M. (1960). A Method of Solution For The Elastic Quarter-Plane. *Journal of Applied Mechanics*, 289-296.

Hetényi, M. (1970). A General Solution for the Elastic Quarter Space. *Journal of Applied Mechanics*, *37*(1), 70-76. https://doi.org/10.1115/1.3408492

Houpert, L. (1985). New results of traction force calculations in elastohydrodynamic contacts. *Journal of Tribology*, *107*(April).

Hsiao, H.-S. S., Hamrock, B. J., & Tripp, J. H. (1999). Finite Element System Approach to EHL of Elliptical Contacts: Part I—Isothermal Circular Non-Newtonian Formulation. *Journal of Tribology*, *120*(October 1998), 695-704. Repéré à http://tribology.asmedigitalcollection.asme.org/ on 11/24/2016

Incropera, F. P., & De Witt, D. P. (1981). Fundamentals of heat transfer. https://doi.org/10.13182/nse65-a18809

J. R., Barber, C. J. M.-M. (1982). Green's functions for transient thermoelastic contact problems for the half-space. *Wear*, *79*, 11-19.

Jang, Y. H., Cho, H., & Barber, J. R. (2009). The Thermoelastic Hertzian Contact Problem. *International Journal of Solids and Structures*, *46*(22-23), 4073-4078. https://doi.org/10.1016/j.ijsolstr.2009.08.004

Jedrasiak, P., Shercliff, H. R., McAndrew, A. R., & Colegrove, P. A. (2018). Thermal modelling of linear friction welding. *Materials and Design*, *156*, 362-369. https://doi.org/10.1016/j.matdes.2018.06.043

Jl, J., Renee, B., & Jacoby, B. R. (1991). *Fundamental Mechanisms Affecting Friction Welding Under Vacuum*. Massachusetts Institute of Technology.

Johnson, K. L. (1987). *Contact Mechanics*. Cambridge : University Press. https://doi.org/10.1201/b17110-2

Johnson K.L. (1985). *Contact Mechanics*. (S.l.) : Cambridge University Press.

Keer, L. M., Lee, J. C., & Mura, T. (1983). Hetényi's elastic quarter space problem revisited. *International Journal of Solids and Structures*, *19*(6), 497-508. https://doi.org/10.1016/0020-7683(83)90087-2

Khan, H., Sinha, P., & Saxena, A. (2009). A simple algorithm for Thermo-Elasto-Hydrodynamic Lubrication problems. *International Journal of Research and Reviews in Applied Sciences*, *1*(3), 265-279.

Kingsbury Inc. (2019). *A general guide to the principles, operation and troubleshooting of hydrodynamic bearings*. (S.l.) : (s.n.).

Kuroki, Hiroshi; Nezaki, Koji; Wakabayashi, Tsukasa; Nakamura, K. (2014). Application of Linear Friction Welding Technique to Aircraft Engine Parts. *IHI Engineering review*, *47*(1), 40-43.

Li, J., & Berger, E. J. (2003). A semi-analytical approach to three-dimensional normal contact problems with friction. *Computational Mechanics*, *30*(4), 310-322. https://doi.org/10.1007/s00466-002-0407-y

Li, Junshan, & Berger, E. J. (2001). A Boussinesq-Cerruti solution set for constant and linear distribution of normal and tangential load over a triangular area. *Journal of Elasticity*, *63*(2), 137-151. https://doi.org/10.1023/A:1014013425423

Li, W., Vairis, A., Preuss, M., & Ma, T. (2016). Linear and rotary friction welding review. *International Materials Reviews*, *61*(2), 71-100. https://doi.org/10.1080/09506608.2015.1109214

Lindemann, Z., Skalski, K., Wlosinski, W., & Zimmerman, J. (2006). Thermo-mechanical phenomena in the process of friction welding of corundum ceramics and aluminium. *Bulletin of the Polish Academu of Sciences*, *54*(1), 1-8.

Liu, G., & Wang, Q. (2000). Thermoelastic asperity contacts, frictional shear, and parameter correlations. *Journal of Tribology*, *122*(1), 300-307. https://doi.org/10.1115/1.555357

Liu, M., Zhang, J., Xu, P., Cai, H., Ku, H., & Wu, C. (2019). Thermal elastohydrodynamic lubrication analysis of helical gear pair under starved lubrication condition. *Lubrication Science*, *31*(7), 321-334. https://doi.org/10.1002/ls.1474

Liu, S., & Hua, D. Y. (2009). Three-Dimensional Semiperiodic Line Contact–Periodic in Contact Length Direction. *Journal of Tribology*, *131*(2), 021408. https://doi.org/10.1115/1.3084237

Liu, Z., Pickens, D., He, T., Zhang, X., Liu, Y., Nishino, T., & Jane Wang, Q. (2019). A Thermal Elastohydrodynamic Lubrication Model for Crowned Rollers and Its Application on Apex Seal-Housing Interfaces. *Journal of Tribology*, *141*(4), 14. https://doi.org/10.1115/1.4042503

Lubarda, V. A. (2013). Circular loads on the surface of a half-space: Displacement and stress discontinuities under the load. *International Journal of Solids and Structures*, *50*(1), 1-14. https://doi.org/10.1016/j.ijsolstr.2012.08.029

M. G. Cooper, B. B. Mikic, M. M. Y. (1969). Thermal Contact Conductance. *International Journal of Heat and Mass Transfer*, *12*, 279-300.

Manser, B., Belaidi, I., Hamrani, A., Khelladi, S., & Bakir, F. (2019). Performance of hydrodynamic journal bearing under the combined influence of textured surface and journal misalignment: A numerical survey. *Comptes Rendus - Mecanique*, *347*(2), 141-165. https://doi.org/10.1016/j.crme.2018.11.002

Mark Kachanov, Boris Shafiro, I. T. (2003). *Handbook of Elasticity Solutions*. *Springer Science+Business Media Dordrecht* (First). (S.l.) : Kluwer Academic Publishers. https://doi.org/10.1007/978-94-017-0169-3

Marx, N., Fernández, L., Barceló, F., & Spikes, H. (2018). Shear Thinning and Hydrodynamic Friction of Viscosity Modifier-Containing Oils. Part I: Shear Thinning Behaviour. *Tribology Letters*, *66*(3), 1-14. https://doi.org/10.1007/s11249-018-1039-5

Meng, X., Yu, C., Xie, Y., & Mei, B. (2018). Thermal insulation effect on EHL of coated cam/tappet contact during start up. *Industrial Lubrication and Tribology*, *70*(6), 917-926. https://doi.org/10.1108/ILT-03-2016-0065

Mihailidis, A., Agouridas, K., & Panagiotidis, K. (2013). Non-Newtonian Starved Thermal-Elastohydrodynamic Lubrication of Finite Line Contacts. *Tribology Transactions*, *56*(1), 88-100. https://doi.org/10.1080/10402004.2012.729298

Mikic, B. B. (1974). Thermal Contact Conductance; Theoritical Considerations. *International Journal of Heat and Mass Transfer*, *17*, 205-214.

Mikula, A. M. (1985). The Leading-Edge-Groove Tilting - Pad Thrust Bearing : Recent Developments. *Journal of Tribology*, *107*(July), 423-430. https://doi.org/https://doi.org/10.1115/1.3261099

Mikula, A. M. (1988). Further Test Results of the Leading-Edge-Groove (LEG) Tilting Pad Thrust Bearing. *Journal of Tribology*, *110*(1), 174-180. https://doi.org/https://doi.org/10.1115/1.3261559

Moes, H. (1992). Optimum similarity analysis with applications to elastohydrodynamic lubrication. *Wear*, *159*, 57-66.

Morales-Espejel, G. E., & Wemekamp, A. W. (2008). Ertel-Grubin method in elastohydrodynamic lubrication - A review. *Proceedings of the Institution of Mechanical Engineers, Part J: Journal of Engineering Tribology*, *222*(1), 15-34. https://doi.org/10.1243/13506501JET325

Morris, N. J., Shahmohamadi, H., Rahmani, R., Rahnejat, H., & Garner, C. P. (2018). Combined experimental and multiphase computational fluid dynamics analysis of surface textured journal bearings in mixed regime of lubrication. *Lubrication Science*, *30*(4), 161-173. https://doi.org/10.1002/ls.1414

Najjari, M., & Guilbault, R. (2014). Edge contact effect on thermal elastohydrodynamic lubrication of finite contact lines. *Tribology International*, *71*, 50-61. https://doi.org/10.1016/j.triboint.2013.11.005

Necas, D., Sperka, P., Vrbka, M., Krupka, I., & Hartl, M. (2015). Film thickness mapping in lubricated contacts using fluorescence. *MM Science Journal*, *2015*(DECEMBER), 821-824. https://doi.org/10.17973/MMSJ.2015_12_201524

Ohue, Y., & Tanaka, H. (2013). Effect of Surface Texturing on Lubricating Condition under Point Contact Using Numerical Analysis. *Engineering*, *05*(04), 379-385. https://doi.org/10.4236/eng.2013.54050

Otero, J. E., Ochoa, E. de la G., Tanarro, E. C., Lantada, A. D., & Munoz-Guijosa, J. M. (2012). Analytical model for predicting friction in line contacts. *Lubrication Science*, *28*, 189-205. https://doi.org/10.1002/ls.

Peiran, Y., & Shizhu, W. (1990). A generalized reynolds equation for non-newtonian thermal elastohydrodynamic lubrication. *Journal of Tribology*, *112*(4), 631-636. https://doi.org/10.1115/1.2920308

Poon, C. Y., & Sayles, R. S. (1994). Numerical Contact Model of A Smooth Ball on an Anisotropic Rough Surface. *Journal of Tribology*, *116*(4), 194-201. https://doi.org/10.1115/1.2927345

Reddy, A. R. A. C. (2015). Finite Element Analysis of Friction Welding Process for UNS C23000 Brass and AISI 1021 Steel. *International Journal of Science and Research (IJSR)*, *4*(5), 1691-1696. Repéré à https://www.ijsr.net/archive/v4i5/SUB154501.pdf

Sahoo, P., & Ghosh, N. (2007). Finite element contact analysis of fractal surfaces. *Journal of Applied Physics*, *40*(14), 4245-4252. https://doi.org/10.1088/0022-3727/40/14/021

Siddiqui, N. A., Deen, K. M., Khan, M. Z., & Ahmad, R. (2013). Investigating the failure of bevel gears in an aircraft engine. *Case Studies in Engineering Failure Analysis*, *1*(1), 24-31. https://doi.org/10.1016/j.csefa.2012.12.001

Siripuram, R. B., & Stephens, L. S. (2004). Effect of deterministic asperity geometry on hydrodynamic lubrication. *Journal of Tribology*, *126*(3), 527-534. https://doi.org/10.1115/1.1715104

SKF. (s.d.). SKF Hydrostatic shoe bearing arrangement.

SKF. (2012). *SKF composite plain bearings*. (S.l.) : (s.n.). Repéré à http://www.skf.com/binary/68-107917/SKF-composite-plain-bearings---11004-EN.pdf

Spiga, M., & Carpinteri, A. (1984). Three dimensional thermoelastic analysis of a semi infinite solid with arbitrary heat supply. *Ingenieur-Archiv*, *54*, 253-258. https://doi.org/10.1007/BF00532550

Stachowiak, G. W., & Batchelor, A. W. (2014). *ENGINEERING TRIBOLOGY* (Forth edit, Vol. 4). (S.l.) : Butterworth-Heinemann, Elsevier.

Sternberg, E., & Mcdowell, E. L. (1957). On the Steady-State Thermoelastic problem for the half-space. *Quarterly of Applied Mathematics*, *14*(4), 381-398. Repéré à https://www.jstor.org/stable/43636015?seq=1

Stupkiewicz, S. (2009). Finite element treatment of soft elastohydrodynamic lubrication problems in the finite deformation regime. *Computational Mechanics*, *44*(5), 605-619. https://doi.org/10.1007/s00466-009-0394-3

Sukumaran, J., Baets, P. De, & Fauconnier, D. (2018). Frictional Heating in Dry and Lubricated Contacts. *Friction, Lubrication, and Wear Technology*, *18*, 67-80. https://doi.org/10.31399/asm.hb.v18.a0006409

Svoboda, P., Kostal, D., Kunak, J., & Krupka, I. (2014). Study of Grease Behaviour in a Starved Lubricated Contact. *MM Science Journal*, 464-469.

Tala-Ighil, N., Maspeyrot, P., Fillon, M., & Bounif, A. (2007). Effects of surface texture on journal-bearing characteristics under steady-state operating conditions. *Proceedings of the Institution of Mechanical Engineers, Part J: Journal of Engineering Tribology*, *221*(6), 623-633. https://doi.org/10.1243/13506501JET287

Tazi, N., Châtelet, E., & Bouzidi, Y. (2017). Wear analysis of wind turbine bearings. *International Journal of Renewable Energy Research*, *7*(4), 2120-2129.

Tian, X., & Bhushan, B. (1996). A Numerical Three-Dimensional Model for the Contact of Rough Surfaces by Variational Principle. *Journal of Tribology*, *118*(1), 33. https://doi.org/10.1115/1.2837089

Timoshenko S. P., G. J. N. (s.d.). *Theory of Elasticity* (Third Edit). (S.l.) : Mcgraw-Hill.

van Leeuwen, H. J., Meijer, H., & Schouten, M. (1987). Elastohydrodynamic film thickness and temperature measurements in dynamically loaded concentrated contacts: eccentric cam-flat follower. *Tribology Series*, 611-625.

Varela, A. C., García, A. B., & Santos, I. F. (2017). Tribology International Modelling of LEG tilting pad journal bearings with active lubrication. *Tribiology International*, *107*(November 2016), 250-263. https://doi.org/10.1016/j.triboint.2016.11.033

Venner, C. H., & Bos, J. (1994). Effects of lubricant compressibility on the film thickness in EHL line and circular contacts. *Wear*, *173*(1-2), 151-165. https://doi.org/10.1016/0043-1648(94)90268-2

Venner, C. H., & Napel, W. E. te. (1992a). Multilevel solution of the elastohydrodynamically lubricated circular contact problem part 1: Theory and numerical algorithm. *Wear*, *152*(2), 351-367. https://doi.org/10.1016/0043-1648(92)90133-S

Venner, C. H., & Napel, W. E. te. (1992b). Multilevel solution of the elastohydrodynamically lubricated circular contact problem part 2: Smooth surface results. *Wear*, *152*(2), 369-381. https://doi.org/10.1016/0043-1648(92)90133-S

Veress, Á., Molnár, J., & Rohács, J. (2009). Compressible viscous flow solver. *Periodica Polytechnica Transportation Engineering*, *37*(1-2), 77-81. https://doi.org/10.3311/pp.tr.2009-1-2.13

Wakuda, M., Yamauchi, Y., Kanzaki, S., & Yasuda, Y. (2003). Effect of surface texturing on friction reduction between ceramic and steel materials under lubricated sliding contact. *Wear*, *254*(3-4), 356-363. https://doi.org/10.1016/S0043-1648(03)00004-8

Wan, G. T. Y., & Wong, P. L. (2009). Pressure Dependence of the Limiting Shear Stress Coefficient of Liquid Lubricants. *Advanced Tribology*, (1), 206-210. https://doi.org/10.1007/978-3-642-03653-8_68

Wang, K. L., & Cheng, H. S. (1980). Thermal elastohydrodynamic lubrication of spur gears. *National Aeronautics and Space Administration, CR 3241*, (February 1980).

Wang, W. Z., Hu, Y. Z., Wang, H., & Liu, Y. C. (2006). Effect of thermo-elastic deformation on lubricated point contacts. *Proceedings of the Institution of Mechanical Engineers, Part J: Journal of Engineering Tribology*, *220*(6), 523-534. https://doi.org/10.1243/13506501JET76

Wang, X., Liu, Y., & Zhu, D. (2017). Numerical Solution of Mixed Thermal Elastohydrodynamic Lubrication in Point Contacts with Three-Dimensional Surface Roughness. *Journal of Tribology*, *139*(1). https://doi.org/10.1115/1.4032963

Williamson, M., & Majumdar, A. (1992). Effect of Surface Deformations on Contact Conductance. *Journal of Heat Transfer*, *114*(4), 802-810. https://doi.org/10.1115/1.2911886

Willner, K. (2008). Fully Coupled Frictional Contact Using Elastic Halfspace Theory. *Journal of Tribology*, *130*(3), 031405. https://doi.org/10.1115/1.2913537

Wymer, D. G., & Cameron, A. (1974). Elastohydrodynamic lubrication of a line contact. *Proceedings of the Institution of Mechanical Engineers*, *188*(1), 221-238. https://doi.org/10.1243/PIME_PROC_1974_188_024_02

Xu, G., & F. Sadeghi. (1998). A Thermal Elastohydrodynamic Lubricated Thrust Bearing Contact Model. *International Compressor Engineering Conference*, *Paper 1226*, 117-122. Repéré à http://docs.lib.purdue.edu/icec/1226

Yalpanian, A., & Guilbault, R. (2020). A fast correction for half-space theory applied to contact modeling of bodies with curved free surfaces. *Tribology International*, *147*(March), 13. https://doi.org/10.1016/j.triboint.2020.106292

Yalpanian, A., & Guilbault, R. (2021). A fast thermoelastic model based on the half-space theory applied to elastohydrodynamic lubrication of line contacts involving free boundaries. *Tribology International*.

Yang, J., & Komvopoulos, K. (2005). Impact of a Rigid Sphere on an Elastic Homogeneous Half-Space. *Journal of Tribology*, *127*(2), 325. https://doi.org/10.1115/1.1828078

Yasuda, K., Armstrong, R. C., & Cohen, R. E. (1981). Shear flow properties of concentrated solutions of linear and star branched polystyrenes. *Rheologica Acta*, *20*(2), 163-178. https://doi.org/10.1007/BF01513059

Zhang, M., Suo, S., Jiang, Y., & Meng, G. (2018). Experimental measurement method for contact stress of elastic metal sealing ring based on pressure sensitive paper. *Metals*, *8*(11). https://doi.org/10.3390/met8110942

Zhang, Y., & Wen, S. (2002). EHL film thickness limitation theory under a limiting shear stress. *Tribology Transactions*, *45*(4), 531-539. https://doi.org/10.1080/10402000208982584

Zulkifli, N. W. M., Kalam, M. A., Masjuki, H. H., Shahabuddin, M., & Yunus, R. (2013). Wear prevention characteristics of a palm oil-based TMP (trimethylolpropane) ester as an engine lubricant. *Energy*, *54*, 167-173. https://doi.org/10.1016/j.energy.2013.01.038